Development of a Hybrid Pixel Detector Based Transverse Profile Monitor for the CERN Proton Synchrotron

Swann Levasseur

Department of Physics
Royal Holloway, University of London

A thesis submitted to the University of London for the degree of Doctor of Philosophy

November 2019

Declaration

I confirm that the work presented in this thesis is my own. Where information has been derived from other sources, I confirm that this has been indicated in the document.

Signed: 

Date: 12/02/2020

To our poor planet to which we are not kind enough with.

Abstract

The ability to rapidly identify the source of emittance blow-up in the CERN Proton Synchrotron (PS) is crucial to ensure the good operation of the Large Hadron Collider (LHC) and its successor the High Luminosity LHC (HL-LHC). Such ability requires to continuously and non-destructively measure the beam size. However, the beam transverse diagnostics in the PS are currently performed by Beam Wire-Scanners (BWS) and Secondary Emission Monitor (SEM) grids. Both of these systems provide high-quality measurements of the beam transverse size. Nonetheless, the destructive nature of their measurement method limits their use to single-shot measurements during the beam commissioning. For this reason, the installation of a new Beam Gas Ionisation (BGI) profile monitor was proposed for the PS.

The new PS-BGI infers the beam profile from the transverse distribution of electrons created by the ionisation of rest gas molecules by the high energy beam particles. The distribution is measured by accelerating the electrons onto an imaging detector based on Timepix3 Hybrid Pixel Detector (HPD). This measurement method allows for continuous, non-destructive beam size measurement. Moreover, the extreme sensitivity of Timepix3 HPDs allows foregoing the use of a gas injection system, while permitting to record the beam size at several kilo-Hertz. This thesis covers the development of this new PS-BGI, from early concept and simulation to the installation and commissioning of a prototype in the PS. This prototype demonstrated the first successful use of Hybrid Pixel Detectors (HPD) in the primary vacuum of an accelerator at CERN. The performances of the prototype were characterised and the first continuous beam profile measurements of the LHC-type beam in the PS were recorded.

Acknowledgements

I would like to thank my Mom (no need for her name, she knows it) for feeding me, giving me shelter all these years and always having my back. I have always done what I wanted and it is mostly thanks to you. I am not sure she will understand this, thus here is the abbreviated french version *Merci Maman*!

Dad you gave me your passion for the mountains and nature, this has been my sole driving force for all these years. You are currently fighting for you life and I have only one thing to say, *Force et Honneur*!

To my sisters, this PhD thesis has only been an elaborate way to force you into long academic studies. Now you have to do better than me. (PS: I love you both).

Thanks to Julia, my beautiful, strong and amazing girlfriend. Did I say amazing ? Thanks for supporting me all this time, I love you.

Bernd, you somehow convinced me into this thesis, thank you. Marius, for getting me into this mess of a project. James, for being the best supervisor and boss I could have ever wanted. Stephen, even though you are the busiest man on earth, you have always answered my calls for help. Hampus, without you the BGI would not work. Christos, you are always smiling. Also, nice sneakers! Kenichiro, for your *I love beer* t-shirt. And all of the people at CERN that have made this project a reality, Joshua, Gerhard, Didier, Dominique, Oliver, Ian, Florentina, Sylvain and all the others I forgot.

Some honourable mention: CERN cleaning personnel; Unica; my office plant (you showed me that one can survive even the worst treatments).

Contents

List of Figures

List of Tables

Chapter 1

Introduction

There are an estimated 30000 active particle accelerators in the world. About half of these are dedicated to industrial processes, such as ion implantation or electron beam processing [1]. The largest part of the other half is used in the medical sector to produce rare radio-isotopes. A niche but paradoxically famous use of accelerators is High Energy Physics (HEP). As the name suggests, HEP accelerators are machines designed to accelerate particles to high energies. These are then collided creating extreme physical conditions. The by-products of these collisions are exotic particles whose properties are studied in large experiments.
Historically, flagship HEP accelerators were almost always designed to reach higher particle/collision energy. This extra energy permitted the creation of, yet to be discovered, massive particles.

This ever increasing collision energy requirement led CERN to develop and construct, the Large Hadron Collider (LHC) [2] where protons are collided head-on at energies up to 13 TeV (6.5 TeV/particle). The LHC has been in operation since 2008, culminating in 2012 with the discovery of the Brought Englert Higgs boson [3, 4]. This operation was enabled by CERN accelerator complex, where the Linac2, Booster, Proton Synchrothron (PS) [5] and Super PS (SPS) [6] were used as proton injectors for LHC. The CERN accelerator complex is presented in Figure 1.1.

The probability for a specific particle or effect to be produced - often referred to as events of interest - during a collision is called the production cross-section σ. Typical cross-sections to produce interesting events are extremely small and a very large number of collisions are required to observe them. The number of interesting events produced

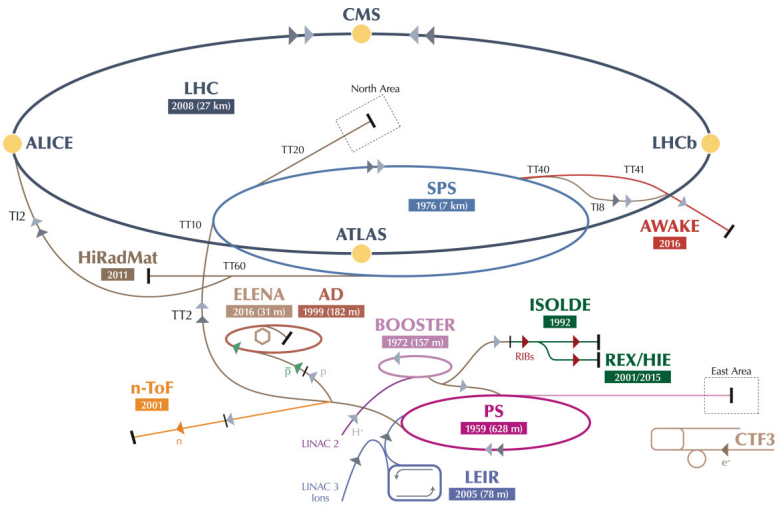

Figure 1.1: The CERN accelerator complex. The LHC injectors chain comprises Linac 2, Linac 3, LEIR, Booster, PS, SPS and the multiple transfer lines connecting them together.

per second $\frac{dN}{dt}$ is proportional to the cross section for the event of interest σ_p and the proportionality constant is called the luminosity L [7]:

$$\frac{dN}{dt} = L\sigma_p \tag{1.1}$$

Luminosity is an important parameter as it governs the rate at which certain phenomena are observed. This is particularly valid for HEP experiments which rely on statistical evidence for their measurements.

1.1 Thesis project context

In order to extend the discovery potential of the LHC, CERN is undergoing a major program to increase the luminosity of the LHC [8, 9]. The aim of the High Luminosity (HL)-LHC project is to increase the nominal instantaneous luminosity by a factor five (to reach $5 \times 10^{34}\,\mathrm{cm}^{-2}\mathrm{s}^{-1}$, leading to an expected increase of the integrated luminosity by a factor ten (from $300\,\mathrm{fb}^1$ to $3000\,\mathrm{fb}^1$) over a ten year period.

The instantaneous luminosity of an accelerator colliding Gaussian beams head-on can be expressed by [7]:

$$L = \frac{f_{rev} n_b N_1 N_2}{4\pi\sigma_x^*\sigma_y^*} S, \tag{1.2}$$

where f_{rev} is the beam revolution frequency, n_b the number of bunches per beam, N_1/N_2 the number of protons per bunch (ppb) for beam one, and two and σ_x^* / σ_y^* the bunch

transverse size in the horizontal and vertical plane at the Interaction Point (IP). S is a geometrical reduction factor given by:

$$S = \frac{1}{\sqrt{1 + \left(\frac{\sigma_z}{\sigma_x^*} \tan\frac{\theta_c}{2},\right)^2}} \tag{1.3}$$

where θ_c is the bunch crossing angle and σ_z the bunch longitudinal size.

The current strategy to achieve a five fold increase in luminosity consists in doubling the bunch population (N_1, N_2) and reducing beam size at the IPs. This reduction implies a stronger beam focusing at the HEP and it will be achieved by using new Nb_3Sn superconducting focusing magnets. The cost for a stronger focus is an increase in the bunch crossing angle, lowering the luminosity. To mitigate this effect, the bunches will be rotated prior to the focusing stage using so called *crab cavities* [10,11].

While the beam size and crossing angle at the IPs are parameters affecting the LHC only, the bunch population increase has a large effect on the injectors chain. The injectors were not designed to work with such an intense beam, moreover this intensity makes it difficult to maintain the beam size within the requirements.

To address these challenges, the LHC Injector Upgrade (LIU) project [12] is implementing an extensive hardware upgrade of the injectors. The most noticeable change is the replacement of Linac2 by the new H^- Linac4 [13]. To ensure the lowest blow-up of the beam size, LIU calls for a large upgrade of the beam instrumentation. As part of this instrumentation upgrade, the ability to continuously monitor the beam emittance in the PS was requested [14]. A new Beam Gas Ionisation (BGI) profile monitor was therefore commissioned. This new instrument is required to measure the beam profile at a rate ≥ 1 kHz with a relative error ≤ 1 %. To meet these requirements, a new detection system based on hybrid pixel detectors would have to be developed.

Although the new Proton Synchrotron BGI (PS-BGI) is required to monitor the beam emittance, it rather measure the transverse beam size. In order to understand the relation between the beam emittance and transverse size, the next section introduces the basic of charged particles transverse dynamics in synchrotrons.

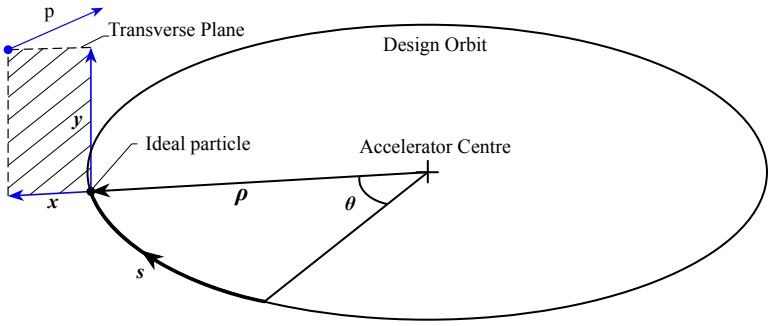

Figure 1.2: Circular coordinate system with the ideal (black) and arbitrary (blue) particle trajectories. ρ is the radius and θ the phase relative to the machine centre. (s, y) and (s, x) are the longitudinal planes, while (x, y) is the transverse plane.

1.2 Charged particle motion in a circular particle accelerator

The general motion of a single particle with charge q in a circular accelerator can be expressed by the following expression:

$$\frac{dp}{dt} = q\left(\vec{E} + \vec{v} \times \vec{B}\right) \tag{1.4}$$

This particle is likely to have a high velocity $\vec{v}$, the relativistic momentum $p = \gamma_r m_0 v$ is therefore used here, with m_0 the particle rest mass and v its velocity as a scalar. $\gamma_r = 1/\sqrt{1-{\beta_r}^2}$ and $\beta_r = v/c$ are the relativistic gamma and beta. The subscript r is used for clarity as the letter γ and β are later introduced in this chapter. Equation 1.4 shows that the effect of magnetic fields on a charged particle momentum is largely affected by its velocity. In order for an electrostatic deflector to equal a simple 1 T dipole magnet on a proton with $\beta_r = 0.5$, it would require an electric field in the $10^7\,\mathrm{V\,m^{-1}}$. For this reason modern accelerators prefer the use of magnets to guide and focus high energy particle beams.

In circular accelerators, the homogeneous magnetic field of dipole magnets is used in conjunction with the particle velocity to bend its trajectory to the desired radius of curvature. In this case, the particle is only subject to a magnetic field perpendicular to its motion, resulting in a curved trajectory.

$$\frac{dp}{dt} = q\vec{v} \times \vec{B}_{dipole}. \tag{1.5}$$

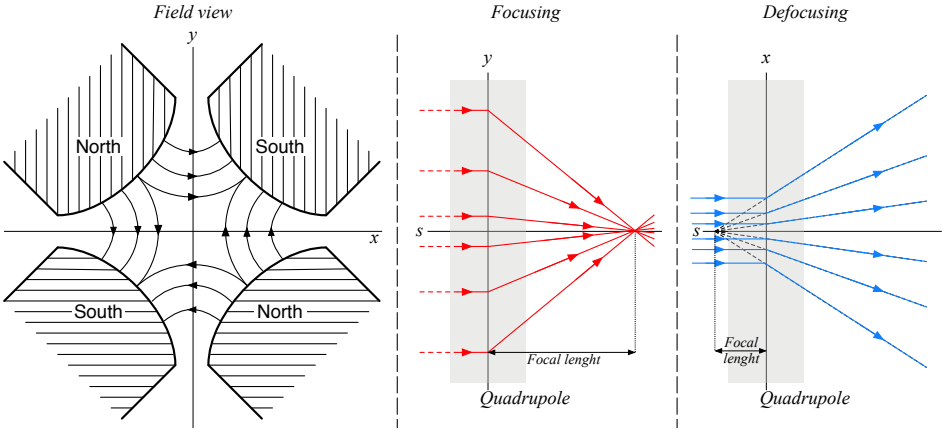

Figure 1.3: A quadrupole magnet comprises four poles (two north and south) angularly equidistant with a $\frac{\pi}{4}$ offset. The field-lines are represented in the transverse view (left) while the focusing and defocusing effects are shown in the longitudinal view (right). This particular magnet focus negatively charged particles in the vertical (y) axis and defocus them in the horizontal axis (x)

The condition to reach a circular motion for a particle is obtained by equating the centrifugal force (1.6) with the previous expression (1.5), resulting in equation 1.7.

$$F_{centri} = \frac{\gamma m_0 v^2}{\rho} \tag{1.6}$$

$$B\rho = \frac{p}{q} \tag{1.7}$$

The quantity $B\rho$ is the so called *magnetic rigidity*, with ρ the bending radius. It shows how the machine radius and maximum magnetic field strength defines the maximum particle momentum that can be confined in a circular accelerator. A circular coordinate system is presented in Figure 1.2. It presents the orbit (s) of an ideal charged particle with momentum p_0 guided by dipole magnets. However, a more likely scenario is represented by the blue particle. This particle has a trajectory divergent from the ideal one and needs to be steered back toward the design orbit for it to complete a full revolution.
Quadrupole magnets, presented in Figure 1.3, are commonly used for this task. Their magnetic field strength k

$$k = \frac{1}{B\rho}\frac{dB_y}{dx} \tag{1.8}$$

follows a linear gradient dB_y/dx relative to the magnet centre. This property allows a quadrupole to provide an angular deflection to a particle, essentially making it behave like a lens. A positive k represents a focusing effect in the vertical plane (y) and defocusing in the horizontal plane (x), while a negative k does the opposite. The focal length of this

lens is expressed as

$$f = -\frac{1}{kl} \tag{1.9}$$

with l the magnet thickness. In order to compensate for the fact that quadrupoles only focus in one plane, they are usually combined in pairs called *FODO* cells. This arrangement of focusing and defocusing element is then spread, in combination with dipole magnets, throughout the accelerator circumference. Such an accelerator is called an alternating gradient machine.

The transverse motion of a charged particle in a constant gradient machine is expressed by a set of differential equations called Hill's equations

$$y'' + k(s)y = 0 \tag{1.10}$$

$$x'' + \left[\frac{1}{\rho(s)^2} - k(s)\right] x = 0 \tag{1.11}$$

where $k(s)$ is a periodic function of the quadrupoles strength and x , y are the particle displacement. The vertical motion (1.10) is only affected by the quadrupoles, while the horizontal motion (1.11) sees both the effects of the dipole $1/\rho(s)^2$ (called weak focusing) and quadrupoles. Moreover the assumption that the motion in both planes is decoupled is made.

Hill's equation solution for x and x' (the particle divergence angle)

$$x = \sqrt{\beta(s)\epsilon}\cos\left(\omega(s) + \omega_0\right) \tag{1.12}$$

$$x' = \sqrt{\frac{\epsilon}{\beta(s)}}\left[\frac{\beta'(s)}{2}\cos\left(\omega(s) + \omega_0\right) - \sin\left(\omega(s) + \omega_0\right)\right] \tag{1.13}$$

is similar to a harmonic oscillator where $k(s)$ is a restoring constant. The quantities ϵ and ω_0 are constants found from the initial conditions. $\beta(s)$, also called the betatron function, is a periodic function representing the amplitude modulation caused by $k(s)$. In order for the aforementioned solution to be valid, $\omega(s)$ the phase advance, and $\beta(s)$ must have the same period.

The take away from Hill's equation is that a particle moving in a circular accelerator will experience oscillations in the transverse planes. The number of transverse oscillations

per revolution is called the *Tune* (represented by the letter Q). It can be expressed by

$$Q = \frac{1}{2\pi} \oint \frac{ds}{\beta(s)} \tag{1.14}$$

An integer, or simple fraction, Tune is to be avoided as the particle will repeat its trajectory for every revolution, easily entering a resonant growth due to small imperfections in the magnet's lattice.

The solution to Hill's equation presented earlier is only valid for periodic lattices. It is however possible to solve particle transverse motion for any lattice configuration by adopting the matrix formalism. This method allows us to treat each finite element of the lattice (called a cell), including magnets and drift spaces, as a transport matrix.

$$\begin{pmatrix} x \\ x' \end{pmatrix}_{s_2} = M_{21} \begin{pmatrix} x \\ x' \end{pmatrix}_{s_1} \tag{1.15}$$

M_{21} is a two-by-two matrix representing the change in position and divergence angle from a point s_1 to s_2. The general form of this matrix is obtained from 1.12 and 1.13 for s_1 and s_2. It is presented here :

$$M_{21} = \begin{pmatrix} \cos\mu + \alpha \sin\mu & \beta \sin\mu \\ -\gamma \sin\mu & \cos\mu - \alpha \sin\mu \end{pmatrix} \tag{1.16}$$

The quantities $\alpha = -\beta'(s)/2$, $\beta = \beta(s)$ and $\gamma = (1 + \alpha^2)/\beta(s)$ are called the *Twiss parameters*. While $\mu = \omega(s_2) - \omega(s_1)$ is the phase advance for the cell. The solution for a complete lattice can be found by combining all cell transport matrices by multiplication.

It is possible to represent the result from 1.12 and 1.13 as an ellipse in phase space (x, x'). This ellipse is drawn for a fixed position in s, where each each point represents a revolution of the particle. The ellipse equation, named the Courant and Snyder invariant, is:

$$\gamma(s)x(s)^2 + 2\alpha(s)x(s)x'(s) + \beta(s)x'(s)^2 = \epsilon \tag{1.17}$$

An example of this ellipse is represented in Figure 1.4, where important points such as the maximum displacement $\hat{x} = \sqrt{\epsilon\beta}$ and maximum divergence angle $\hat{x}' = \sqrt{\epsilon\gamma}$ are presented.

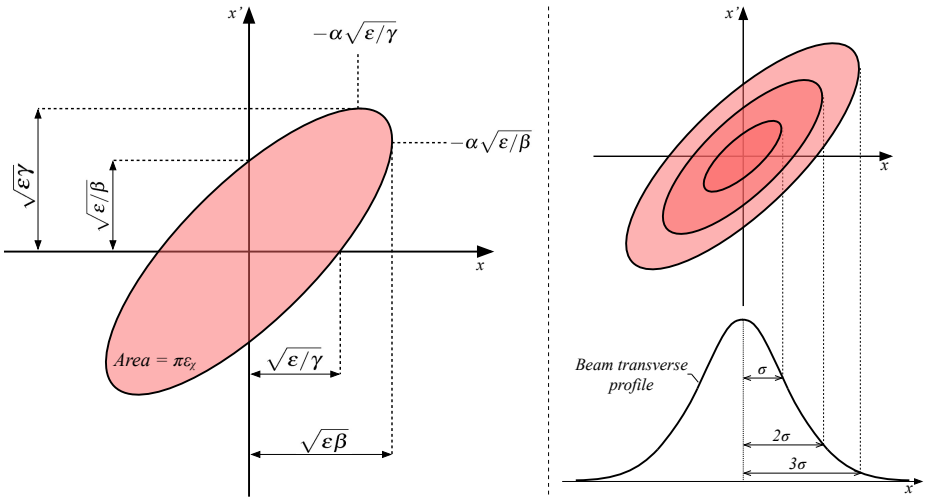

Figure 1.4: A charged particle phase space ellipse (left) where the maximum/minimum displacement and divergence are shown. The emittance ellipses corresponding to 1σ, 2σ and 3σ of the beam transverse distribution (right).

The area of this ellipse (e.g. 1.18) is called the geometric emittance. It is common to write it with the π in the unit, as shown in 1.19. The emittance is used as a measure of how divergent the particle trajectory is from the ideal one. As the dependence on s of all parameters in 1.17 suggests, the ellipse shape and inclination depends of the position (s) in the lattice. It is interesting to note that, the Liouville's theorem states that the emittance is conserved at any point in the lattice.

$$area = \pi\epsilon_x \ (mm\ mrad) \tag{1.18}$$

$$area = emittance = \epsilon_x \ (\pi\ mm\ mrad) \tag{1.19}$$

In a synchrotron, the particle beam is divided in a multitude of bunches. Each bunch has a certain number of particles, called the bunch population. The sum of the population of all bunches within the beam is the beam intensity. For now, the beam is assumed mono-energetic. Each particle in the beam has an ellipse similar to the one presented in 1.4. However due to the spread in their initial position and divergence, each ellipse has a unique size.

The *Beam Emittance* is defined as the geometric emittance of the particle with an ellipse encompassing all others, or in other words, the particle with the largest $\beta(s)$. There are however several definitions of emittance based on the percentage of the particles they encompass. The RMS emittance ϵ_{RMS} has 39 % of the beam, the 95 % emittance $\epsilon_{95\%}$ has

95 % and the σ emittance ϵ_σ has $\approx$ 68 %. The σ emittance, typically used with Gaussian beams, is preferred in this document.

It was said earlier that the emittance is conserved, this is however not true for the geometric emittance. As the beam is accelerated, the geometric emittance shrinks with $\sim 1/p$, with p the particle momentum, in a process called *adiabatic damping*. In order to account for this effect, the *normalised* emittance, denoted ϵ_n, is introduced :

$$\epsilon_n = \beta_r \gamma_r \epsilon_\sigma \ (\pi \ mm \ mrad) \tag{1.20}$$

In either form, a small beam emittance shows that the beam is compact and the particles comprising it have a low divergence, thus is a direct measurement of the beam quality.

One way to monitor the beam emittance is to measure the beam profile and extract the *transverse beam size* (noted σ). These two quantities are linked by

$$\sigma = \sqrt{\epsilon\beta} \tag{1.21}$$

where β is known from the lattice.

The particles comprising the beam are typically arranged in a Gaussian spatial distribution. As a consequence, the transverse beam size is approximated to a value encompassing a certain percentage of the total particle count. In the case of the Gaussian distribution, the beam size is taken as an integer of the distribution's standard-deviation. An example of this effect is presented in Figure 1.4 (right).

The assumption that the beam is mono-energetic was made earlier. This is in practice hard to achieve and the momentum spread, $\Delta p/p_0$, is introduced to account for off-momentum particles. *Dispersion* is the effect of the momentum spread on the magnetic rigidity of the lattice dipoles ($\rho = \frac{p}{Bq}$). Particles with a momenta larger than the ideal particle ($p > p_0$) have a larger orbit radius, while particles with a smaller momenta ($p < p_0$) have a smaller orbit radius. Dispersion can be accounted for by adding the momentum spread to Hill's equations. This results in the addition of a new periodic function $D(s)$, called the *Dispersion function*, representing the effect of dipoles on off-momentum particles. Dispersion directly affects the beam size and emittance, changing

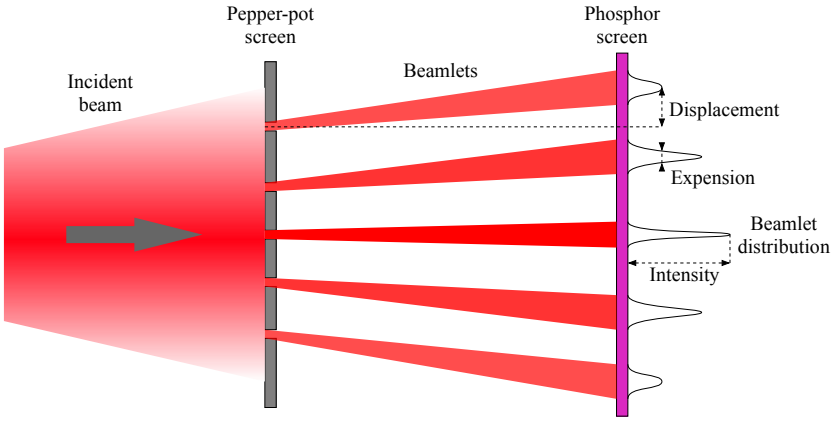

Figure 1.5: The pepper-pot emittance measurement method. The incident beam (red) is screened by the pepper-pot mask, the resulting beamlets are then imaged by a phosphor screen.

1.21 into:

$$\sigma = \sqrt{\epsilon\beta(s) + \left(D(s)\frac{\Delta p}{p_0}\right)^2} \tag{1.22}$$

where $D(s)$ and $\beta(s)$ are approximated from the lattice and/or indirectly measured [15]. σ, $\frac{\Delta p}{p_0}$ and ϵ are measured from the beam. Despite the addition of the dispersion, it is still possible to use 1.21 in a section of the machine where the dispersion is low ($D(s) \approx 0$) or with a beam with no momentum spread ($\frac{\Delta p}{p_0} \approx 0$).

Directly measuring emittance is possible, using methods such as the pepper pot, slits or quadrupole scan. Figure 1.5 represents the pepper pot method. A screen with an array of identical holes is inserted in the beam path. The beam is then divided in smaller *beamlets*. After a short free flight, these are imaged by a phosphor screen (or other detector). The beamlets displacement, transverse expansion and intensity are used in conjunction with the apparatus geometries to reconstruct the original beam transverse position and divergence.

In the context of an operational accelerator, it is however preferable to measure the beam size and momentum spread instead. Emittance measurement devices usually require a dedicated beam line and only allow to measure the emittance at a single point in time, as the measurement is destructive. On the other hand, beam size and momentum spread measurements can be non-destructive and therefore repeated throughout the life of the beam.

The derivations presented in this section are taken from [16], while resources regard-

ing momentum spread and direct emittance measurements are available here [17, 18] and here [19] respectively. The next section presents current methods used to measure the beam size.

1.3 Beam size measurements

Depending on the measurement method, either the full (x, y) transverse distribution (referred as beam spot) or a one dimensional distribution (referred as beam profile) is measured. The measurement methods, can be sorted in two class; intercepting and non-intercepting. We define as intercepting, methods where the act of measurement is noticeably disturbing the beam (e.g. causing a blowup of the emittance). While non-intercepting methods do not affect the beam. This definition highlights the main advantage of non-intercepting techniques, i.e. their measurement can be performed on production beam and be repeated several times within a cycle (for circular machines). A comprehensive list of measurement methods is presented in the next two subsections.

1.3.1 Intercepting Measurements

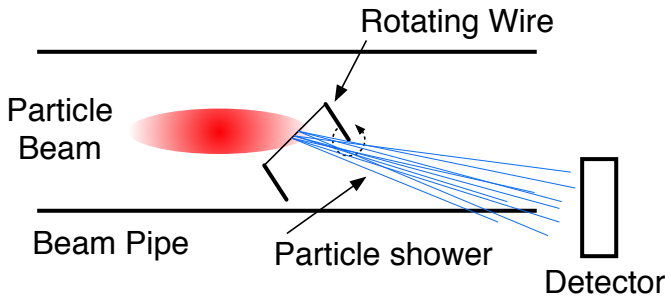

Figure 1.6: A rotational wire scanner passes a thin carbon wire through the beam (red). The intensity of the shower of secondary particle is measured with a detector downstream of the wire.

1.3.1.1 Wire Scanner (WS)

A Wire Scanner (WS) [20], depicted in Figure 1.6, is a device measuring the beam profile by scanning a thin wire ($\leq$30 µm) through the beam. The secondary-particle shower generated by the beam/wire interaction is recorded by a scintillator or diamond detector placed downstream of the wire [21]. The beam profile is then reconstructed by correlating

the wire position with the signal intensity. The measurement resolution is driven by the wire position knowledge, wire speed, mechanical properties (thickness, deformation from acceleration) and detector sensitivity.

The main drawback of a WS is the limited lifetime of the scanning wire. Depending on the beam intensity and energy, the total number of scans may range from none to a few thousands before the wire breaks and need to be replaced [22]. Efforts are ongoing to find new materials for the wire, such as carbon nano-tubes to improve WS reliability.

The wire scanner relative simplicity and absence of radiation sensitive components has allowed it to become an ubiquitous beam profile monitoring device. At CERN, they are installed in all circular accelerators. They are considered a reference and are commonly used to calibrate other instruments.

1.3.1.2 Secondary Emission Monitor (SEM)

Secondary Emission Monitors (SEM) measure the beam spot by inserting a grid of thin metallic wires into the beam path. The current generated by the interaction of the beam with the wire is recorded.The beam spot is then reconstructed by correlating the wire position with the measured current.

The resolution of SEM is limited by the wire diameter and spacing, which is usually in the range of a few micrometers for the former and hundreds of micrometers for the latter. This arrangement allows the grid to intercept few percents of the beam [23], which makes it well suited for low energy beams, where screens cannot be used. Moreover SEM perform single shot measurements, making then very useful in linacs and transfer-lines during beam setup periods.

1.3.1.3 Beam screen interaction

There are currently three methods which rely on the interaction of the beam with a thin screen to infer the beam profiles: scintillation screens; Optical Transition Radiation (OTR) and Optical Diffraction Radiation (ODR). In all cases light emitted by the screen is used to infer the beam spot. A schematic for each method is presented in Figure 1.7.

The scintillation screens method [24] uses the light emitted by the fluorescence of the screen by the beam traversing it. This method produces a large amount of light and is therefore well suited for low intensity beams. It however suffers from bulk and pile-up effects which can cause a blur of the recorded beam spot

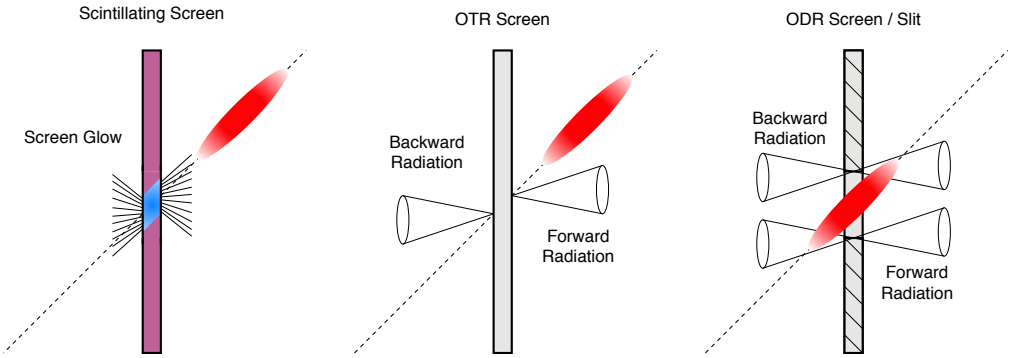

Figure 1.7: A scintillation screen (left), OTR screen (middle) and ODR screen (right).

The OTR method [25] uses the phenomena of Optical Transition Radiation, where charged particles emit light when they cross the boundary between two material with different dielectric constant. OTR is advantageous because the light emission is fast and exclusively originates from the surface of the screen, which allows to use very thin screens. This mitigates the aforementioned drawbacks of scintillation screen at the cost of producing only a fraction of the light.

With these two methods, the light intensity distribution across the screen surface is representative of the beam spatial distribution. This distribution is then recorded by a set of optics and camera.

These methods suffer from the degradation of the screen and large emittance growth caused by the beam/screen interaction. This limits the use of screens to beams with relatively low intensity and high energy (>20 GeV/c) for very short measurement period.

The ODR method [26, 27] fixes the screen degradation issues by relying on Optical Diffraction Radiation, where light is emitted from the screen by the close proximity of moving charged particles. In practice, the beam passes through a narrow slit carved into the screen, emitting light at the edge of the slit. The beam profile is then reconstructed from the ODR intensity distribution.

This method is mainly limited by its geometry requirements. The beam must be close to the slit in order to produce a detectable amount of light, while the beam has to be small compared to the slit in order to have a sensitivity sufficient to measure the beam profile. This restricts the use of ODR to the measurement of very low emittance beams, such as those obtained in lepton machine.

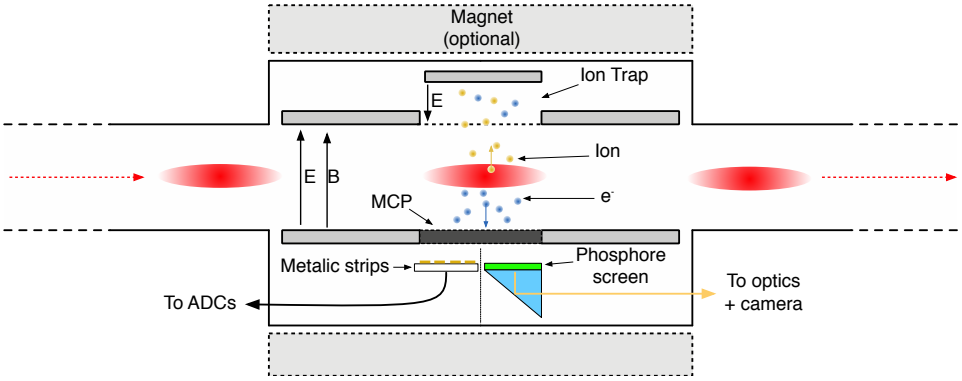

Figure 1.8: Representation of a typical BGI profile monitor. The beam (red) travels from left to right, the combination of an electric and magnetic field channels ionisation electrons toward a detector. Two detection system are presented, a metal strip (left) and optical (right) system. MCP(s) (bottom) amplify the ionisation electron signal while an ion trap (top) prevent the ions to generate a secondary electron signal.

1.3.2 Non-intercepting measurements

1.3.2.1 Beam Gas Ionisation (BGI)

A Beam Gas Ionisation profile monitor (BGI) is a device using the ionisation products (electron or ions) produced by the beam/rest gas interaction to infer the beam size. Assuming a homogeneous distribution of the rest gas, the initial distribution of the ionisation products is directly proportional to the beam spatial distribution. In the case of electrons, a magnetic field parallel to the drift field is introduced to limit the potential for measurement error caused by beam effects. The beam profile is recorded by transporting the electrons or ions toward a detector using an electric drift-field. The signal, collected by the detector, is then integrated for a given time to create a beam profile. Figure 1.8 presents the concept of a BGI.

Two types of detector are commonly used in BGIs, an optical system [28] or a charge collection system [29]. Both the optical and charge-collection systems require the ionisation products signal to be amplified by MicroChannel Plates (MCPs) [30] to allow for detection. MCPs convert a single primary electron or ions into a shower of secondary electrons with a gain in the 10^4 to 10^7 range. The substantial gain of MCPs comes at the cost of introducing a point spread function, fundamentally limiting the detection resolution. Besides, a gas injection system may be used to increase the gas pressure locally, further improving the signal.

The optical detection system uses a phosphor screen to convert the MCP electrons into photons. These are then sent to a camera using a set of in/out-vacuum optics. While

the charge collection system uses metal strips and ADCs, correlating the strip position with the charge it measures.

BGIs are currently limited by the inhomogeneous gain loss and limited lifetime of MCPs; which lead to frequent re-calibration of BGIs or when the gain becomes too small, to the replacement of the MCPs. Other limitation include, the frequent radiation-induced failure of the read-out cameras and the distortion in the measured profile caused by the beam space charge and ionisation process.

CERN is currently using seven BGIs. Six based on optical systems, four at the LHC (2 per beam line) [31] and two at the SPS [28]. The last one, installed in LEIR is strip based [29]. Other laboratories such as Fermilab [32] or KEK [33] also successfully build and operate BGIs.

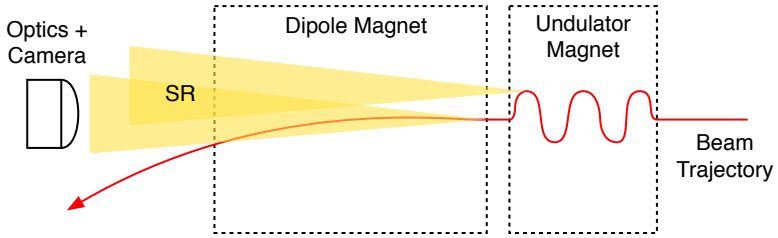

Figure 1.9: A representation of a synchrotron light monitor. The synchrotron light generated by the bending of the beam by a dipole or undulator magnet is used to reconstruct the beam profile.

1.3.2.2 Synchrotron Radiation (SR)

Synchrotron radiation monitors take advantage of the synchrotron light emitted by the beam, when passing through a dipole or special undulator magnet, to measure the beam spot. The SR light is collected and directed outside of the beam vacuum by a complex optical system placed downstream of the magnet(s). The beam spot is then either directly imaged or measured by an interferometer. The appropriate method is determined from the beam properties (size, momentum) and available magnet(s). Additionally, the beam divergence [34] and longitudinal profile [35] can be measured.

Synchrotron radiation monitors are advantageous due to their ability to continuously measure the beam spatial distribution and divergence. However they require to be calibrated against another device, such as a wire-scanner, to provide meaningful measurements. Moreover the dependency of SR wavelength with the beam energy, renders continuous measurement challenging. For example in the LHC, separate optical paths and

magnets are used to measure the beam at injection and flat-top. SR monitors are widely used in light sources and HEP accelerators such as the CERN SPS and the LHC [36]. A representation of a SR monitor is presented in Figure 1.9.

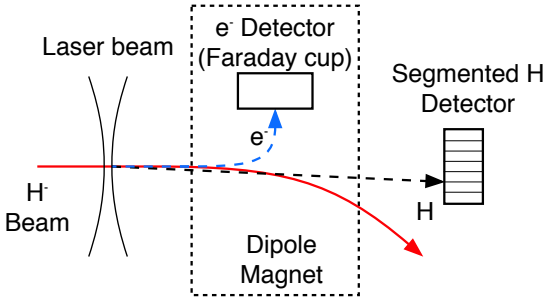

Figure 1.10: A pulsed laser beam strips electrons of an H^- ion beam. The resulting Hydrogen atoms or electrons are then used to reconstruct the beam profile or the beam emittance.

1.3.2.3 Laser Wire-Scanner (LWS)

Laser Wire Scanners (LWS), represented in Figure 1.10, are relatively new devices used in H^- linacs. They use a pulsed laser to strip electrons from the H^- ions. The laser is scanned across the beam and the resulting free electrons are measured by a faraday-cup. The beam profile is then reconstructed by correlating the laser position with the amplitude of the measured signal. Alternatively, a segmented detector can be used to measure the neutralised H atoms distribution at the end of the beam line. The beam emittance is then reconstructed from the H distribution and laser position information. In addition, the beam momentum spread can be retrieved from the striped electrons using a proper measurement stage [37].

Laser wire scanners, as opposed to wire-scanners (1.3.1.1) and SEM (1.3.1.2), are not limited by the beam intensity. This makes them particularly suitable to measure high current beams. Moreover, the ability to directly measure the beam emittance is Some limitations of LWS include the dependence of the ionisation yield to the laser properties, requiring to continuously monitor them. Furthermore, LWS require multiple shot in order to be complete each measurement. They have been successfully operated in BNL Linac [37] and CERN Linac4 [38].

1.3.2.4 Beam Induced Fluorescence (BIF)

Beam Induced Fluorescence monitors measure the beam spot by collecting the light emitted from the fluorescent rest-gas after the beam passage. Depending on the vacuum quality and beam characteristics, the injection of a noble gas may be required to increase the signal strength and tune the dynamic properties of the light emission. However, the pressure required to acquire a meaningful signal ($\approx 10^{-6}$ mbar) might be incompatible with modern accelerator requirements.

In order to alleviate this issue, an alternative technique consists in injecting a supersonic gas sheet across the beam path. This has the advantage of providing a very localised pressure increase. By tilting the gas sheet relative to the beam trajectory, it becomes possible to image the beam spot with a pair of cameras.

Beam induced fluorescence monitors have been successfully operated in facilities such as BNL [39] and GSI [40]. The main advantage of BIF monitors is the fact that they do not require a magnetic field to work, making them potentially more compact than BGIs.

1.3.2.5 Beam Gas Vertex (BGV)

A beam gas vertex monitor measures the beam spot by finding the origin of the vertices of particles produced from the beam / rest gas inelastic interaction. A demonstrator device recently installed at the LHC, inspired by techniques developed by LHCb to measure the beam profile [41], uses multiple Scintillating Fibre (SciFi) [42] planes in order to record the vertices of the incoming particles. A computer cluster is then used to reconstruct the vertices and find their origin. Figure 1.11 provide a simplified representation of the BGV. In order to tune the interaction rate to a suitable level, neon gas is injected in a special thin-wall vacuum chamber designed to reduce the amount of unwanted secondary scattering. The current BGV has successfully demonstrated its ability to measure the beam spot, future work will aim at improving measurement speed and accuracy. A complete description of this project is available in [43–45].

1.4 Thesis Overview

The LIU project motivated the need to monitor the LHC-type beams in the PS throughout the cycle at 1 kHz. Furthermore, the limitations of existing profile monitors and the availability of key technologies presented the opportunity to propose a new concept for

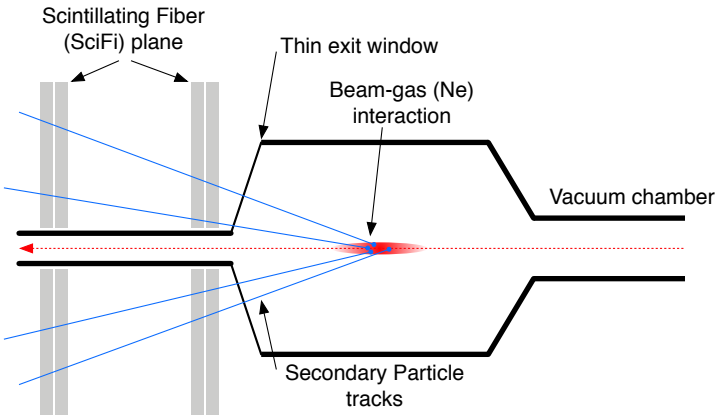

Figure 1.11: Representation of the BGV detector. Particles from a bunch (red) collide with Ne gas atoms, creating a shower of secondary particles. These are detected by a tracker and their origin found.

the PS-BGI. This new instrument would allow to gain unprecedented beam diagnostic insights.

The development of a novel BGI design with a detection system based on Hybrid Pixel Detectors (HPD) is introduced in this work. This detection system is, for the first time, directly installed inside the primary beam vacuum. Such configuration is required to remove the need for MCPs, enabling for the direct detection of the ionisation products. The HPDs high spatial and temporal resolution grants the possibility to continuously measure the profile of individual bunches. Their intrinsic radiation tolerance makes them perfectly suited for the radiation levels found at BGIs locations, increasing the robustness of the detection system. Moreover, their small form factor allows to reduce the aperture needed for the correction magnet, reducing its size / cost or granting a higher field strength for a similarly sized magnet.

This new BGI concept, along with the simulation needed to validate it are detailed in Chapter 2. The transition from concept to a proper design is presented in Chapter 3. Chapter 4 emphasises the design, fabrication and testing of the HPD based detector. The assembly and installation in the PS, followed by the instrument preparation and first ionisation-electrons measurements of the completed PS-BGI are presented in Chapter 5. Chapter 6 details the post processing chain required to filter the PS-BGI data and to reconstruct the beam profile. Measurements of the LHC-type beams, along with performance measurements and comparisons with the PS wire-scanner and beam position monitor system are presented in Chapter 7. An outlook and conclusion of this thesis work is given in

chapter 8.

Chapter 2

Conceptual design

The PS-BGI is required to measure the LHC type beams in the CERN Proton Synchrotron (PS). These are presented in Section 2.1. To better understand the instrument concept, its performance requirements are given in Section 2.2. The PS-BGI conceptual design is then detailed in Section 2.3. The concept was validated by simulations, these are presented in Section 2.4 and their results are given in Section 2.6.

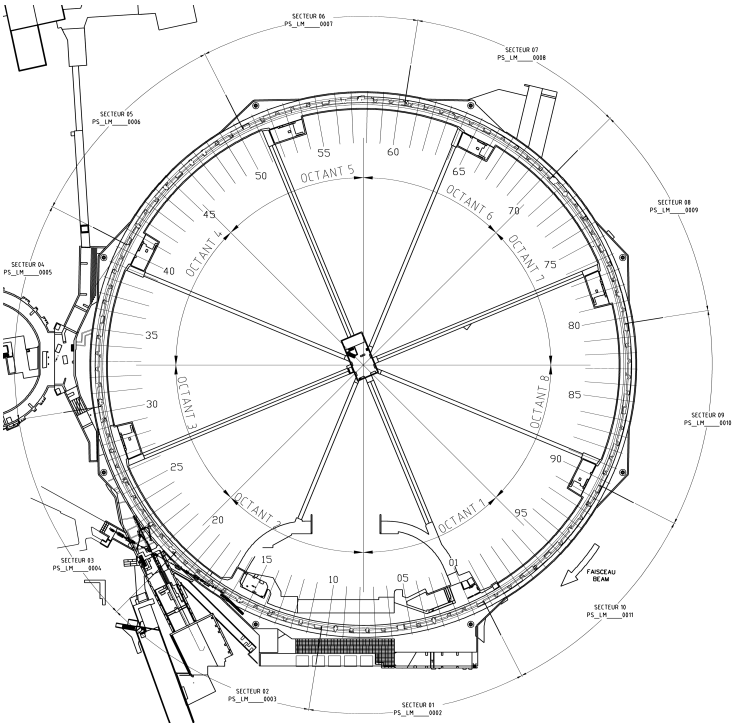

Figure 2.1: The CERN Proton Synchrotron.

2.1 The CERN Proton Synchrotron

The CERN Proton Synchrotron is a 628 m long circular accelerator comprising 100 dipole magnets operated with fields from 0.1 T to 1.2 T and can accelerate protons up to 25 GeV. Its complex Radio Frequency system allows it to perform most of the *beam gymnastics* required for CERN applications. The term beam gymnastics refers to the longitudinal manipulations done on the beam by the RF system e.g. bunch splitting, bunch merging and bunch rotation.

The Proton Synchrotron was first operated in 1959, where it was for a time the most powerful particle accelerator in the world. Nowadays, its main mission is to accelerate and shape proton and lead-ion beams for a broad range of users, including LHC, the Anti-proton Decelerator and the East/North areas. Figure 2.1 shows a technical diagram of the PS, a full virtual visit is available at Ref [46].

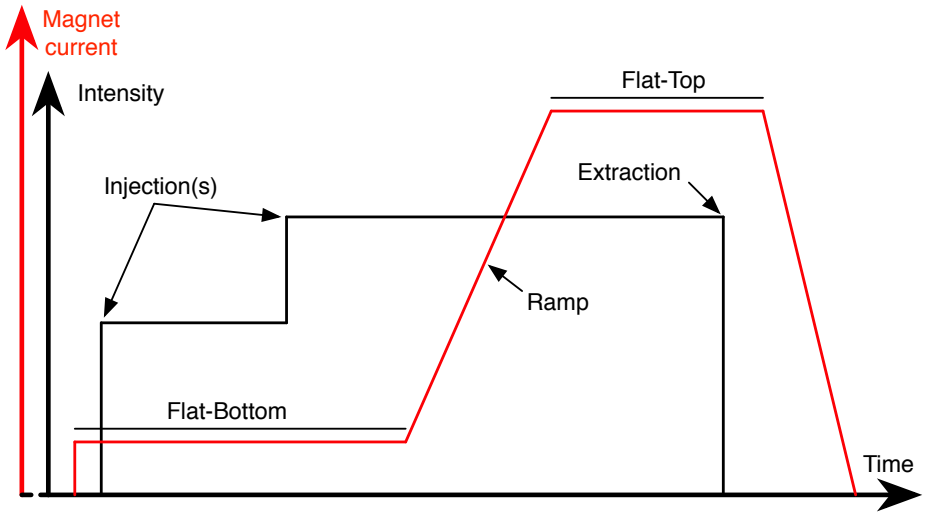

Figure 2.2: The PS proton cycle.

2.1.1 The PS cycle

A proton cycle starts with a single or double batch *injection* from the PS Booster, each batch injecting up to four bunches. During this injection period, referred to as *flat-bottom*, the dipole strength is at its minimum and the beam is not accelerated. Once the injection is complete some beam gymnastics may be performed. The beam is then accelerated and the dipoles strength follows a characteristic *ramp*. At the end of the acceleration, the magnets stop ramping, reaching *flat-top*. The beam may undergo a few more RF

Table 2.1: Beam parameters for the main LHC beams at the PS. The emittance values are for 1σ and normalised to $\beta_r\gamma_r$.

	Nominal		BCMS	
	Injection	Extraction	Injection	Extraction
Energy [GeV]	1.389	25.445	1.389	25.445
Momentum [GeV/c]	2.129	26.366	2.129	26.366
Proton per Bunch [10^{10}]	156 (325)	13 (22)	70	11.5 (22)
Bunch Spacing [ns]	327	25	254	25
Bunch Count	6	72	8	48
Bunch Length ($4\sigma_z$) [ns]	195	< 4.2	160	< 4.2
Revolution Time [µs]	2.3	2.096	2.3	2.096
ϵ_h [mm mrad]	2.66	3.16	1.4	1.6
ϵ_v [mm mrad]	2.08	2.9	0.9	1.15
σ_h @psbgi [mm]	3.7	1.14	2.69	0.81
σ_v @psbgi [mm]	4.54	1.5	2.98	0.95
$\frac{\Delta p}{p_0}$ (10^{-3})	0.9	0.4	0.9	0.4

operations before it is *extracted*. The magnets are then returned to their initial state in anticipation for the next cycle. The length of a PS cycle vary from one to three basic periods (1.2 s). A simplified representation of a typical PS cycle is shown in Figure 2.2.

2.1.2 LHC Beams at PS

The BGI is intended to measure the profile of the LHC beams in the PS. This corresponds mainly to two beams, the nominal LHC beam and the Batch Compression Merging Splitting (BCMS) beam. The parameters for these beams are given in Table 2.1.

2.1.2.1 Nominal LHC beam

The nominal LHC beam is used for the collisions at the LHC. For this reason, it must have a low transverse emittance and a relatively high intensity. Moreover to minimise the filling time of the LHC, as many bunches as possible must be produced per cycle.

The nominal LHC beam is produced by injecting two batches of four and two bunches respectively. These are then split in three, before the ramp, to make 18 bunches. After reaching flat top, the bunches are split in two another two times to reach a total of 72 bunches. The bunches are then rotated longitudinally to prepare them for injection in the Super Proton Synchrotron. This process compresses the bunches to allows them to match the SPS radio-frequency cavities harmonic.

This beam is the most challenging to measure due to the constant variation of the bunch intensity, size and number.

2.1.2.2 BCMS beam

The BCMS beam is another beam used for the collisions at LHC. Its main particularities are to allow for a higher bunch intensity while having a smaller emittance than the nominal LHC beam. This comes at the cost of producing only 48 bunches instead of 72, reducing LHC filling time efficiency. The lower number of bunches is however useful to mitigate the production of electron clouds in the SPS and LHC.

The BCMS beam is produced by injecting two batches of four bunches. These eight bunches are then merged in four bunches to be immediately split in three, reaching 12 bunches. The beam is then accelerated and the bunches are split in two another two times at flat-top, extracting a total of 48 bunches.

2.2 Instrument requirements

The basic operational requirement for the PS-BGI is to provide, for the first time, continuous profile measurements of the LHC beams and individual bunches at a rate of 1 kHz during the full PS cycle. The measurement accuracy and precision shall be less or equal to 1 % and 2.5 % respectively. The fully operational device should also be able to measure individual bunch profile on a turn by turn basis (one profile per bunch per turn). As will be demonstrated in Chapter 7, this last requirement is difficult to achieve without the addition of a gas injection system.

2.3 PS-BGI design

The concept for the new PS-BGI is presented in Figure 2.3. The instrument is placed in the primary PS vacuum inside a specially designed vacuum vessel. The PS beam ionises the rest gas. While field shaping elements produce a guiding electric field, diverting the ions to an ion trap and translating the electrons to the detector.

In order to meet the required measurement rate and accuracy, without the addition of a gas injection system, the PS-BGI uses a detection system based on the Timepix3 (TPX3) [47] hybrid pixel detector. HPDs can detect the ionisation electrons directly, removing the need for any signal amplification such as Micro-Channel Plates and gas injection.

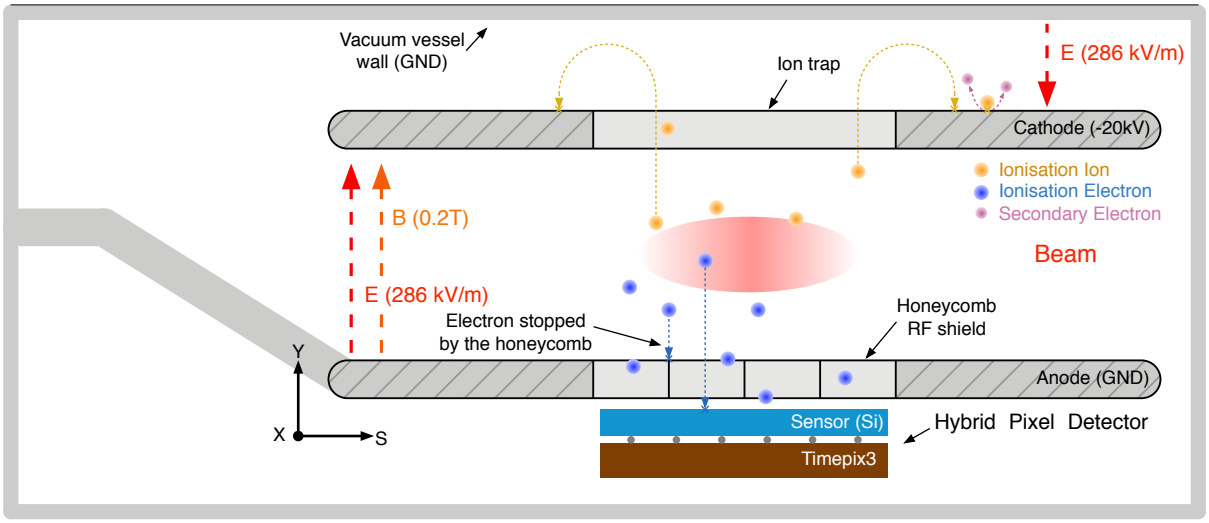

Figure 2.3: The PS-BGI concept. The beam, represented by a red arrow, ionises the rest gas. The resulting electrons are directed to the hybrid pixel detectors by the combination of an electric and magnetic field. The same electric field is used, in conjunction to an ion trap, to prevent the ions from creating a secondary-electron signal.

The time of arrival, position and energy for each detected particle is recorded, making it possible to distinguish between bunches and beam revolutions. Moreover, this information is directly digitised, making the data transmission more robust to the noise caused by the accelerator. The Timepix3 is designed to be extremely radiation tolerant [48]. This makes it suited for several years of use in the PS, reducing unexpected downtime and the need for maintenance.

Nonetheless, these advantages come at a cost. To work, the detector has to be installed inside the primary beam vacuum. This has never been done at CERN before and no readily available solution existed. Moreover the effects of the PS environment inside the beam pipe on the HPDs, such as the beam wakefield, were largely unknown. The HPDs require a state of the art readout system and none existed that could survive the expected level of radiation close to the instrument (0.1 krad to 1 krad). Finally, no software and techniques for the signal processing could be reused from another instrument. This meant that the PS-BGI had to be entirely designed from scratch and a long commissioning period would be required.

The detailed motivations and design of the detector are introduced in Chapter 3 and 4. The next subsections presents more insights in the field shaping, ionisation electrons production and transport. For the rest of this document, a Cartesian coordinate system centred at the beam design orbit is used as reference. The beam travels along the Z axis

or longitudinal axis, the X axis is the transverse horizontal or measurement axis and the Y axis is the transverse vertical axis. Unless specified otherwise, every dimension is given with the following order X, Y, Z.

2.3.1 Electric field shaping

A $-20\,\mathrm{kV}$ voltage is applied to a cathode to provide the ionisation electrons with sufficient kinetic energy to be detected by the HPD. Together with an anode electrode at ground potential, both electrodes have a surface of $240 \times 240\,\mathrm{mm}^2$ and are spaced by 70 mm, the vertical beam acceptance at this location. The detector is placed, inside a Faraday cage, roughly 10 mm below the anode. The Faraday cage protects the detector from electromagnetic effects of the beam wakefield. A $50 \times 20\,\mathrm{mm}^2$ (X, Z) rectangular opening in the anode allows ionisation electrons to reach the detector. In order to keep the Faraday cage effective, this opening is partially closed with a steel honeycomb structure. The dimensions and configuration of the anode and cathode emanate from a design exploration campaign where several competing designs were simulated. This work was performed during my master studies, prior to the start of my PhD, details are available here [49]. The results of the electrostatic simulation of the final design are presented in section 2.6.

The emerging electric field has a value of $-286\,\mathrm{kV\,m}^{-1}$ and is mostly parallel with the vertical axis of the instrument. The quality of this field is defined by the absence of transverse components (X and Z axes), which would result in a drift of the ionisation electrons. The *good field region* is defined as the volume where the electric field quality is good enough to allow for profile measurements. This corresponds to a volume of $50 \times 70 \times 20\,\mathrm{mm}^3$, encompassing the largest envelope of any LHC beam with their maximum transverse excursion.

While most BGIs use side electrodes to improve their electric field quality, the large electrode and small spacing of this design allows to remove them completely. The absence of side electrodes simplifies the mechanical design and assembly, and relaxes the requirements of the high voltage distribution circuit. The quality of the electric field is discussed in section 2.6.

2.3.2 Detection using electrons

The choice of using the electrons over ions for the profile measurement is motivated by the required measurement speed. In order to measure the profile of individual bunches,

the signal from each bunch must be separate. This implies that ionisation products must reach the detector before the next bunch enters the instrument. Their drift time must therefore be less than 25 ns, the minimum bunch spacing. Electrons with 10 keV of kinetic energy only reach a Lorentz factor of 1.02. One can therefore derive the drift time t_{drift} of a particle subject to a constant electric field and starting at rest assuming non-relativistic mechanics with

$$t_{drift} = \sqrt{\frac{2xm}{qE}}, \tag{2.1}$$

with m the particle mass, q its charge, x the drift distance and E the electric field strength. With 45 mm of drift distance and an electric field strength of $-286\,\mathrm{kV\,m^{-1}}$, the expected drift time for electrons and hydrogen ions is 1.34 ns and 57.3 ns respectively. This result discards the use of ions for the PS-BGI.

A prerequisite for the proper function of a BGI is the absence of a transverse drift during the transport of the ionisation-electrons. Such drift would be detrimental to the instrument accuracy, introducing distortions in the measured profile. However, due to the beam space charge, ionisation process and inhomogeneity in the guiding electric field, the ionisation-electron acquire a transverse velocity; which causes a drift if left unattended. These effects and their mitigation is presented below.

2.3.3 Ionisation process

The ionisation process is responsible for the production of the electrons used to reconstruct the beam profile and participate to the distortion of this very same profile.

2.3.3.1 Signal production

The number of ionisation electrons / ion pairs (N_{ion}) produced by the passage of a single bunch in a BGI can be estimated with ([50] equation 1)

$$N_{ion} = D\sigma_p N_p P \frac{N_A}{RT} \tag{2.2}$$

where D is the distance of interest (usually the length of the detector), N_p the number of protons (or ions) in the bunch, P the vacuum pressure, N_A the Avogadro constant, R the ideal gas constant and T the gas temperature. σ_p is the total ionisation cross section of the rest gas for a given beam energy. The value of σ_p can be calculated using the Bethe

approximation [51]

$$\sigma_p(\beta^2) = \frac{4\pi a_0^2 \alpha^2}{\beta^2}\left[a_i ln\left(\frac{\beta^2}{1-\beta^2}\right) - a_i\beta^2 + b_i'\right] \tag{2.3}$$

where $\beta = v/c$ with v the projectile velocity, a_0 Bohr radius, α the fine structure constant. a_i and b_i' are empirical constants unique to each gas species ([52] Table II where $a_i = M^2$ and $b_i' = C$). The total ionisation cross-section for several gas species with proton projectiles is given in Table 2.2.

Table 2.2: Total ionisation cross sections for injection and extraction LHC type beams in the PS with molecular hydrogen, water, argon, carbon dioxide and xenon gas species.

	σ_p (p 1.39 GeV) [Mbarn]	σ_p (p 25.44 GeV) [Mbarn]
H_2	0.194	0.226
H_2O	0.78	0.948
Ar	0.924	1.158
CO_2	1.399	1.694
Xe	1.763	2.208

It is possible to estimate the ionisation rate by extending 2.2 with the number of bunch in the beam (n_b) and revolution frequency (f_{rev}), leading to

$$\frac{dN_{ion}}{dt} = N_{ion} n_b f_{rev}. \tag{2.4}$$

The ionisation rate expected for different beam with molecular hydrogen gas at 10^{-9} mBar is shown in Table 2.3.

Table 2.3: Ionisation (product) production by bunch, turn and ms.

	Nominal		BCMS	
	Injection	Extraction	Injection	Extraction
N_{ion} / bunch	10	1	5	0.9
N_{ion} / turn	63	72	38	43
N_{ion} / ms	27400	31320	16530	18705

Since these electron production number are rather small, the statistical error will play an important role in the measurement error of the instrument. The statistical error on the standard deviation of a Gaussian distribution is given by

$$\sigma_{stat\_err} = \frac{1}{\sqrt{2N_{count} - 2}}, \tag{2.5}$$

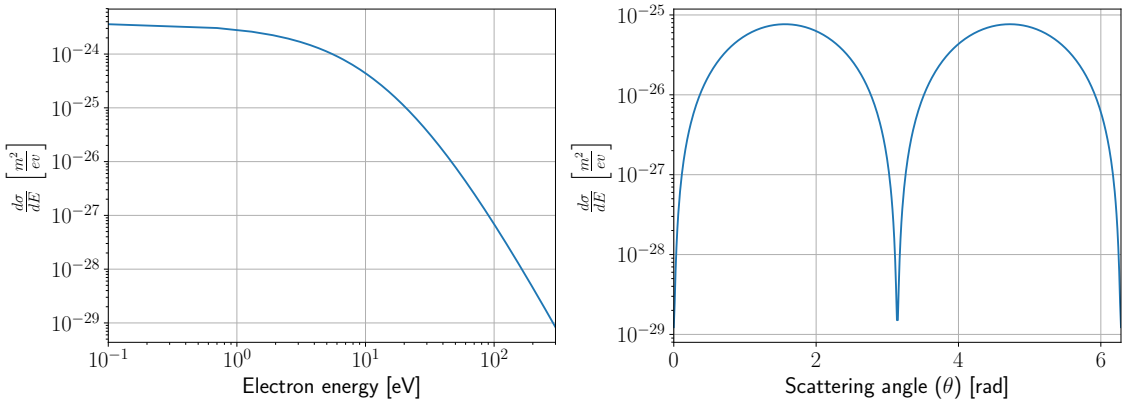

Figure 2.4: SDCS of the electron energy (left) and scattering angle (right) for the ionisation of hydrogen with 25 GeV proton beam.

with N_{count} the total number of counts in the distribution. To reach the required 2.5 % accuracy on the beam width measurement, one need $N_{count} \approx 5000$, which corresponds to a range of 70 to 130 beam revolutions. This range jumps to, 500 to 5000 revolutions for individual bunch profile.

It is good to keep in mind that this represents a rather conservative scenario. The gas composition is likely to comprise water and other heavier elements (in trace amounts) potentially increasing the production of electrons. In addition, the shift toward higher intensity beams for HL-LHC will roughly double the numbers presented in Table 2.3.

2.3.3.2 Profile distortion

As a result of the ionisation process, the electron / ion pair receives some kinetic energy. In the case of the electrons, this energy leads to a non negligible transverse drift during their transport to the detector. The energy and scattering angle cross section for the ionisation electrons can be estimated analytically using the Voitkiv approach [51, 53] for interaction with high energy projectiles. This approach works for simple atoms such as hydrogen and helium. The results are Single Differential Cross Sections (SDSC) for the production of electrons with a certain energy and scattering angle. An example is presented in Figure 2.4 for a 25 GeV proton beam interacting with hydrogen.

The left plot shows the cross-section as a function of the electrons energy while the right one shows the cross-section as a function of the scattering angle. One can see that for hydrogen, the electrons are more likely kicked perpendicular to the beam motion ($\frac{\pi}{2}$ and $\frac{3\pi}{2}$) with a relatively small energy (<50 eV). Moreover, this effect is symmetrical relative to the beam direction (π), there is no left/right preference. The simulations presented in

section 2.6 show that the measured beam profile is expected to broaden due to this effect.

2.3.4 Bunch space charge

The collection of charges within a particle bunch creates a non negligible transverse electric field. This field is called bunch space charge. It can potentially affect the BGI measurement by attracting or repulsing, at the moment of their creation, the ionisation electron and ions. The transverse field for a symmetric Gaussian bunch ($\sigma_x = \sigma_y$) is given by (adapted from [54]):

$$E(r,z) = \frac{N_p q}{(2\pi)^{3/2}\epsilon_0 \sigma_s r}\left(1 - e^{-\frac{r^2}{2\sigma^2}}\right) e^{-\frac{s^2}{2\sigma_s^2}} \tag{2.6}$$

Where q is the elementary charge, ϵ_0 the vacuum permittivity, $r = \sqrt{x^2 + y^2}$ the distance from the bunch centre in the transverse plane, s the distance from bunch centre in the longitudinal plane and σ / σ_s the bunch size in the transverse and longitudinal plane respectively. A solution for asymmetric bunches is given in [55].

The electric field is determined by the bunch population (N_p scaled with the longitudinal charge distribution) and its shape from the transverse bunch size (σ). An example for a BCMS bunch at injection, extraction is given in Figure 2.5

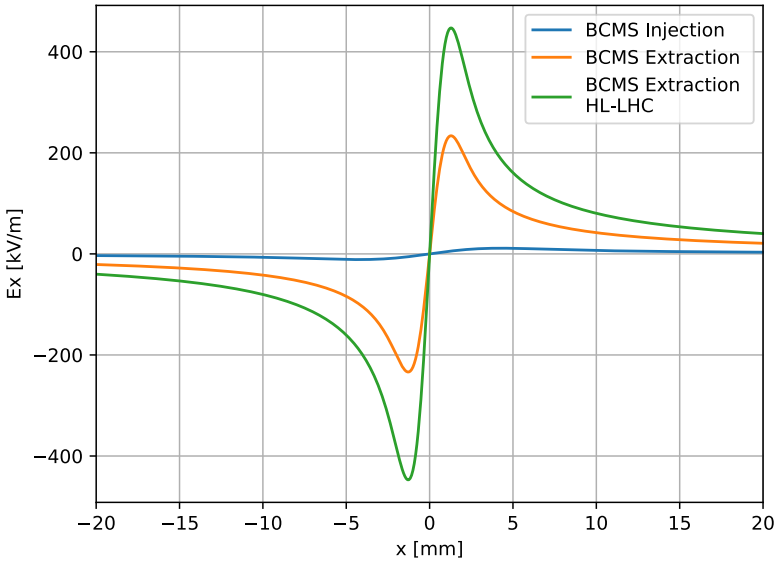

Figure 2.5: E_x for the BCMS beam at PS injection, extraction and extraction with the HL-LHC intensity.

The shape of the space charge electric field indicates that ionisation electrons tend to be pulled toward the bunch centre, resulting in a characteristic pinching of the measured beam profile. This effect is a major concern for the LHC BGIs [31]. Moreover, the field

amplitude increases largely from injection to extraction. This is caused by the beam size (σ and σ_s) shrinking during the ramp and from the bunch population increasing (for the HL-LHC case). The profile distortion caused by this effect is therefore more likely to be problematic close to extraction. Finally due to its strength, this effect is likely to be the dominating source of profile distortion in the BGI.

The profile distortion caused by the combined effects of the beam space charge and ionisation process are extensively studied in Ref [51, 56–58] and methods to correct for them are being investigated in Ref [59, 60]. Nowadays, the only proven strategy to mitigate the impact of these negative effects is the addition of a magnetic field.

2.3.5 Magnetic field

A magnetic field, collinear to the guiding electric field, forces the electrons into a gyration motion. This prevents them from drifting during their transport to the detector, limiting the measurement error. The gyration radius (r_g) and frequency (ω_g) are expressed with

$$r_g = \frac{m v_\perp}{|q|\, B} \tag{2.7}$$

$$\omega_g = \frac{|q|\, B}{m} \tag{2.8}$$

Where m is the electron mass, q its charge and B is the magnetic field strength. $v_\perp$ the electron speed perpendicular to B, is given by the transport effects (space charge, ionisation kick...). In order to limit the profile distortion, B should be large enough to ensure the electron gyration radius is much smaller than the beam width ($r_g << \sigma$).

In the PS-BGI, the magnetic field is set to 0.2 T. This value was, at first, selected based on the work of K.Satou and prior experience with the LHC BGIs, where no profile distortion is observed at injection (450 GeV/c). It was then later confirmed by the simulations presented in section 2.6.

An unwanted consequence of the BGI magnetic field is the deflection it induces on the beam trajectory. The beam deflection angle (θ) is given by

$$\theta = \arcsin\left(\frac{lqB}{p}\right) \tag{2.9}$$

where l is the magnet length, q the particle charge, B the magnetic field strength and p

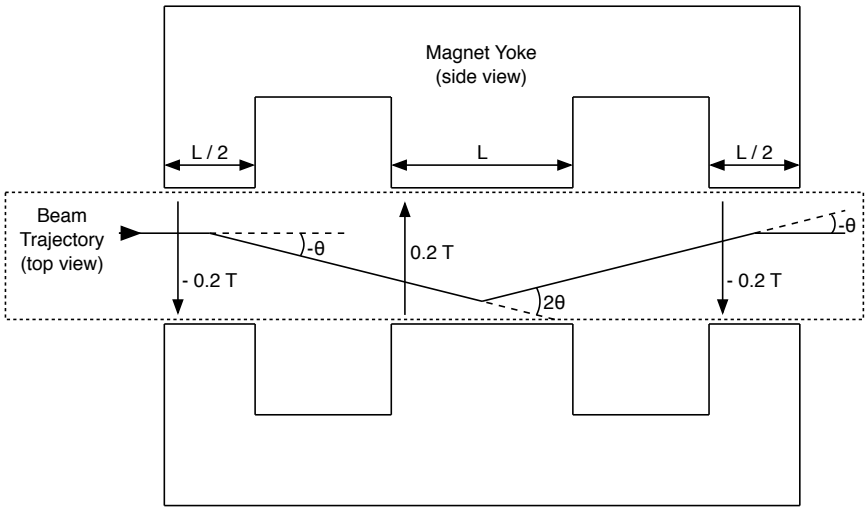

Figure 2.6: PS-BGI tri-pole magnet. The sum of the angular change on the beam trajectory caused by the magnet is null. For convenience, the beam trajectory is displayed from a top view perspective.

the particle momentum. The effective deflection (Δ) is then calculated with

$$\Delta = \tan\left(\frac{\theta}{2}\right). \tag{2.10}$$

Assuming a length l of 0.1 m, the deflection on a proton at injection in the PS is roughly 1.3 mm/turn, which can lead to the loss of the beam in a few micro-seconds. The solution to this problem is to design a self compensating magnet. The PS-BGI magnet was designed by the CERN magnet group, its concept is presented in Figure 2.6. The magnet comprises three poles, each with a 0.2 T field. The central pole, used for the BGI operation, has positive field. While the two other poles, twice shorter than the central one, have a negative field. When the beam enter the magnet, the first pole deflects it by an angle -θ, the second pole then deflect the beam by 2θ and the last poles deflects it back with -θ. The net sum of the deflection is therefore zero. This configuration guaranties that the net sum of the deflection caused by the PS-BGI magnet is null.

2.3.6 Ion trap

The ions resulting from the ionisation process are accelerated in the opposite direction to the electrons; they then collide with the cathode and create secondary electrons. These electrons are then accelerated towards the detector, creating a secondary signal. This signal heavily complicates the profile measurement and needs to be suppressed.

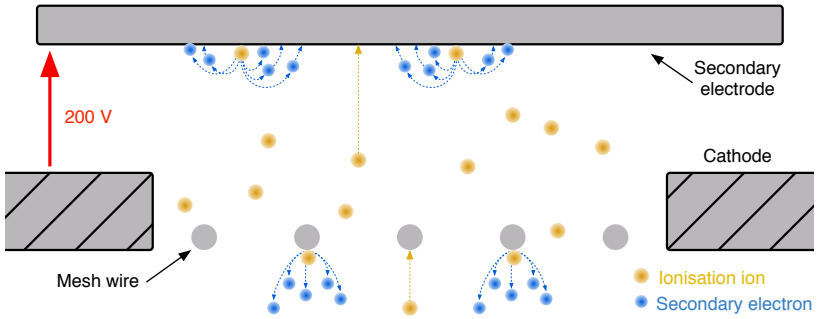

Figure 2.7: Classic ion trap design. Some ions hit the wire mesh, creating an undesirable secondary electron signal.

In order to prevent the ions from ever creating secondary electron a so called ion-trap is used. Despite its name, an ion trap is a contraption meant to prevent the secondary electrons from reaching the detector. The standard ion-trap design is presented in Figure 2.7. An opening, slightly larger than the detector, is made in the cathode to allow ions to pass. A second electrode is then used to introduce a small voltage difference between itself and the cathode. This small electric field is sufficient to prevent the secondary electrons falling back toward the detector. To prevent a degradation of the main guiding field, a fine wire mesh is used to close the trap opening. However, the wires used in the mesh are relatively large and a fraction of the ions collide with them. The resulting secondary electrons are then free to fall toward the detector, leaving a characteristic grid pattern.

In order to solve this issue, a new design is introduced in the PS-BGI, as shown in Figures 2.3 and 2.8. The wire mesh is removed, along with the secondary electrode and only the opening in the cathode is left. This design works based on the shape of the electric field created between the cathode and the vacuum vessel wall. This field is as strong as the main guiding field but due to its geometry it has a large transverse component. This large transverse field deflects the majority of ions entering the trap toward the backside of the cathode. In the centre of the ion-trap opening, the transverse electric field is slightly too weak to deflect the remaining ions all the way to the cathode backside before they are pushed back inside the main volume of the instrument. These ions are then closer to the ion trap wall during their second pass in the trap (going from above to below the cathode), giving them enough momentum to clear away from the trap opening and hit the frontside on the cathode. For both ions hitting the backside or frontside of the cathode, the electric and magnetic field present in the instrument prevent the secondary electrons to come back inside the detector region and create a background signal in the detector.

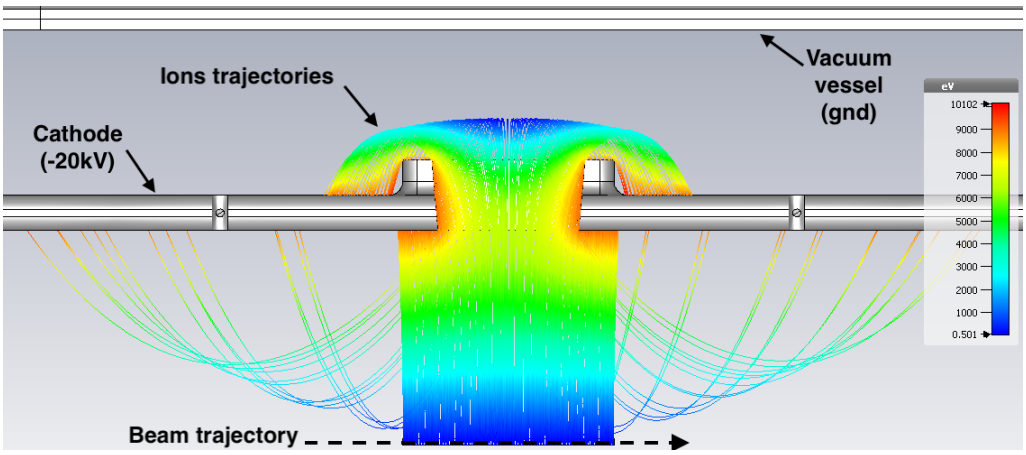

Figure 2.8: Ion tracking simulation of the novel ion trap design. The coloured lines represents the ions trajectories and energy. Due to the transverse electric field created by the trap, most ions are deflected toward the backside of the cathode. The remaining ions are deflected back inside the instrument volume and hit the cathode frontside. This prevents secondary electrons to reach the detector.

Figure 2.8 shows a particle tracking simulation, using CST studio [61], where hydrogen ions are deflected by the ion trap.

The transverse component of the electric field inside the trap is enhanced by making the hole wall longer than the cathode thickness. Moreover, to completely remove the possibility for secondary electrons to fall back toward the detector, these walls are slightly slanted.

The effects of this new design on the guiding electric field are not negligible. These are studied in the simulation presented in the next section. The original idea for this design belongs to K.Satou. This publication [62] provides further details on the design.

2.4 Simulation method

To ensure that the design choices made for the PS-BGI would allow for a relative profile measurement error below 1 %, the PS-BGI design was simulated. Since no available single simulation tool could completely simulate the instrument, the simulation was split between CST Studio and Virtual-IPM.

2.4.1 CST studio

CST studio is an advanced commercial tool-set for static and dynamic electromagnetic simulations and particle tracking. The tool comes with a full support for parametric 3D

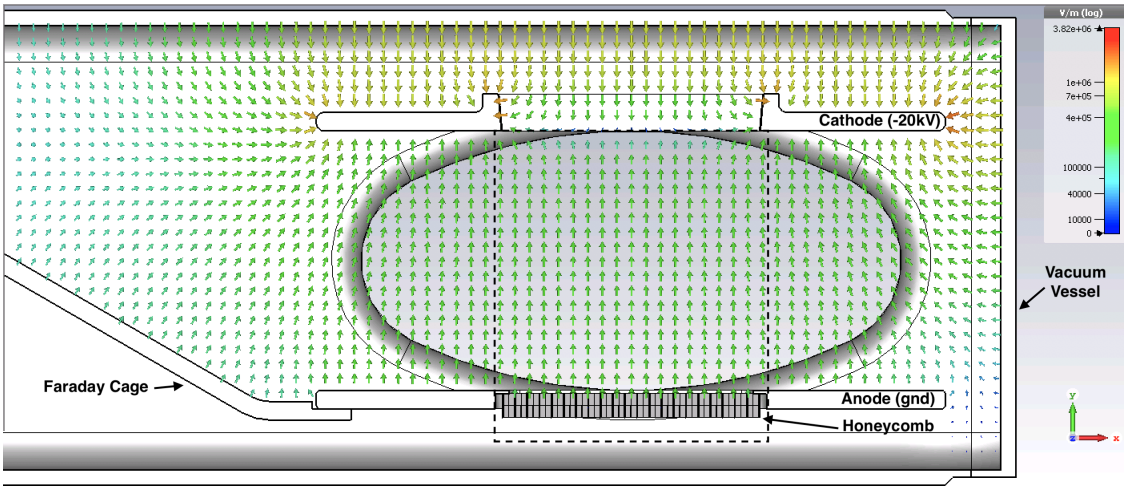

Figure 2.9: Example of a 3D electric field simulation with CST-studio. The field vectors are displayed on a cross section (XY). The large oval shape in the background is the PS beam pipe. The beam would be coming out of the page.

modelling, allowing the user to perform design exploration. This tool is typically used to simulate electron guns, RF cavities, antennas etc.

At the time of the instrument design, CST Studio could not simulate a high energy particle beam and the particle generation options were rather limited. For these reasons, CST studio was only used as an electrostatic 3D field solver. The CST 3D field solver uses a 3D model of the PS-BGI, the material and the electric potential of each individual parts of the 3D model as input to generate a 3D field map. A field map is a file containing the coordinates (X,Y,Z) and electric field vector components (E_x, E_y, E_z) of points in the simulation volume. The volume, in mm^3, exported for these simulation is [-45:45] in X, [-45:35] in Y and [-45:35] in Z.

An example of a CST studio simulation result is presented in Figure 2.9. The main elements affecting the electric field are present. The arrows represent the electric field direction and their colour, the field strength. A dashed line rectangle represent a cross-section of the volume exported as a field map. The field map resulting from the CST simulation is used as an input to Virtual-IPM.

2.4.2 Virtual-IPM

Virtual-IPM [63] is a modular simulation framework for BGIs. It is developed by D.Vilsmeier (GSI) and its creation is motivated by the absence of a simulation tool for precise and accurate simulations of BGI instruments.

The tool uses the beam physical properties, the instrument electric/magnetic field

and the vacuum properties in the instrument as input to simulate the beam space charge, ionisation process and motion of the ionisation products in the instrument. The beam physical properties are the bunch number, bunch spacing, bunch transverse and longitudinal particle distribution, particle type, particle momentum, and particle count per bunch. The vacuum properties are the residual gas species, pressure and temperature.

Virtual-IPM tracks the ionisation products using either the Runge-Kutta or Boris method. These methods compute particle velocity based on the electric and magnetic field present at their current location. The particles are them moved accordingly for a given time-step. The time-step is a user defined parameter. The electric and magnetic field can be manually set or imported as 3D or 2D field maps. Since it was impossible to access a field map from the early magnet design, simulations including a magnetic field assume a manually set field.

The simulation stops when all particles have hit the simulation boundaries or when the requested number of time step is reached. The tracking results take the form of a CSV file with all particles initial and final positions and momentum. These are then fed to a python script implementing the profile reconstruction.

2.4.3 Profile reconstruction

The method used to reconstruct the profiles from virtual-IPM results is relatively straight forward. The final transverse position for each electron, that reached the detector region, is summed in bins of 55 μm, the timepix3 pixel size. This depicts a rather perfect detector with no losses, misalignment or dead-regions. A Gaussian function is fitted to the resulting histogram to obtain the beam width (σ) and position (μ). The errors on the fit parameters returned by the fitting function are then used as uncertainty on the beam position and width. Finally a χ^2 goodness of fit test is performed to verify that the values resulting from the fit can be trusted. Figure 2.10 shows an example of beam profile obtained with this method.

The measured histogram is shown with blue data points, the vertical error bars are the Poisson error and the horizontal ones are the bin size. The expected Gaussian profile from the fit result is plotted as a red line with a +- 3 sigma interval in green. In the text box are given the mean, standard deviation, lowest bin count and integral of the profile distribution. The amplitude (P0), mean (P1) and sigma (P2) of the fitted Gaussian function are also stated.

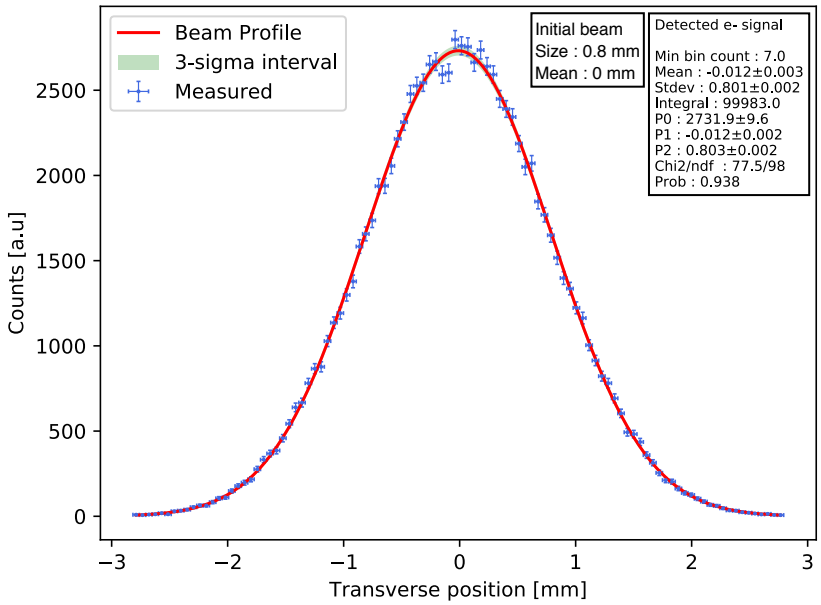

Figure 2.10: Example of a simulation result with a BCMS beam at extraction.

One might argue that the fitting step is unnecessary as the width and position of a Gaussian function is simply the standard deviation and mean of the underlying distribution. This is true as long as the distribution is perfect (e.g. no missing or over/under filled bin) and that it is truly Gaussian. This is, however, not often the case when considering all the effects causing distortions to the original ionisation electron distribution.

The method presented here is a simplified version of the one used for the real PS-BGI data-sets. For this reason the detailed method is introduced in Chapter 6.

2.5 Simulation layout

In order to make a first assessment of the guiding electric field, the electric field map from CST-Studio is evaluated (2.6.1). This map was generated using the 3D model of the instrument and a cathode electric voltage of $-20\,\mathrm{kV}$ as input. The individual components of the electric field (E_x, E_y, E_z) are integrated along the Y axis, from the beam centre (Y = 0 mm) to the detector (Y = $-45\,\mathrm{mm}$). Due to the irregular shape of the honeycomb RF shield, present in the CST-Studio simulation, small ripples are visible in the integrated fields (Figures 2.11, 2.12 and 2.13). The integrated electric fields provides a first order approximation of the energy (longitudinal and transverse) electrons will receive from the guiding field as they travel toward the detector. Although E_y and E_z do not directly affect

the profile measurement, large discrepancies in them could cause some electrons to drift outside of the detector region or to not get enough kinetic energy for detection.

Virtual-IPM is then used to study the individual and combined effect of the inhomogeneity of the electric field (2.6.2), ionisation process (2.6.3) and space charge (2.6.4) on the measured beam profile. To evaluate the influence of each perturbation, the simulations are at first performed without the addition of the magnetic field. It is then introduced (2.6.6) to assess its effectiveness at preserving the beam profile.

To evaluate the instrument margins in the electric and magnetic field strength, simulations are either run with 3D field map corresponding to a cathode voltage range of $-10\,\mathrm{kV}$ to $-20\,\mathrm{kV}$ for the electric field or $0\,\mathrm{T}$ to $0.2\,\mathrm{T}$ for the magnetic field. Moreover, since the magnet is separate from the rest of the instrument, the effect from a small misalignment ($0°$ to $10°$) between the magnetic and electric fields is studied (2.6.7). Finally the case of the HL-LHC beam is studied (2.6.8) to ensure the relevance of the PS-BGI in the future.

For all aforementioned cases, two values are evaluated, the difference between the beam position and the measured beam position ($\Delta\mu$) and the relative error between the measured beam width and the real one (σ_{err}). These are calculated with

$$\Delta\mu = \mu_{measured} - \mu_{beam} \tag{2.11}$$

$$\sigma_{err} = \frac{\sigma_{measured} - \sigma_{beam}}{\sigma_{beam}} \tag{2.12}$$

where $\sigma_{measured}$ and $\mu_{measured}$ are the beam size and position measured by the BGI. σ_{beam} and μ_{beam} are the real beam size and position given to virtual-IPM. A positive σ_{err} implies a measured profile larger than expected and vice versa. The error on these quantities is simply the error given by the fitting function. For clarity, $\Delta\mu$ is referred as *Beam position shift*. σ_{err} is referred as *beam width error*.

2.5.1 Virtual-IPM beam parameters

All simulations use the BCMS beam parameters at injection and/or at extraction (see Table 2.1). This beam is selected because of its small size, leading to a large space-charge. This makes it a worst case scenario, ensuring that the simulation result are conservative.

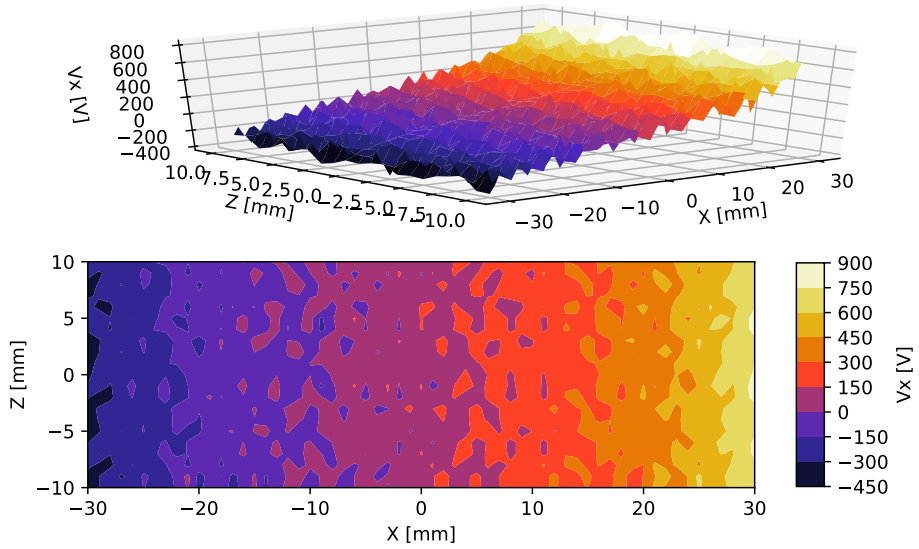

Figure 2.11: E_x integrated along the Y axis. Top: surface plot. Bottom: contour plot.

2.5.2 Virtual-IPM general parameters

In order to neglect the statistical errors, each simulation creates ≈ 100000 electrons (the real number is randomised by virtual-IPM). The time-step is set to 0.13 ps, corresponding to ≈ 10000 steps per electron. The total simulation time for the case with an extraction BCMS beam is set to 13 ns, while in the case of an injection beam it is set to 400 ns. These values are chosen based on the bunch length. Since the electrons reach the detector before the next bunch arrives, only one bunch is simulated. When the ionisation process is considered, the ionised gas is hydrogen. The simulation volume, in mm^3, is set to the ranges [-45, 45] in X, [-45, 35] in Y, and [-10, 10] in Z. This is slightly larger than the good field region of the instrument.

2.6 Simulation results

2.6.1 Electrostatic simulations

The integral along the Y axis, from the beam centre (y = 0) to the detector, for each component of the electric field map from CST-studio are presented in Figures 2.11, 2.12 and 2.13. For each, a surface plot and contour plot is given, the colour-map used is *CRMmap*. The integrals are presented for an area (XZ) slightly larger than the detector area ([-30:30] X, [-10:10] Z).

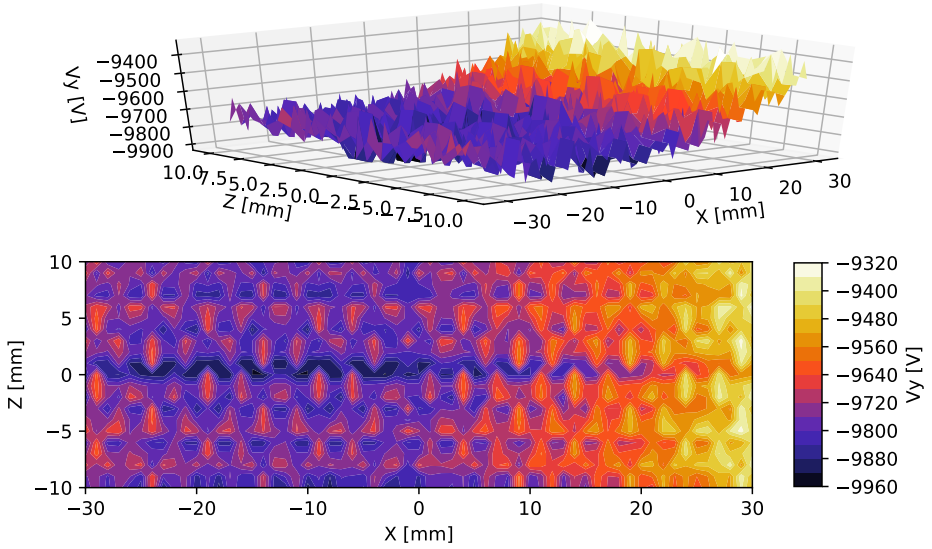

Figure 2.12: E_y integrated along the Y axis. Top: surface plot. Bottom: contour plot.

V_x is following a positive slope ($\approx 22.5\,\mathrm{kV\,m^{-1}}$) along X ranging from $-400\,\mathrm{V}$ to $800\,\mathrm{V}$, while it remains relatively stable along Z. This slope is large enough to noticeably shift the electrons trajectories. Its polarity hints that the electrons should globally have a positive drift. Moreover, the slope in itself should causes electrons within the distribution to drift more or less depending on their position along X, causing a broadening of the measured profile. The slope in V_x can be explained by the field line leaking to the vacuum vessel wall and Faraday cage. In addition, the asymmetry in the mechanical design along the X axis (see Figure 2.9) shifts the zero crossing to $\approx -10\,\mathrm{mm}$.

V_y is relatively stable around $-10\,\mathrm{kV}$, with fluctuation few hundreds of volt in amplitude. Moreover V_y tends to rise toward values close to $9\,\mathrm{kV}$ with X >0. These fluctuations and rise are however too small to significantly affect the electron detection in the HPDs.

V_z follows a positive slope ($\approx 35\,\mathrm{kV\,m^{-1}}$) along the Z axis, while it is relatively constant on the X axis. This slope is explained by the fields lines leaking to the vacuum vessel. V_z should have no direct effects on the profile measurement. It will however cause the electrons to slightly shift toward positive Z value.

For all cases presented above, the shape of the integrals is due to the instrument mechanical geometries, while their amplitudes is defined by the cathode voltage. The fine grained fluctuation (spikes) are caused by the honeycomb structure.

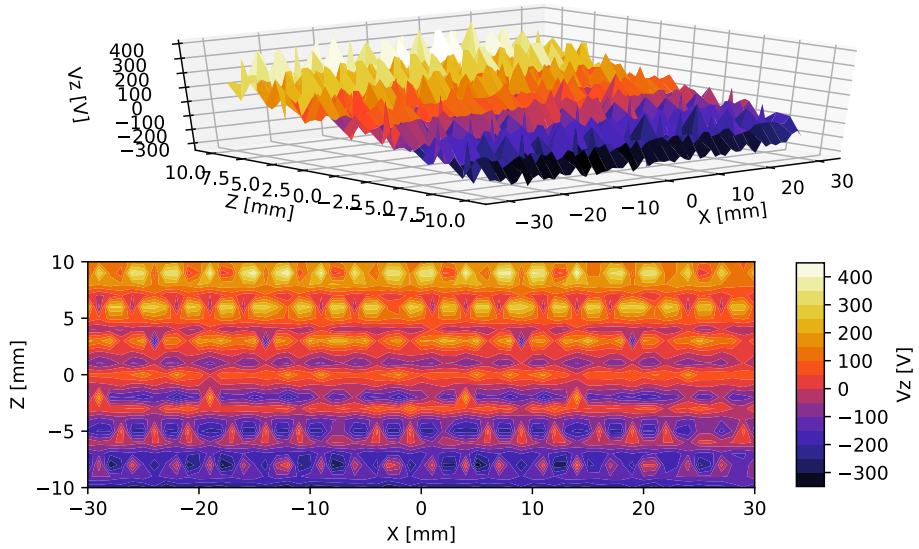

Figure 2.13: E_z integrated along the Y axis. Top: surface plot. Bottom: contour plot.

2.6.2 Effect of the electric field

The quality of the electric field and its effect on the beam profile measurement is first studied by a scan of the cathode voltage, followed by a scan of the beam position relative to the design orbit. In both cases, the magnetic field is not present, and the effect from the ionisation process and beam space charge are not considered.

2.6.2.1 Cathode voltage scan

The beam width error and beam position shift are presented in Figure 2.14. Both are relatively constant with the cathode voltage. The beam width error at injection is slightly lower (4.5 %) than for the extraction beam (5 %). For both beams a 490 µm beam position shift is observed. These results are explained by the electrostatic simulation presented earlier.

2.6.2.2 Position scan

The beam position is scanned across the X axis from −20 to 20 mm. Two cases are studied, the change in the vertical beam position (Y) and the change in the position of the particle generation along Z (since the simulation only creates particles on a 2D XY plane).

The beam position shift is not significantly affected by the position in Z, while the position in Y may increase or decrease it slightly. In both cases the shift follows a quasi

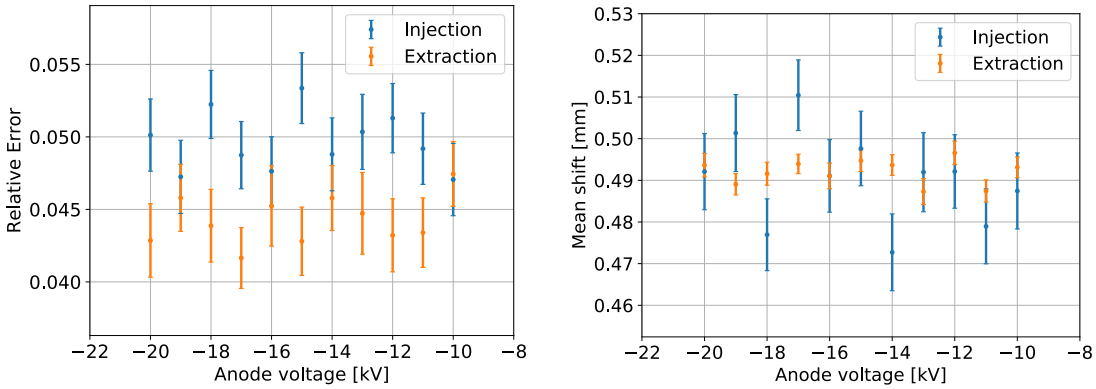

Figure 2.14: Cathode voltage scan. Left: Relative beam width error. Right: Beam position shift. Both include results for the extraction (orange) and injection (blue) BCMS beam.

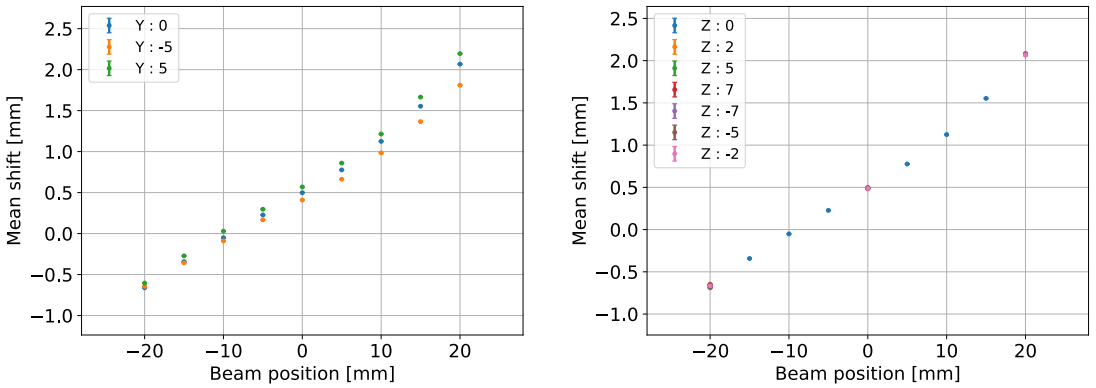

Figure 2.15: Beam position shift for X = [-20:20] mm. Left: Vertical scan Y = [-5:5] mm. Right: Longitudinal scan Z = [-7:7] mm. These are presented for a BCMS beam at extraction. The results at injection results were identical.

slope with a minimum of ≈ -0.65 mm for X $= -20$ mm and maximum of ≈ 2.1 mm at X $= 20$ mm.

The transverse beam position causes a large variation in the beam width error, with a minimum of 5 % at X $= 0$ mm, two maximums 7 % at X $= -20$ mm and 12 % at X $= 20$ mm. This emanates from the fact that V_x (fig 2.11) is not constant across the X axis. The vertical and longitudinal position affect the beam width error by roughly 1 or 2 %. The results are almost identical for the injection and extraction beam, therefore only the results for the extraction beam are presented.

The variations in the beam position shift and beam width error with the vertical beam position are explained by the fact that the electrons have more or less time to drift based on their starting position. The variation caused by the longitudinal position is

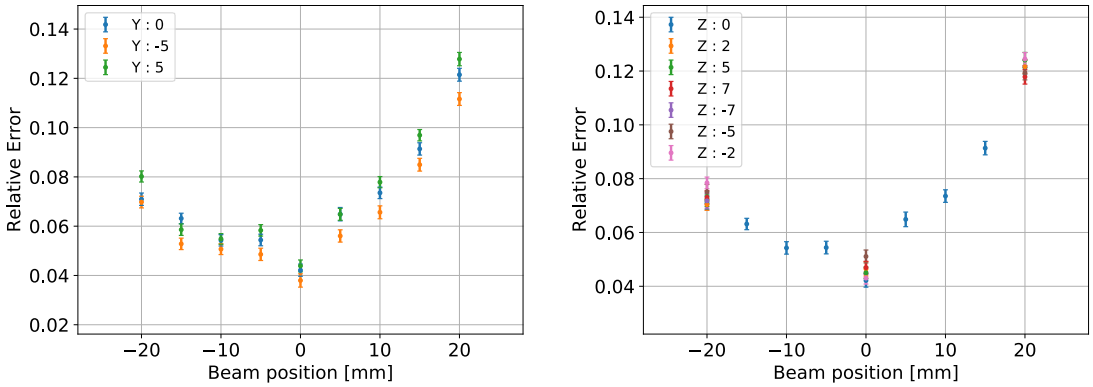

Figure 2.16: Relative beam width error for X = [-20:20] mm. Left: Vertical scan Y = [-5:5] mm. Right: Longitudinal scan Z = [-7:7] mm. These are presented for a BCMS beam at extraction. The results at injection results were identical.

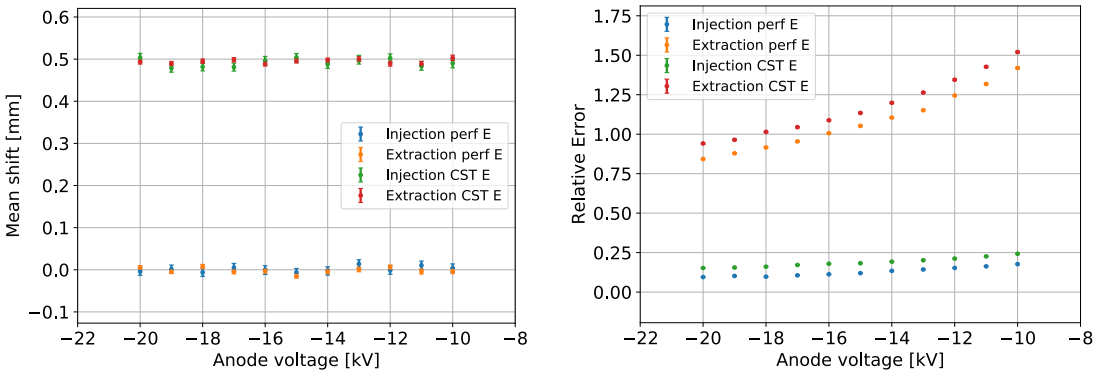

Figure 2.17: Effect of the ionisation process. Left: Relative beam width error. Right: Beam position error. Both include results from simulation with the electric field extracted from CST studio (CST) and from a perfect electric field (perf). The beam used is a BCMS at extraction (orange, green) and injection (blue, red).

probably caused by a small variation in E_x along the Z axis.

2.6.3 Effect of the ionisation process

The effect of the ionisation process on the beam position and width is presented in Figure 2.17. To decouple the perturbations caused by the ionisation process and the electric field, both a perfectly vertical electric field and the field map given by CST-studio are used for the simulations. In all the results presented, none of the profiles passed the goodness of fit test. The beam profile is no longer Gaussian. For this reason, the profile mean and standard deviation are given in place of the fit results.

Figure 2.17 (left) shows that, for the full cathode voltage range, the beam position shift is not affected by the ionisation process. This is valid for both the injection and

extraction beam. The effect of the CST-studio electric field appears to just add to the ionisation process. The absence of a position shift stems from the fact that the ionisation electrons scattering angle is randomly selected from a distribution similar to the one presented in section 2.3.3 (fig 2.4). They are therefore kicked homogeneously transverse to the beam trajectory.

The beam width error (fig 2.17 right) decreases as the cathode voltage increases. The error is ≈ 4 times stronger at extraction than at injection, with values exceeding 75 %. The effect of the CST-studio electric field seems to simply add to the ionisation process.

The variation in the beam width error with the cathode voltage results from the difference in the electrons drift time. The change in electric field affect the electrons drift time, moderating their transverse drift. The difference between the injection and extraction beam stems from the difference in beam width. The kick given to the ionisation electrons is relatively similar in either cases. However, the beams have different sizes, leading to a larger error for the smaller beam.

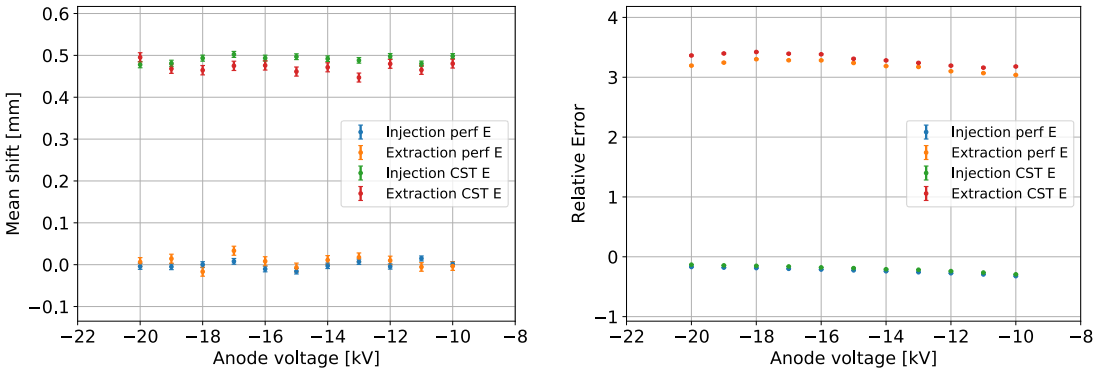

Figure 2.18: Effect of the beam space charge. Left: Relative beam size measurement error. Right: Beam position error. Both include results from simulation with the electric field extracted from CST studio (CST) and from a perfect electric field (perf). The beam used is a BCMS at extraction (orange, green) and injection (blue, red).

2.6.4 Effect of the beam space charge

The effect of the beam space charge is presented in Figure 2.18. To decouple the perturbations caused by the beam space charge and the electric field, both a perfectly vertical electric field and the field map given by CST-studio were used for the simulations. Like for the ionisation process results, all of the profiles failed the goodness of fit test. The profile

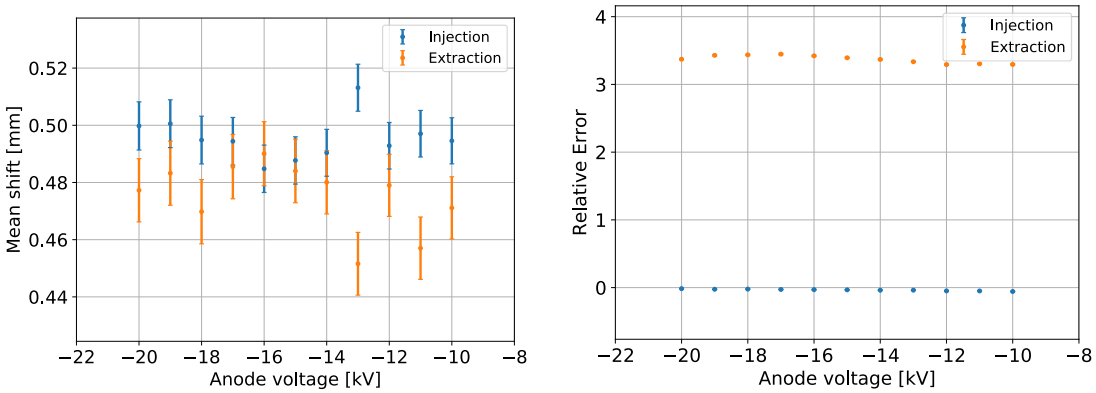

Figure 2.19: Combined effects of the electric field, ionisation process and beam space charge. Left: Relative beam width error. Right: Beam position error. Both include results for the extraction (orange) and injection (blue) BCMS beam.

mean and standard deviation are given in place of the fit results.

The beam position shift is mostly unaffected by the beam space charge. When the effect from the CST-studio electric field is added, the mean shift moves to 500 µm. At injection, the beam size error is negative with values between −40 and −20 %. The error tends to reduce linearly with the increase in the cathode voltage. At extraction, the error is positive with values above 300 %. The error varies non-linearly with the cathode voltage. The effect of the CST-studio electric field seems to add an extra 5 % of error to the effect of the space charge.

In the case of the injection beam, the large beam size and relatively weak beam space charge, attract the electrons toward the beam centre. This causes the profile to shrink. In the case of the extraction beam, the stronger beam space charge pulls the electrons past the beam centre, causing the beam width to grow. The absence of beam position shift is explained by the symmetric pull the beam space charge applies on the ionisation electrons.

2.6.5 Combined effects

The electric field inhomogeneity, ionisation and space charge effect are all included in the simulation. The results of the combined perturbations is presented in Figure 2.19. Due to the large distortion caused to the beam profiles, all of them failed the goodness of fit test. The profiles mean and standard deviation are given in place of the fit results.

The beam position shift, both for injection and extraction, is centred around 500 µm. Moreover there is no clear effect from the change in cathode voltage. At extraction, the beam width error is mostly above 300 % with a non-linear response to the change in

cathode voltage. At injection, the error decreases from 10 % to 3 % as the cathode voltage increases. These values are lower than for the effect of the space charge only.

These results indicate that the beam space charge is the dominating source of beam width error, while the electric field causes the beam position shift. At injection, when the beam space charge is weaker, the beam width error is almost compensated by the ionisation process effects.

2.6.6 Effect of the magnetic field

To compensate for the effects detailed in the previous section, a 0.2 T magnetic field is introduced in the simulation. First a scan of the cathode voltage is performed, then a scan of the magnetic field from 0 T to 0.2 T is done.

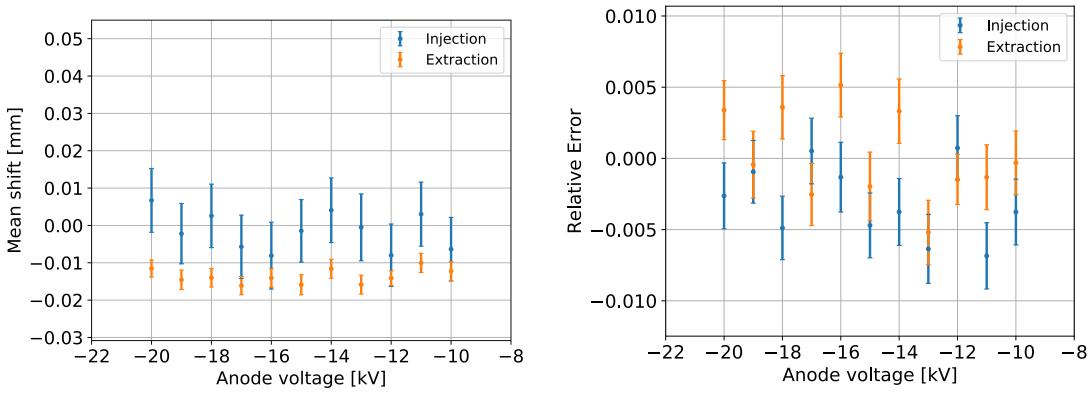

Figure 2.20: Corrective effect of the magnetic field Left: Relative beam width error. Right: Beam position error. Both include results for the extraction (orange) and injection (blue) BCMS beam.

2.6.6.1 Cathode voltage scan

The results of the cathode voltage scan are presented in Figure 2.20. For both the injection and extraction cases, the beam position shift is mostly between −20 and 20 µm. While the beam width is below 1 %, there is no clear effect from the change in cathode voltage. All profiles presented here pass the goodness of fit test.

2.6.6.2 Magnetic field scan

The result of the magnetic field scan are presented in Figure 2.21. For the injection case, both the beam position shift and width error remain withing acceptable values down to 0.03 T. From there, the position shift moves toward 500 μm and the width error climbs

to ≈ 8 %. All profiles expect the one with no magnetic field pass the goodness of fit test. The profile mean and standard deviation are therefore used for this point.

For the extraction case, the beam position shift immediately increases as the magnetic field decreases. It ultimately stops at 500 µm. The beam width error remains below 1 % down to 0.11 T, it then increases to reach 300 %. The profiles where the magnetic field is above or equal to 0.11 T all pass the goodness of fit test. The mean and standard deviation are used for the value where the magnetic field is below 0.11 T. To highlight the effect of the magnetic field on the measured profile, a comparison between profiles measured with a magnetic field of 0 T and 0.2 T is given in Figure 2.22.

These results show that a magnetic field strength of 0.2 T is largely sufficient to prevent profile distortions.

2.6.7 Consequence from a misaligned magnet

The angle between the magnetic field and guiding electric field (θ) is increased from 0° to 10°. Both a rotation in the X-Y and Z-Y planes are considered, the X-Z plane is ignored since it does not affect the vertical magnetic field component B_y. The magnetic field is set to 0.2 T and the −20 kV CST-studio electric field is used. The results are presented in Figure 2.23.

In the case of a rotation in the X-Y plane, the beam position shift increases linearly from 0 to −8 mm; while the beam width error remains below 1 % until $\theta \approx 5°$, it then continues to increase to reach ≈ 2.5 %. A rotation in the Z-Y plane causes a small beam position shift (0 mm to 0.25 mm) and the beam width error remains below 1 % for the full rotation range. For both planes, there is no significant difference between the injection and extraction cases.

In conclusion, the effect of a small rotation between the magnet and the instrument do not cause significant profile distortions. However the mean shift is problematic as it significantly reduces the aperture of the detector.

2.6.8 Corner Case

To conclude the simulations, a corner case is studied, the BCMS beam at extraction with the HL-LHC parameters (×2 intensity). Two scenario are considered, first the beam is at the design orbit and second, it is shifted by 20 mm in X. The latter corresponds to an absolute worst case and is based on the position scan result of section 2.6.2. The magnetic

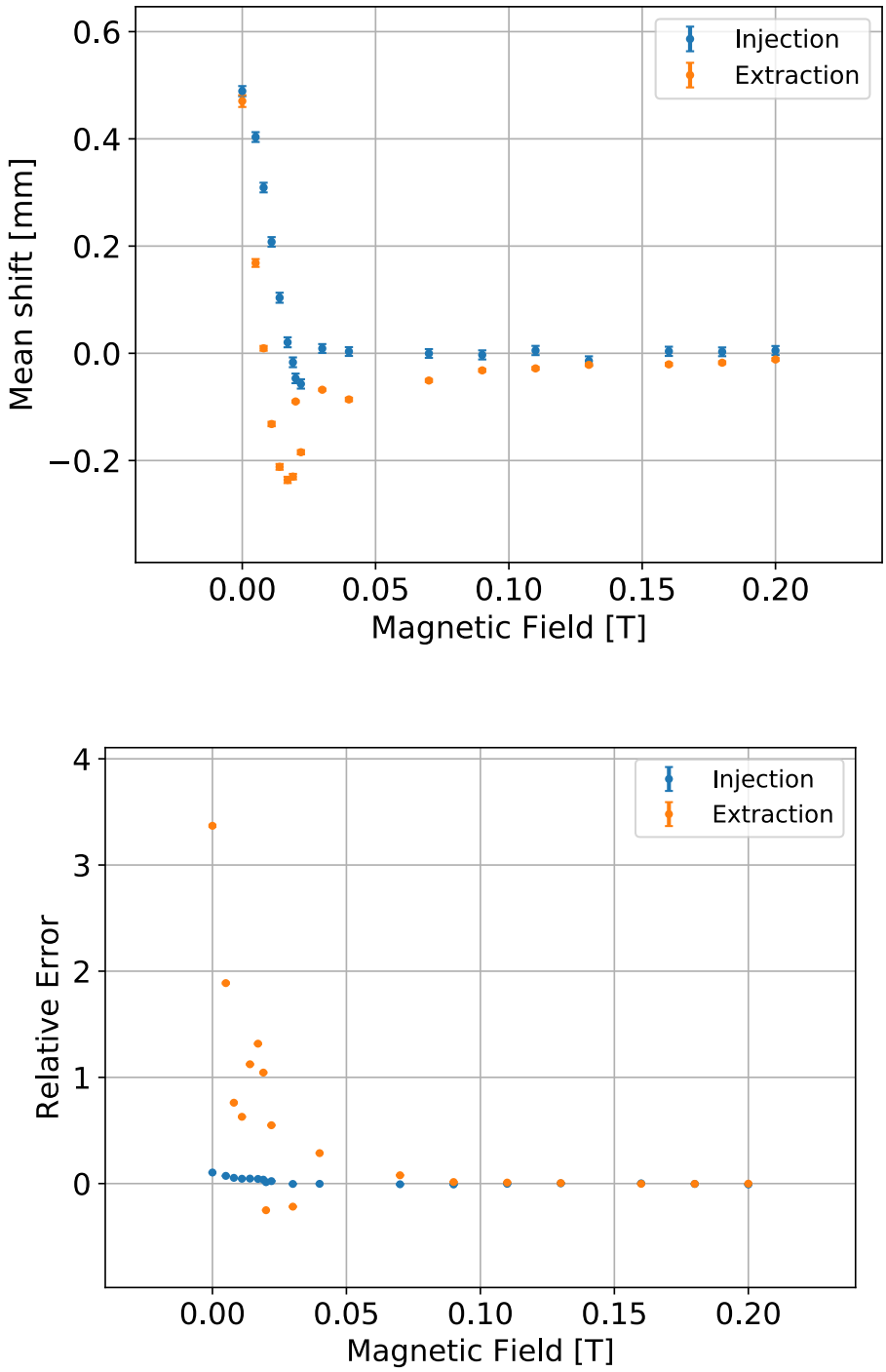

Figure 2.21: Magnetic field scan from 0 to 0.2 T. Left: relative beam width error. Right: Beam position error. Results for the extraction (orange) and injection (blue) BCMS beam are presented

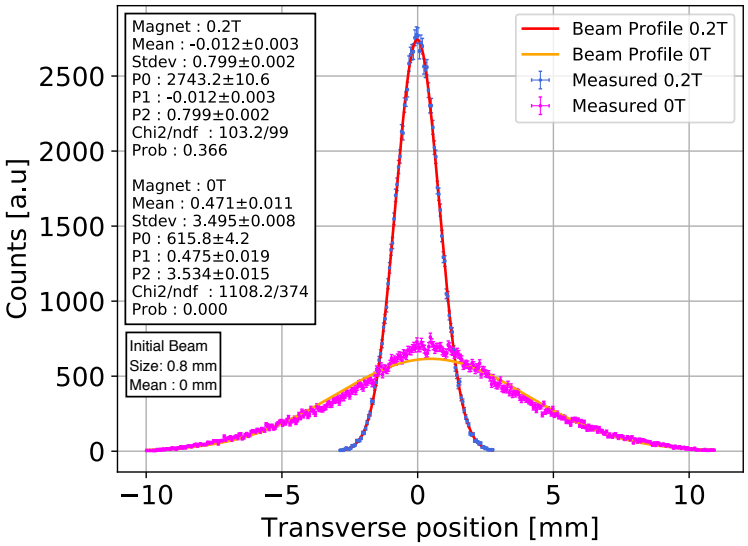

Figure 2.22: Simulated beam profile measurement of a BCMS beam at extraction with and without magnetic field. The measurement with the magnetic field is not distorted and provide the correct beam width (800 µm); while the measurement without magnetic field is no longer representative of the beam profile.

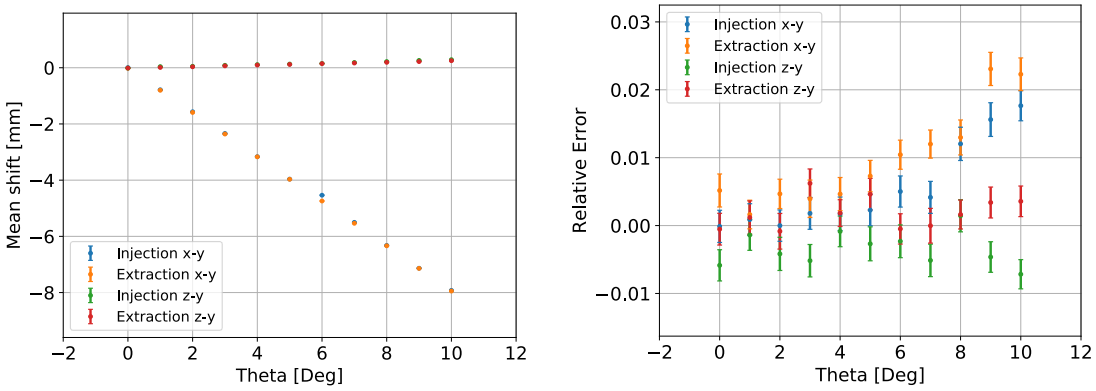

Figure 2.23: Magnetic field misalignment scan from 0° to 10°. Left: Beam position error. Right: Relative error on the beam width. Results for the X-Y plane (blue, orange) and Z-Y plane (green, red) are presented for a BCMS beam.

field is set to 0.2 T and the −20 kV CST-studio electric field is used.

The results are presented in Figure 2.24. In both scenarios, the beam width error is below 0.25 % and the position shift is in the order of a few micro-metres. This result shows that the magnetic field is successful at preserving the beam profile in what is the worst possible scenario.

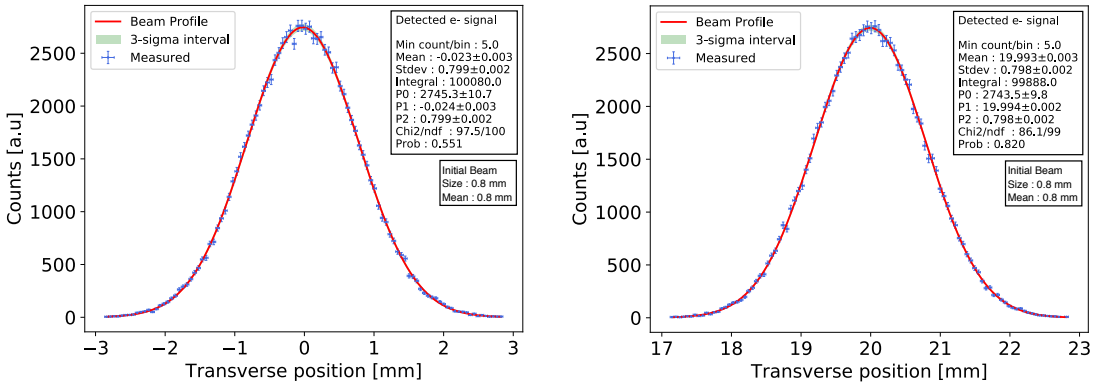

Figure 2.24: Profiles from a HL-LHC BCMS beam centred (left) and transversely shifted by 20 mm (right).

2.7 Summary

The CERN Proton Synchrotron and relevant LHC beams were introduced. The instrument will principally be used to measure the nominal-LHC and BCMS beams. These are challenging to measure due to their small width and high intensity.

A concept for the instrument design which matches the performance requirements was presented. It relies on the use of the ionisation electrons for the profile measurement. These are guided and constrained by a vertical $-286\,\mathrm{kV\,m^{-1}}$ electric field and 0.2 T magnetic field.

The conceptual design was tested with simulations. These showed that:

- The instrument should perform as required, even in worst case scenarios, given that a sufficiently strong and well aligned magnetic field is applied.
- A magnetic field of 0.1 T is enough to keep the error on the beam width measurement below 1 % with the current LHC beams.
- The absence of field shaping side-electrodes and new ion-trap design should not affect the performance of the instrument.

Chapter 3

Implementation

In the previous chapter, the instrument concept was introduced and validated. In this chapter, the implementation of this concept into a proper design is presented in Section 3.2. The main challenge of this implementation is to comply with the PS environment, which is introduced in Section 3.1. The instrument detector is based on the Timepix3 hybrid pixel detector. The motivations for this choice and its working principle are given in Section 3.3. In order to operate, the Timepix3 requires a state of the art read-out system, which is introduced in Section 3.4.

3.1 Environmental constraints

The instrument is allocated to the Straight Section 82 (SS82), presented in Figure 3.1. Among the available locations, it was the least radioactive one. The section is 1 m long with no hard restriction on the width or height. The BGI shall be compatible with the PS

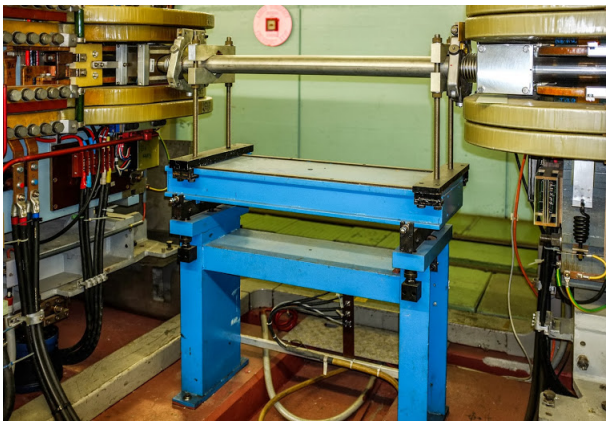

Figure 3.1: The Straight Section 82 before the PS-BGI installation.

Ultra High Vacuum ($<10^{-9}$ mbar). A gas injection system is highly undesirable due to the presence of ion beams in the PS, for which the ionisation cross-sections are four orders of magnitude higher than for protons, leading to poor beam lifetime and stability. Molecular hydrogen (H_2) is assumed to dominate the residual gas composition in the instrument [64], with a pressure range of 10^{-9} to 10^{-10} mbar.

Since the PS vacuum system is not baked, a large amount of water (H_2O) is also expected. At this location the device will be exposed to a radiation dose estimated to be between 1 to 10 kGy per year. This radiation might create background signals in the instrument detector (see Chapter 6). Due to the restricted access to the PS during the physics run, the device is only accessible for maintenance once every few months. Moreover, vacuum interventions are only possible once a year, during the winter shutdown. For these reasons the internal components of the BGI have to operate fault free for a minimum duration of one year.

3.2 System design

The conceptual design was implemented as a mechanical design by the CERN mechanical design office under the supervision of the PS-BGI project team, the author included. For clarity, the BGI mechanical design is divided in two parts, the atmospheric part and vacuum part. It is important to note that the PS-BGI design was realised under tight time constraints, especially the detector and cooling system. This made the prototype design focus on vacuum compatibility and radiation hardness.

3.2.1 Atmospheric part

The instrument vacuum chamber is presented in Figure 3.2, where five flanges are visible. At the extremities, the connection to the PS is ensured with two conical flanges. The BGI is bolted to a rectangular ConFlat (CF) flange and inserted in the rectangular compartment in the centre. A spare DN40CF is unused and a DN63CF flange is used to connect to a small ion pump ($50\,l\,s^{-1}$).

The instrument flange comprises two SHV20 high voltage feedthroughs to supply the -20 kV to the cathode, a pair of sub-D78 feedthroughs for the digital communication with the detector and one sub-D26 to power it. In addition, a cooling water inlet and outlet pipe are present to connect to the PS chilled water cooling circuit. A pair of removable

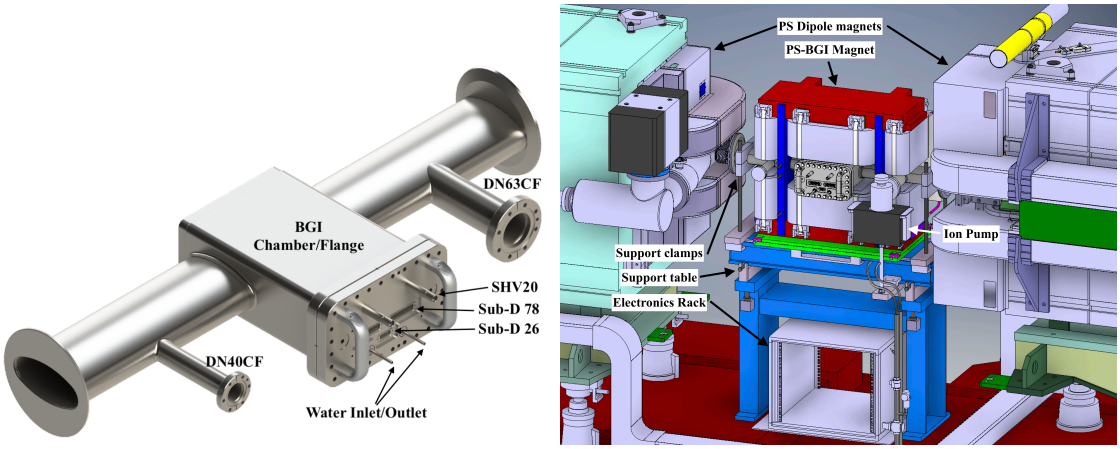

Figure 3.2: Left: Rendered image of the PS-BGI vacuum tank and instrument flange. Right: Integration of the PS-BGI at SS82.

handles is present to help during transport, installation and maintenance. In order to meet CERN Ultra-High Vacuum (UHV) standards and to not perturb the instrument magnetic field, the vacuum chamber is entirely made of 316LN stainless steel.

The chamber is supported by a pair of clamps affixed to its extremities. These allow for the precise alignment of the BGI and are attached to a standard support table bolted to the floor. The magnet is supported from the table, making it independent from the vacuum chamber. Its electrical and water cooling connections are made on the exterior of the PS ring, while all the BGI connections are on the inside of the ring. A small rack under the support table is used to host multiple electrical/optical patch panels and part of the readout electronics.

3.2.2 Vacuum part

The in-vacuum part of the instrument is visible in Figure 3.3. A pair of support arms, bolted to the flange, is used to support the cathode, anode, Faraday cage and detector sub-assembly. A thin rigid copper wire connects one high voltage feedthrough to the cathode. The cathode is isolated from the rest of the instrument by a set of ceramic spacers.

The Faraday cage protects the detector from the beam radio-frequency interference and provides a low resistance passage for the beam mirror current. It is composed of the anode, steel honeycomb and the copper top/side covers. A set of spring loaded steel balls (not visible in the Figures) electrically connects the support arms to the vacuum chamber.

The instrument is entirely made of 316LN steel, with the exception of the Faraday cage cover and side plates, which are made of oxygen-free copper. All fasteners in contact

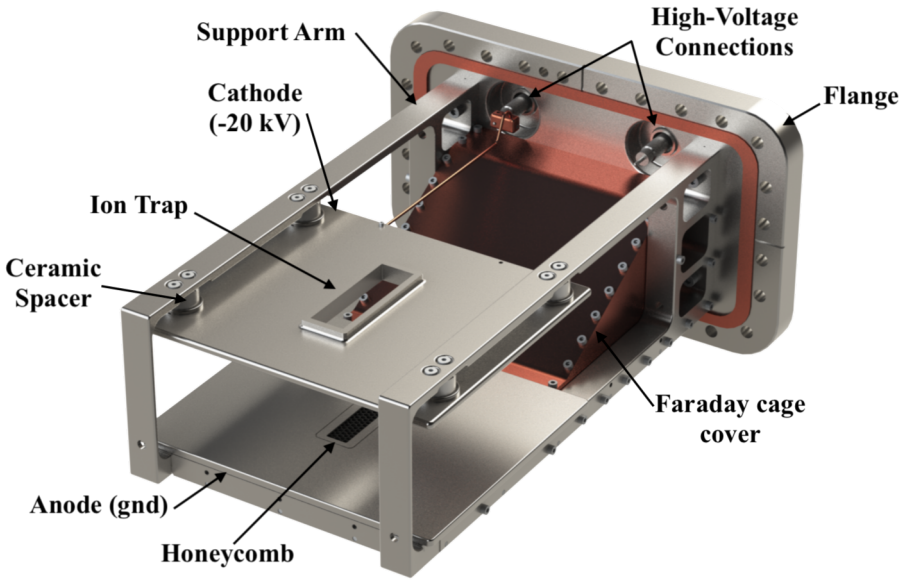

Figure 3.3: Rendered image of the PS-BGI vacuum parts.

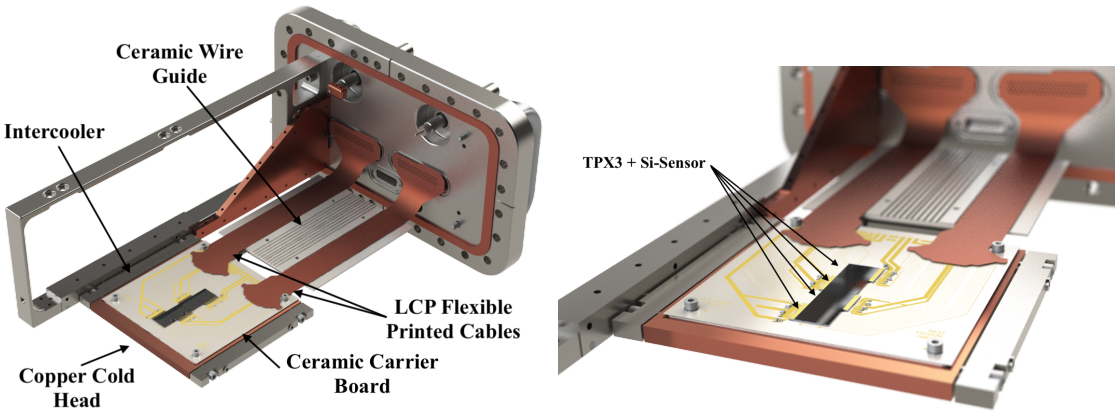

Figure 3.4: Left: Rendered image of the detector sub-assembly. Right: close-up view of the ceramic carrier board.

with steel parts are silver coated to reduce the chance of cold weld. In addition most of them are vented to prevent the creation of virtual leaks during installation.

3.2.3 Detector sub-assembly

The detector sub-assembly, comprising the detector and the cooling system, sits under the anode and Faraday cage, as in Figure 3.4. The detector is composed of four individual Timepix3 Hybrid Pixel Detectors (HPDs) placed side by side in a line perpendicular to the beam direction. This configuration allows the detection surface to completely cover the range of motion of the PS beams. The HPDs are secured on the so-called ceramic chip carrier board. The chip carrier is a two layer ceramic (Al_2O_3) Printed Circuit Board

(PCB), which hosts the Timepix3 chips and connects the signals to a pair of Liquid Crystal Polymer (LCP) Flexible Printed Cables (FPCs). The chip carrier connects to the flexible cables via a set of low profile connectors. The flexible printed cables then directly connect to the sub-D 78 vacuum feedthroughs. Each cable supports the signals of two Timepix3 chips.

The power for the Timepix3 is brought to the chip carrier by a set of bare copper wires (not visible in the Figures). These are soldered to the PCB and individually mated with the sub-D26 feedthrough. In order to prevent short circuits a ceramic-guide constraints these wires, while at the same time preventing the flexible cables from touching the Faraday cage cover.

This architecture is driven by the need to produce a design with low outgassing to pass the vacuum acceptance test set by the CERN vacuum group. The low outgassing constraint means that the design has to be simple, with as few parts as possible. Moreover, the use of polymers has to be limited to a bare minimum and the materials/fabrication technique have to be chosen accordingly. The detailed design, production and testing for the detector electronics are presented in Chapter 4.

3.2.4 Cooling system

Each Timepix3 produces from 1 W to 3 W of heat when operated. Due to the lack of natural convection, the detector is cooled using a liquid cooling circuit. Chilled 6 °C demineralised water from the PS water circuit is circulated in a thin steel pipe brazed to a copper cold-head. The cold-head is attached to the support arms via a pair of steel intercoolers designed to minimise heat transfer.

The detector is attached to the cold head by a four fastener placed in the corners of the ceramic carrier board. A ceramic spacer is placed in between the carrier board and the cold-head to electrically isolate them. This spacer is itself brazed to a copper bar, which is in turn fastened to the cold-head.

In order to ensure proper thermal conductivity from the ceramic carrier to the ceramic spacer, a 100 µm gold foil is inserted in between the two to act as a thermal interface. Gold is selected for its ductility and high thermal conductivity. Graphite and indium were also considered but were ultimately rejected due to their incompatibility with the vacuum requirements. This assembly of the detector to the cold-head is referred to as the cooling stack and is depicted in Figure 3.5.

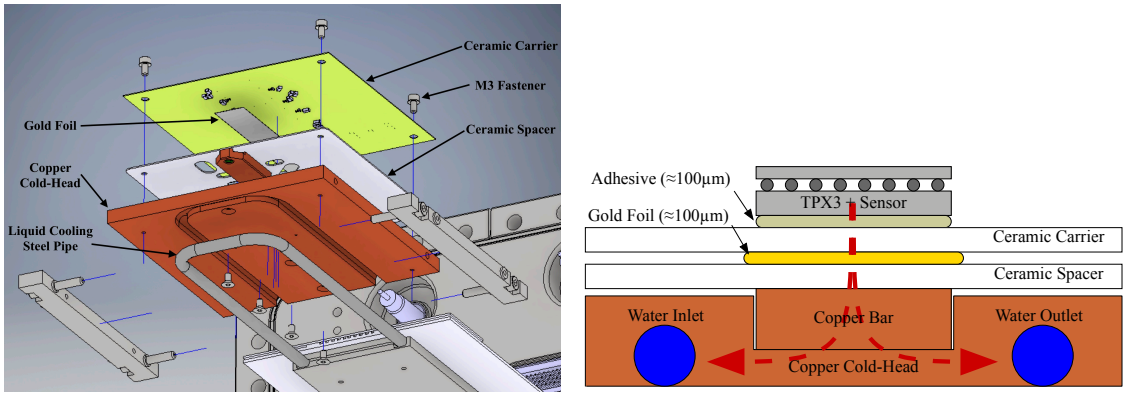

Figure 3.5: The cooling stack thermally connect the HPDs to the chilled liquid. Left: Exploded view (Ceramic carrier in false colours). Right: Schematic view.

To monitor the detector temperature, the Timepix3s internal temperature sensors are used (see Section 3.4.1). These are however neither precise nor calibrated, providing only a rough estimate of the system temperature. The addition of PT100 temperature sensors was considered to make the temperature monitoring more precise, robust and reliable. However, this addition complicated the design and was ultimately abandoned.

This cooling solution was simulated with a simplified model in Ref [65] but it could not be tested prior to the BGI production due to time constraints. The overall cooling performance was estimated to be sufficient to operate the detector.

3.3 Detector choice

The PS-BGI detector is based on the Timepix3 hybrid pixel detector. The Timepix3 was selected for it low noise floor, high sustained detection rate and high temporal resolution. Allowing the BGI detector to reach the required profile measurement rate. Other important criterion were its high radiation hardness, small form factor, high spacial resolution, insensitivity to static magnetic field and the fact that CERN is responsible for its design and production.

3.3.1 Hybrid pixel detector

Hybrid pixel detectors are devices meant to detect and measure ionising radiation. They combine a pixelated sensor and readout chip, which are soldered together. The sensor is a matrix of p-n diodes - called pixels - reverse-biased to allow electrons or holes to be collected by the readout chip. It is usually covered with a thin aluminium layer to prevent

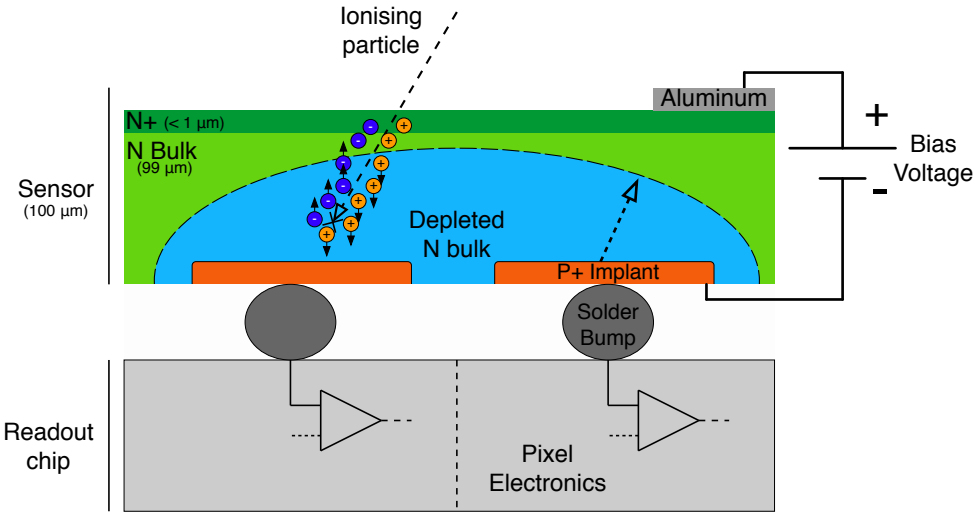

Figure 3.6: Illustration of a hybrid pixel detector. An inbound ionising particle is stopped by the P-on-N sensor, creating electron hole pairs. A bias voltage is applied to create a depletion zone within the sensor N-bulk. To show the difference between depleted and non-depleted zone, the depletion zone is intentionally depicted smaller than it is in a fully depleted sensor, where it would extend all the way to the N+ layer. The holes present in the depletion zone are collected by the readout chip, the rest are lost to the thin, almost conductive, N+ layer.

light from reaching the silicon, which would otherwise create a noise source in the sensor. The readout chip comprises a matrix of readout channels that matches the size and pitch of the sensor. Each readout channel amplifies and then digitises the charge from each sensor pixel.

The working principle of HPDs is illustrated in Figure 3.6. An incident ionising radiation is stopped by the sensor, creating electron hole pairs. These are then separated by a biasing electric field and depending on the sensor type, either electrons or holes are collected by the readout chip. If the charge collected by a pixel reaches a certain predefined threshold, the pixel records information such as the energy, location and time of this event. The data from each event is then temporarily stored and read-out off the chip by a dedicated readout system. The term *event* relates to the interaction between an ionising radiation and the sensor, and the information that is subsequently recorded/transmitted by the readout chip.

3.3.2 The Medipix Timepix3 readout chip

The Timepix3 is a pixelated readout chip, designed by the Medipix collaboration [66]. It is a faster and more capable evolution of the Timepix chip [67]. The Timepix3 is visible

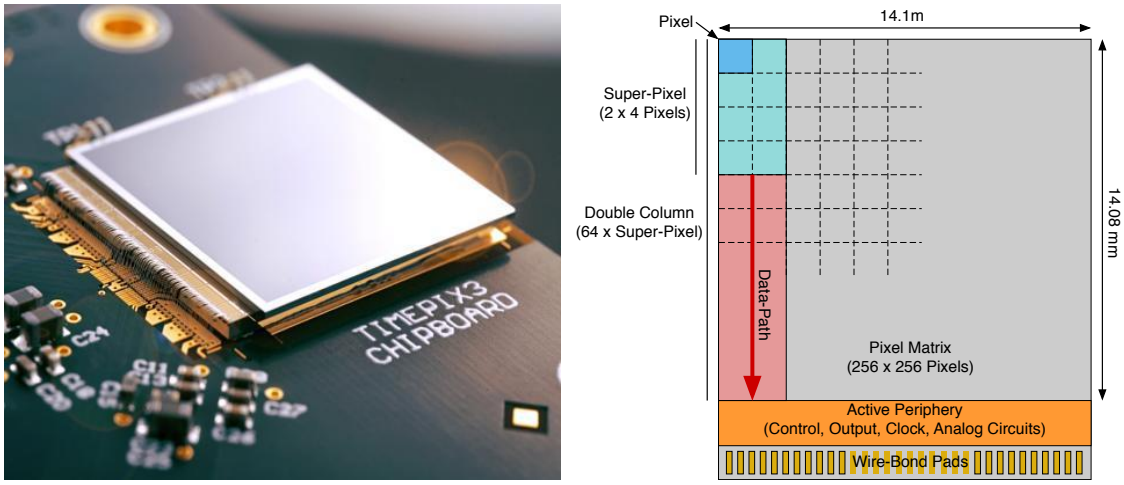

Figure 3.7: Left: Picture of a Timepix3 and silicon sensor mounted on a Medipix chip-board. The Timepix3, connected via a multitude of wire-bonds, sits under the sensor. The sensor is non-metalised, only a frame of aluminium is kept to connect the bias voltage. Right: Schematic layout of the Timepix3. Each pixel is read-out by a 2-by-4 super-pixel, which is itself read-out by a double-column.

in Figure 3.7. The chip's physical layout is composed of the pixel matrix, active periphery and wire-bond pads. The pixel matrix is populated with an array of 256 by 256 pixels, each 55 µm by 55 µm, for a total detection area of 14 mm by 14 mm. Each pixel can individually record the so called Time of Arrival (ToA) and Time over Threshold (ToT) of an event. These are presented in Figure 3.8. Moreover, the pixel position is intrinsically known in terms of row and column coordinates. The ToA is a time-stamp corresponding to the moment the charge collected by the pixel exceed the input threshold. Its clock runs at 40 MHz, resulting in a basic resolution of 25 ns. In addition, a fast ToA (fToA) running off a 640 MHz clock can be used, improving the resolution further to 1.56 ns. The ToT is the time it takes for the charge stored in the pixel to decay below the threshold. If properly calibrated [68], it can yield the amount of charges collected in the pixel, which is directly related to the incident particle energy if it stops in the sensor. The minimum usable threshold is $\approx$ 500 electrons [47].

The active periphery allows the user to control the chip. With actions such as enabling the digital shutter signal or setting the pixels matrix thresholds. The chip, when operated at 40 MHz, can detect and process up to 40 MEvent/s. Events can be read-out with two main schemes; data-driven or frame based. In data-driven, events are read-out from the chips as they come, while in frame based, events are read-out only after the shutter is closed. Both schemes are zero-suppressed, meaning that only pixels with events

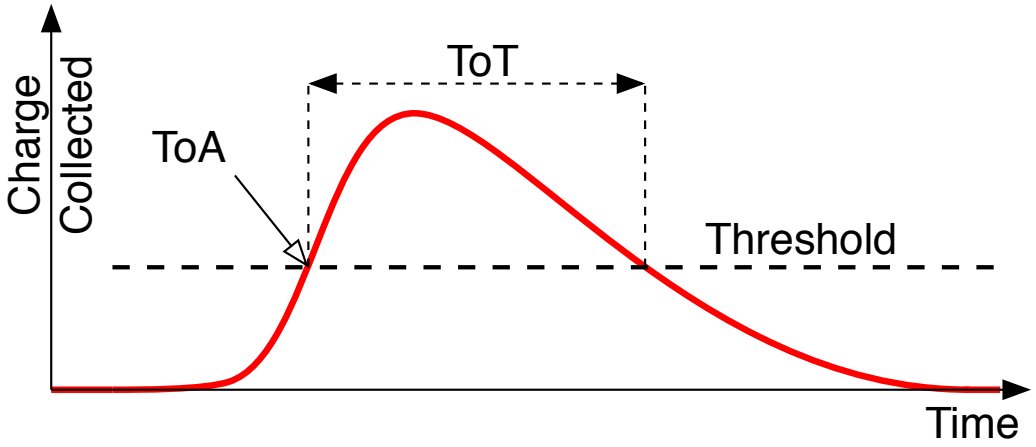

Figure 3.8: Example of an event's charge collected in a Timepix3 pixel. The Time of Arrival and Time over Threshold are presented.

are read-out. The transmission of events off-chip is achieved by a set of eight Scalable Low Voltage Signalling (SLVS) links. These can be used at speeds ranging from 80 to 640 Mbit s^{-1} for a total maximum throughput of 5.12 Gbit s^{-1}.

One edge of the Timepix3 is used to connect the power, control and output signals to a PCB using wire-bonds. The three remaining edges may be used to tile Timepix3 chips together, increasing the detection surface.

3.3.3 Sensor choice

The Timepix3 can be paired with crystalline, MCP or gas-filled sensors. The sensors selected for the PS-BGI detector are 100 µm thick, edge-less and made of silicon with either a P+ implant in a N bulk (P-on-N) or N+ implant in a P bulk (N-on-P) pixel structure (see Figure 3.9). The P-on-N sensors are completely non-metallised, while the N-on-P sensors have a small aluminum band covering their first and last two rows. These bands are used to connect the bias wire to the sensor surface. The surface (<1 µm) of the sensor is N+ doped by default. This layer has a much lower resistivity than the bulk and allows the bias voltage to spread more uniformly.

Silicon is chosen for its availability and its relatively low average ionisation energy of 3.6 eV, making it suitable for the detection of low energy electrons. An electron with 10 keV of kinetic energy would on average creates 2780 electron hole pairs in the sensor, which is largely above the 500 electrons limit of the Timepix3. However, this number is rather idealistic as a fraction of these pairs will be lost in the N+ layer and to other effects

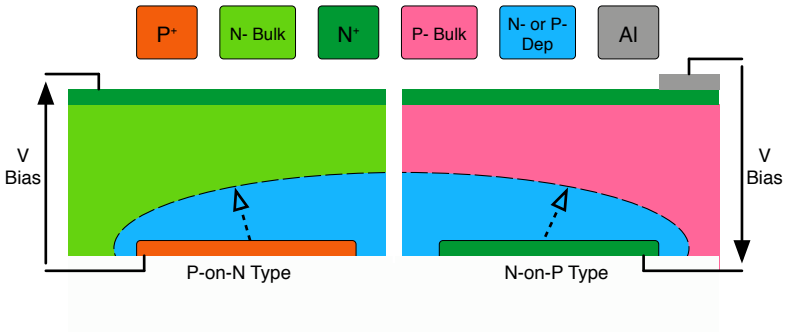

Figure 3.9: Illustration of the two types of sensor used in the PS-BGI detector. On the left half, a P-on-N sensor is presented, while the right half presents a N-on-P type. The blue region is the depletion region extending from the implant to the surface.

(recombination, trapping).

The average ionisation-electrons penetration depth in a silicon sensor (R_{si}) can be estimated using the Continuous Slowing Down Approximation (CSDA) range

$$R_{si} = \frac{CSDA_{range}}{\rho_{si}} \tag{3.1}$$

with ρ_{si} the density of silicon ($2.329\,\mathrm{g\,cm^{-3}}$). The NIST ESTAR [69] database gives the CSDA range for 10 keV electron in silicon at $3.461 \times 10^{-4}\,\mathrm{g\,cm^{-2}}$, which makes the penetration depth $\approx 1.5\,\mu\mathrm{m}$. The sensor thickness of 100 µm was chosen over the more standard 300 µm to reduce the drift distance of the deposited charge, thus reducing the drift-time and limiting the amount of charges trapped in the sensor. In comparison, the electron penetration depth in aluminium is $\approx 1.31\,\mu\mathrm{m}$. The sensor surface metallisation would therefore prevent ionisation electrons from reaching the silicon, hence the aforementioned use on non-metallised sensors only.

P-on-N sensors were initially selected for the project as they are standard and were successfully tested for the detection of low energy electrons (<5 keV) with a Timepix and the calibration system of a retired SPS BGI [50]. These sensor equipped the first prototypes of the detector, named MKI.

However, P-on-N sensors undergo type inversion when exposed to a significant fluence of ionising radiation ($\approx 1 \times 10^{13}$ proton/cm^2) [70,71]. This process converts the sensor N-type bulk into a P-type bulk. This causes the depletion voltage to decrease until it becomes null, to then increase linearly with the fluence. The transient period where the depletion voltage is null prevents the sensor from collecting charges and therefore prevents it from being used. This is problematic as the PS-BGI would become unusable for a period

of time dependent on the beam loss at its location. The fluence at the PS straight section 82 is currently unknown but it is certainly below the one observed at the PS straight section 3; which is in the order of 1×10^{13} proton/cm^2/year

To mitigate the possibility of type-inversion, a small batch of N-on-P sensors were procured. As opposed to P-on-N sensors, the depletion voltage of N-on-P sensors only increases linearly with fluence. This prevents the sensors to become ineffective when irradiated and therefore increases its effective lifetime. For this reason, another detector prototype — named MKII — was equipped with N-on-P sensors.

3.4 Control and readout system architecture

The control and readout system is a suite of hardware and software components responsible for the communication with the detector. Its main role is to allow a user to control the detector and to receive/manage the very large amount of data transmitted by the detector during an acquisition.

Although SPIDR [72], a commercial readout system for the Timepix3 exists, it could not offer the specific functionality required to operate the PS-BGI detector and is not compatible with operation in a radiation environment. For this reason a new readout system was designed and implemented by the PS-BGI team. This new readout would need to handle the large data rate created by the detector ($4 \times 5.12\,\mathrm{Gbit\,s^{-1}}$) and have the possibility to be integrated in the CERN infrastructure. As an added challenge, the Timepix3 SLVS links can only transmit data for a short distance (<2 m) forcing part of the readout system to be located in the PS radioactive environment.

The architecture devised for the readout is presented in Figure 3.10. The detector is controlled by a specialised software running on the Data Acquisition (DAQ) computer. The DAQ computer communicates via an Ethernet link to the back-end, which handle the data to/from the front-end as well as maintains the detector synchronisation with the PS timing. An $\approx 150\,\mathrm{m}$ optical fibre link connects the back-end and front-end. The front-end, a radiation tolerant electronic board located just under the PS-BGI, acts as a bridge between the short range SLVS link of the Timepix3s and the long range optical fiber link. During data acquisition periods, the data streaming from the detector are buffered in the back-end before being sent to the DAQ computer for long term storage. The back-end and DAQ computer are located in a counting room that is accessible anytime, while the

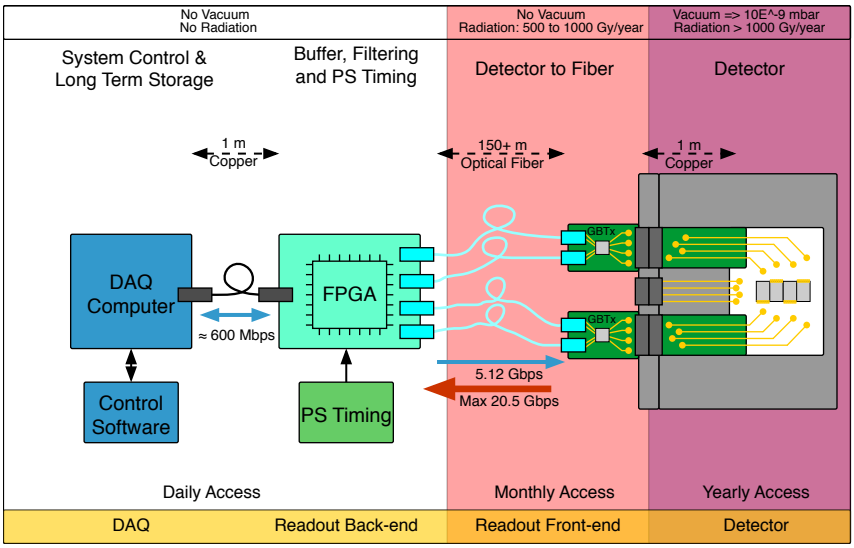

Figure 3.10: PS-BGI readout architecture diagram.

front-end is only accessible once every few months during PS maintenance periods.

The development of the control and readout system was initially the responsibility of the author, it was however transferred to H.Sandberg whom did the vast majority of the work presented in this section. Details regarding his work are available here [73]. The author contributed to the readout system by designing the interconnection between the flange and the readout (PCB design and cable selection), and the *off-line* mode of the DAQ software (see Section 3.4.3).

3.4.1 Front-end

The front-end is implemented on the GBT-based Expendable Front-End (GEFE) board [74]. It is a versatile, radiation-tolerant, Field Programmable Gate Array (FPGA) board developed by the BE-BI group at CERN. The GEFE provides a bi-directional 4.8 Gbps optical link based on the GBTx [75] and VTRx [76], a Microsemi ProAsic3 FPGA [77] and FPGA Mezzanine Card (FMC) connector. The GBTx and VTRx are radiation tolerant components developed to implement high speed optical links for CERN LHC experiments. The GEFE is tested for a Total Ionisation Dose (TID) of 750 Gy, which corresponds to the point were the FPGA fails. The detector connects to the GEFE via a set of interface boards and Ethernet cables, linking the sub-D78 vacuum flange feedthrough and the GEFE FMC. In addition, an Arduino board [78] provides a simple Analog to Digital Converter (ADC) to monitor the Timepix3 internal temperature sensors.

The GEFE FPGA runs a custom firmware, named *Water-Bear*. This firmware im-

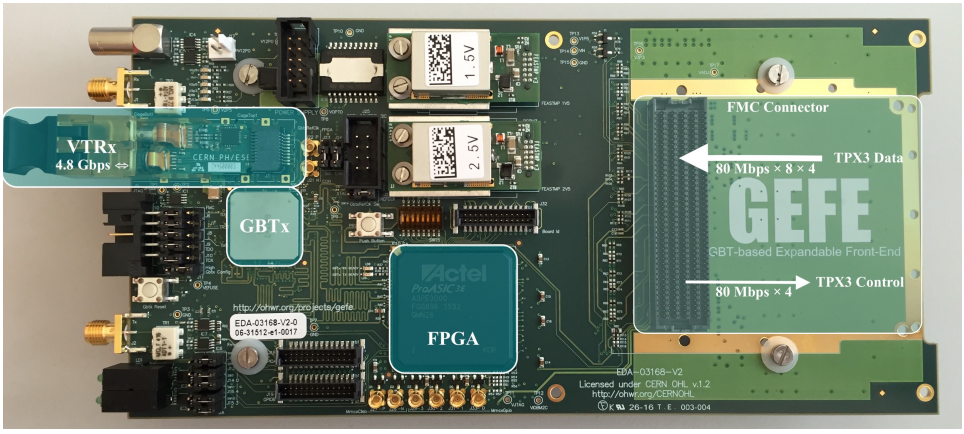

Figure 3.11: BE-BI GEFE FPGA front-end board.

plements the interface to communicate with the four Timepix3 chips and the interface to send/receive data to/from the GBTx. Timepix3 data is packed into BGT frames for transmission with the GBTx or GBTx frames unpacked for transmission to the Timepix3. The firmware also provides a reference clock to all four Timepix3 chips and ensures that they receive control signals synchronously.

This implementation of the front-end is limited by the FPGA Inputs/Outputs (IOs) performance. The speed at which the FPGA can receive data from a Timepix3 SLVS link is capped at 80 Mbps. As a consequence, the event rate sustainable by the detector drops by a factor eight, from 4×80 MEvent/s to 4×10 MEvent/s. This reduces the expected data rate from 20.5 Gbps to 2.5 Gbps, allowing all the detector data to be handled by a single GEFE board.

This front-end solution was adopted despite its technical limitation due to the immediate availability of the GEFE, drastically reducing the time required to have a functional readout system and instrument. A new front-end designed to sustain the maximum event rate (4×80 MEvent/s) will be implemented during CERN long shutdown 2 (2019-2020).

3.4.2 Back-end

The back-end is implemented on a vc707 Xilinx development board [79]. This board hosts a Virtex-7 FPGA, a 1 Gb RAM module a 1G Ethernet connection and can support a SFP+ optical module. The firmware implemented in the Virtex-7 is called *Polar-Bear*. It uses a GBT interface to communicate with the front-end and an IPbus [80] interface to communicate with the DAQ computer. IPbus is a control system based on Ethernet which was developed for the CMS experiment [81]. It was selected for its availability and relatively

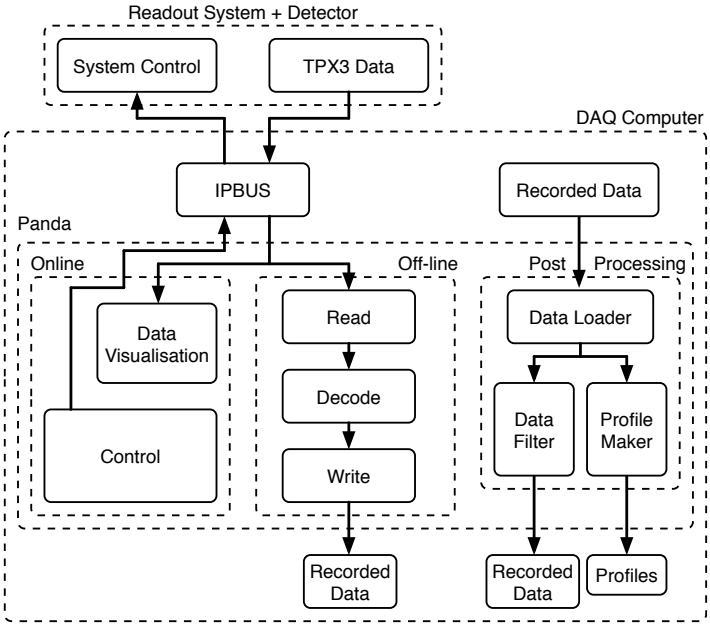

Figure 3.12: Panda readout software functional diagram.

simple implementation in the readout chain. In addition, the back-end is connected to the PS timing and is responsible for triggering the detector synchronously with the beam injection.

This implementation of the back-end is limited by the speed at which data can be transmitted to the DAQ computer. The front-end sends data at 2.56 Gbps while the back-end can only pipe data to the DAQ computer at 600 Mbps. For this reason, the RAM is used to buffer the surplus of events during an acquisition.

3.4.3 DAQ software

The DAQ software, called *Panda*, runs on the DAQ computer. It is written in C++ and provides a user with a Graphical User Interface (GUI) to have complete control of the readout chain (back-end, front-end) and the four Timepix3s. Panda also provides an *on-line* visualisation of the detector data, an *off-line* mode to record acquisition data to the disc and a suite of post processing tools.

A functional diagram of the DAQ software is presented in Figure 3.12. In on-line visualisation mode, the raw data received from the back-end is consumed to produce an image and it cannot be stored to disk. The term raw data refers to the individual events sent by the Timepix3. The decoded raw data can be used to produce a 2-dimensional image of the pixel surface showing either pixel counts or ToT values, integrated over a

defined time window. In the count map the colour corresponds to the number of counts in this time window, while for the ToT map the colour corresponds to the integral of the ToT values over the period of the time window. The event coordinates (row, column) are matched to scaled pixels on-screen to create the image. This mode is mainly used to setup the detector in preparation for a data acquisition run.

Once the detector is properly set, data are recorded to disk for later offline analysis by means of high-speed multi-threaded processes. The multi-threaded programme receives a stream of data from the back-end, decodes it to retrieve the individual events and stores the data in a Protocol Buffer [82] object. This object is then stored as a bit stream in a file on the DAQ computer for later analysis. The post processing tools may then be used to apply filtering and produce beam profiles.

In the early stages of the readout system development, the back-end could not store data in the RAM and the total readout speed was therefore limited to the IPbus 600 Mpbs bandwidth. For this reason raw data recording was separated from the live visualisation in order to gain speed and maximise the amount of data stored by the system.

3.4.4 Support systems

In addition to the equipment described so far in this chapter, the BGI requires a plethora of smaller support systems such as:

- High Voltage power supply
- Low voltage power supplies for the detector and readout system
- Bias voltage / current-meter supply for the Timepix3 bias
- Environmental sensors (flow meter, valves, humidity, temperature sensors...)

All of these are controlled by a Programmable Logic Controller (PLC) unit. The PLC is in charge of monitoring all the variables (voltage, current, temperature, etc.) and to control the system accordingly. It implements all important safeguards, preventing the user to damage the detector. For instance a user cannot turn on the detector if the cooling system is not activated.

3.5 Summary

The concept presented in chapter 2 has been implemented in a real device. The complete mechanical design of the PS-BGI was presented. The concept of hybrid pixel detector and a concise description of the Timepix3 was given. A new radiation tolerant readout system was developed for the PS-BGI.

Chapter 4

Prototype work

An important part of the R&D work realised for the PS-BGI project is the design of the detector electronics. Designing a detector which is compatible with the PS ultra high vacuum is challenging. The common use of polymers and adhesive in standard electronics makes them mostly incompatible with vacuum. In addition the radiation level present in the close vicinity of the PS beam is significant and limits even further the degree of freedom available for the design.

Once designed, the detector parts were built and assembled. The completed detector was then tested to verify that it was fit for final assembly in the instrument. The detailed design of the detector is given in section 4.1. Its fabrication is presented in section 4.2. The testing performed on the detector is presented in section 4.3.

4.1 Electronics design

4.1.1 Ceramic chip carrier

The ceramic chip carrier is a two sided Printed Circuit Board (PCB), shown in figure 4.1, comprising four Timepix3 HPDs, their 64 decoupling capacitors and six low-profile connectors. The board shape is a square of 114.3 by 114.3 mm, with M3 holes in each corner to fasten it to the cooling stack. The board is made of a 635 µm thick electronic grade Al_2O_3 substrate. This ceramic has the advantages of: a high dielectric constant that reduces dielectric signal losses; a thermal expansion matching silicon; and low degassing in vacuum. The top layer of the PCB is dedicated to the Timepix3 signals and power traces, while the bottom layer is mainly used for the ground. The metallisation is composed of a

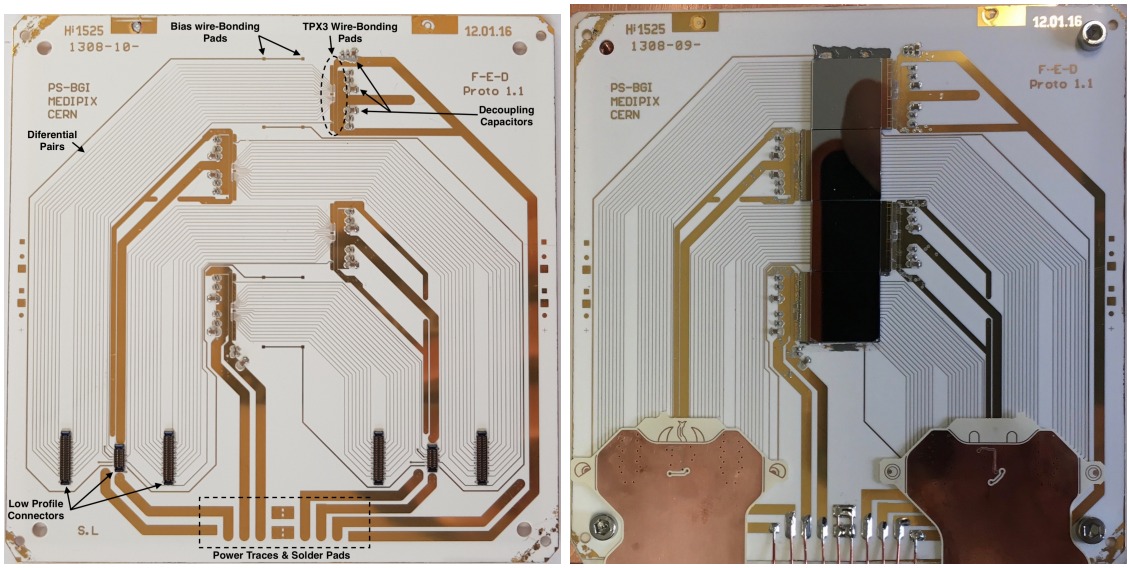

Figure 4.1: Left: Picture of a chip carrier board before assembly of the HPDs. Right: Complete chip carrier board with N-on-P assemblies. The flexible cables and the power delivery copper wires are visible at the bottom.

Ti/Cu/Ni/Au stack with the copper being ≈12 µm thick. The Ti layer is deposited using a thin film sputtering process, while the other layers are chemically formed. To prevent vacuum degassing, the standard polymer solder-mask used to protect PCB tracks is not applied.

The four hybrid pixel detectors are named chip one to four, chip one being the closest to the low-profile connectors. The chips are placed on the top side with 180 µm of spacing at their base. The sensor on the Timepix3 extends by ≈50 µm, leaving an expected 80 µm of spacing between them. The Timepix3 are oriented in the beam direction, two looking upstream and two downstream in an alternating pattern. This configuration is required in order to route all four Timepix3 signals with only the top metal layer.

The Timepix3's are electrically connected with 25 µm aluminium wire-bonds to a custom footprint on the chip carrier. A total of 17 differential pairs is required to communicate and control each Timepix3. The voltage for the pixel analog front-end, digital circuitry and ground add an additional 66 power connections per chip. This footprint is visible in figure 4.2, the tracks connecting to it are 30 µm wide with 30 µm spacing. The power connection are brought from the solder pads at the edge of the board to the front of each chip, while all signals are routed under the chip toward the connectors. To avoid short circuits, the Timepix3 are attached to the PCB using a thermally conductive but electrically isolating thermoplastic adhesive (Staystik [83]) or an epoxy with similar

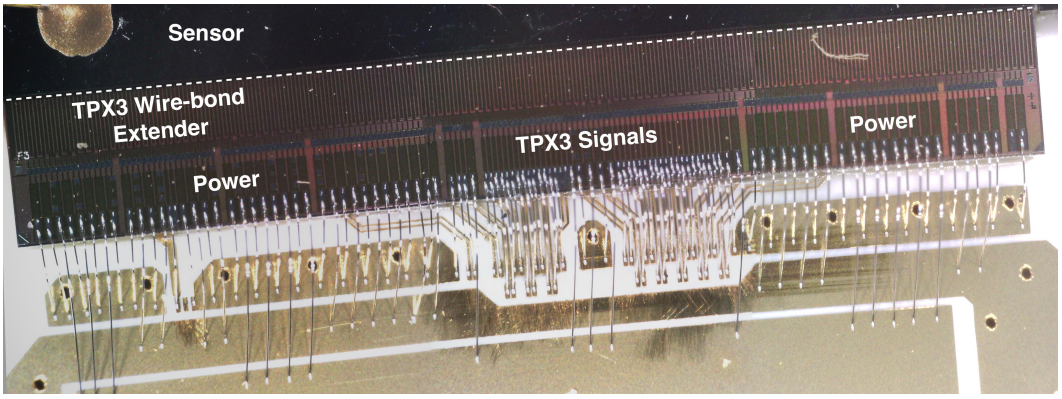

Figure 4.2: Close view of the Timepix3 footprint on the chip carrier. The centre is dedicated to the Timepix3 signals. The large metallised bands on the chip carrier are, from the ground and input voltages. The image is a composite of three separate images.

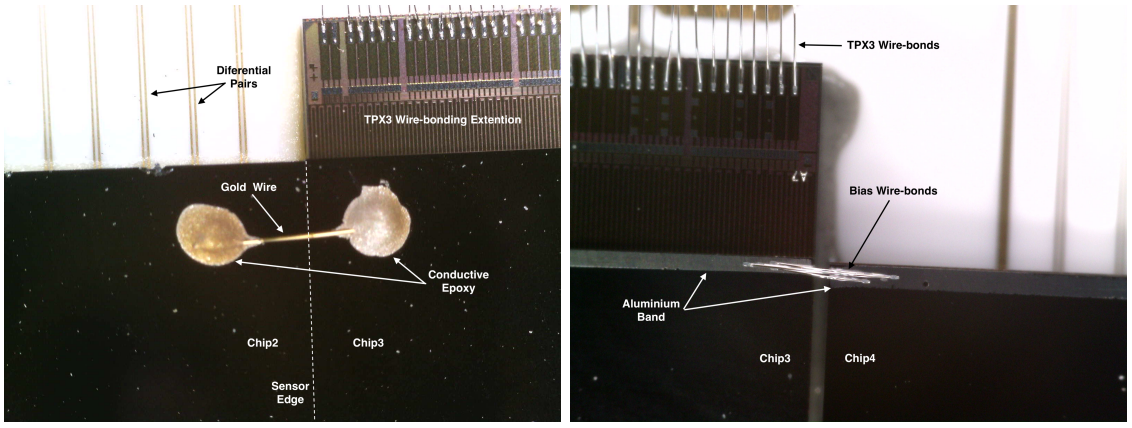

Figure 4.3: Left: P-on-N sensors without metallisation. The conductive epoxy and wire are visible at the centre. Some differential pairs of the chip carrier are also visible in the top left corner. Right: N-on-P sensors with the aluminium band, the wire-bonds connecting the two sensors are visible at the centre.

properties (EPO-TEK H70E [84]).

The bias voltage is connected to chip one and chip four sensors using wire-bonds. All sensor are interconnected to spread the voltage to chip two and three. Since the P-on-N sensors do not have any metallisation, they require the bias wire to be secured on the sensor using a conductive epoxy. On the other hand, the N-on-P sensors have the bias wires bonded directly to their aluminium strip. The former was used for the MKI prototypes, while the latter was used for the MKII prototype. These different methods are visible in figure 4.3.

Although both methods have the disadvantage of masking part of the sensor surface, the method relying on conductive epoxy yielded an inhomogeneous masking and approximate result.

All differential pairs on the board are designed to have a 100 Ω differential impedance. This was verified using Ansys HFSS [85], a 3D electromagnetic field solver. To limit the risk of cross-talk between the pairs, the spacing between them is maximised (≈300 µm). To lower the voltage drop on the Timepix3 power lines, these are made as wide (2 mm to 5 mm) and as thick as possible (12 µm). The power is brought to the chip carrier by ten 0.5 mm diameter solid copper wires directly connecting to the flange sub-D26 vacuum feedthrough. These are selected for their negligible resistance and better vacuum compatibility compared to tracks on a flexible printed cable.

Each Timepix3 requires 16 decoupling capacitors, four 10 nF, two 100 nF, two 4.7 µF, for its input voltages. These act as low pass filter to stabilise the chip input voltages, preventing sudden voltage drop which would cause the Timepix3 to malfunction. The capacitors are Multi-Layer Ceramic Capacitors (MLCC), selected for their radiation tolerance, vacuum compatibility and small form factor. They are placed as close as possible to the chips, while still allowing to perform the wire-bonding. The largest ones (4.7 µF) are too thick to fit on the top layer, they are therefore placed on the bottom side.

The connection to the FPCs is performed by the molex slimstack [86] low-profile connectors. They are placed by groups of three on the lower edge of the chip carrier. Each groups accommodates the signals for two Timepix3 plus the connection for two bias lines. To prevent signal distortions and cross-talk, differential pairs are interleaved by ground line at the connector. These connectors were selected for their mated height of 0.6 mm, small size and the use of Liquid Crystal Polymer (LCP) as base material. The low mated height allows the flexible cables to connect without being in contact with the instrument anode. The small size and use of LCP reduced vacuum degassing. A downside of using these connectors is their short life expectancy (≈ 50 mating cycles), which limits the possibility to test the system in the lab.

4.1.2 Flexible cable

The flexible cables are a pair of two layer flexible printed cables, each comprising three low-profile connectors and an array of high-density sub-D pins. They are presented in figure 4.4. The cables are roughly 240 mm long by 25 mm wide. Their shape is tailored to connect to the chip carrier, while bending 90° to connect with the flange sub-D78 vacuum feedthroughs. Moreover, their surface area is trimmed down to a minimum to reduce the potential vacuum degassing.

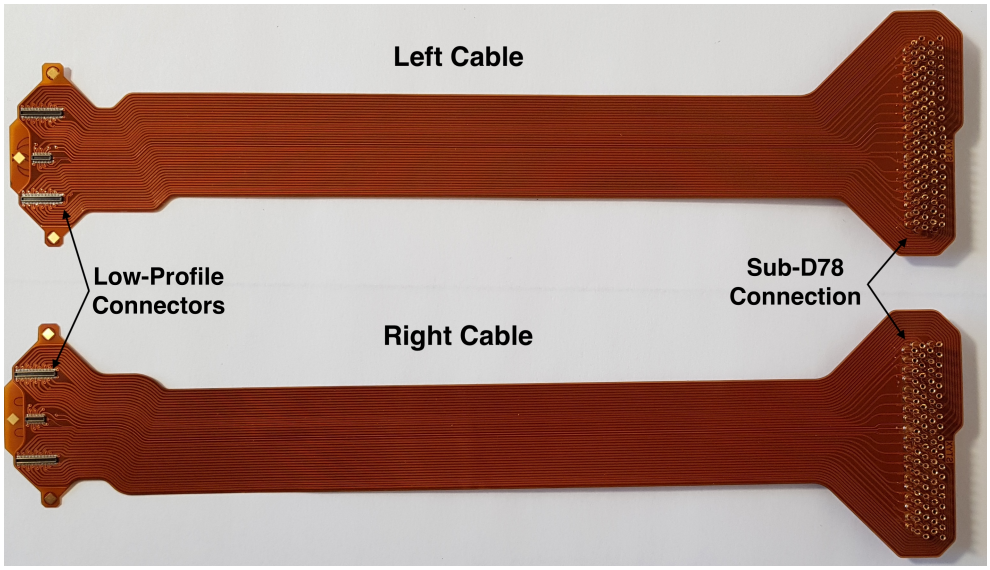

Figure 4.4: Left and right flexible printed cable. The version presented in this picture is made in Kapton and includes the solder-mask. The LCP cables were immediately installed after reception, no picture of them before the installation exists.

The cable substrate is a 100 µm thick liquid crystal polymer. LCP was chosen for its extremely low water absorption and low vacuum degassing according to NASA material database [87]. However, at the time of design, it was not yet tested and approved at CERN for use in the accelerator vacuum. The other alternatives such as Kapton and special polyimides were either known to be not compatible with our vacuum requirements or prohibitively expensive.

The cables metallisation is a single 25 µm layer of copper. To limit vacuum degassing no solder-mask is applied. Furthermore, the cables are limited to two layer since the process required to make higher layer count uses adhesives not compatible with the vacuum requirements.

The cables top layer is used for the Timepix3 digital signals and bias voltage, while the bottom layer is grounded. The differential pairs are designed to have a 100 Ω differential impedance, resulting in a track width of 75 µm and spacing of 100 µm.

The low profile connectors are arranged to perfectly mate with their counterpart on the chip carrier. In order to strengthen the connector region and avoid unwanted breakage, a solid stiffener should be glued to the cable. However, due to the vacuum requirements, this cannot be done. As a consequence the mating of the cables with the chip carrier is a very delicate operation and it is highly unlikely that they would survive unmating, so are therefore considered single use cables.

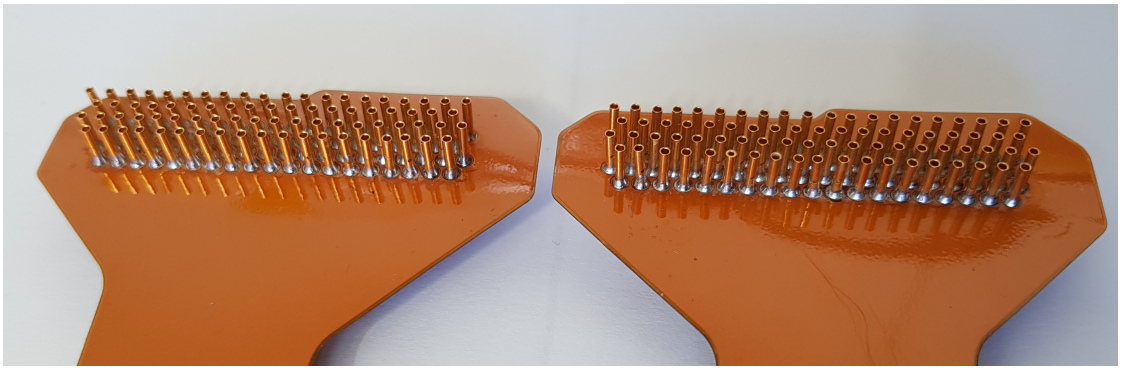

Figure 4.5: Individually soldered sub-D pins are used to connect to the feedthrough.

Since no vacuum compatible sub-D78 connector existed, the connection to the feedthrough is achieved by directly soldering sub-D crimping pins to the LCP cables. Moreover, the impossibility to use a stiffener makes the mating of the cables with the feedthrough require special tooling.

In order to allow for the design to be tested in the lab, the cables were produced in kapton with and without stiffeners. The LCP cables were preserved for the final assembly of the instrument.

4.1.3 Detector power and support electronics

In addition to the main vacuum electronics, a set of custom electronic boards are used to power the detector and connect it to the readout system. These are briefly introduced below.

4.1.3.1 Detector power scheme

Each Timepix3 requires two separate 1.5 V voltage rail, one to power its analog front-end and one to power its digital circuitry. In nominal configuration, the analog side draws a constant current of ≈0.5 A, while the digital side draws 0.5 A when idle and up to 1 A when under load. Ideally these voltages shall be as stable as possible, their stability defines the the stability of the Timepix3. The analog voltage is especially important, since it is used as a reference for the Timepix3 threshold. For this reason analog and digital voltages are usually separated, the analog is supplied by a linear voltage converter and both voltages are supplied as close as possible to the chips to reduce effects from long copper lines.

Typical power delivery schemes include a pair of low voltage DC/DC converters on the same board as the Timepix3. However, due to our vacuum requirements, having

Figure 4.6: The Hydra power board. The board presented in this picture is configured for a usage in parallel.

radiation tolerant DC/DC converters on the chip carrier is impossible.

As a consequence, the Timepix3 voltages are provided by *Hydra* power boards placed on the flange of the instrument. This board, presented in figure 4.6, hosts a pair of radiation tolerant DC/DC FeastMP converters. The DC/DC FeastMP is a switched mode step-down converter made by CERN [88]. It was chosen for its availability and high tolerance to Single Event Upsets (SEU). The Hydra board receives a 10 V input and convert it to two 1.55 V with a maximum power of 10 W each. Alternatively the Hydra can be operated in a cold redundancy mode where only one 1.55 V output is provided. This mode is not used in the PS-BGI.

Two hydra board are used to power the detector, one board provides the analog and digital voltages for chip one and chip three, while the other powers chip two and four. As a consequence chip one/three and chip two/four share their digital and analogue voltages. This configuration is chosen because the analogue and digital supply shall be separated to lower the noise on the analog side. Moreover a single feast module could not power all four Timepix3 at once.

To estimate the voltage drop caused by the long path between the feastMP and the Timepix3, the resistive path between those was modelled as resistor network. A drop between 30 mV to 70 mV is expected. The main bottleneck is the carrier board, causing most of the drop. Moreover the Timepix3 power lines have different lengths and size for each chip causing the drop to increase between chip one and chip four. In an attempt at mitigating this issue, the voltage provided by the Hydra board is bumped to 1.55 V. Enlarging the tracks on the chip carrier was not an option as there was no space left on

the board.

As it is mentioned in chapter 5, this solution is working but instabilities in the power delivery have been observed.

4.1.3.2 Flange board and sub-D78 board

The sub-D78 board connects the airside of the sub-D78 vacuum feedthroughs to the front-end readout. It has on one side a pair of sub-D78 connectors and on the other a set of RJ45 connectors.

The flange board is a patch panel board connecting the hydra boards to the sub-D26 feedthrough. It also comprises connections for environmental sensors used to monitor the instrument surroundings.

4.2 Fabrication

This section details the fabrication, assembly and procurement of the chip carrier and flexible cables.

4.2.1 Chip carrier

The hybrid pixel detectors were sourced from Advacam [89]. The company produces the sensor and bump bonds it to the Timepix3. The assemblies delivered are guaranteed to be functional with minimal defects. As said in chapter 3, two batches of assemblies were procured. The first batch with P-on-N sensors was fully tested with the help of J.Alozy (CERN Medipix). The test included communication with the Timepix3 and detection of particles from Fe55 and Sr90 radioactive sources. The capacitors and low-profile connectors did not require testing and were procured through standard electronics suppliers.

The chip carrier board were produced by Hightec [90] a Swiss based company. Due to technical issues they experienced, the production of the boards took approximately four months. In total five boards were ordered. Out of those, Hightec fully assembled two boards with P-on-N assemblies attached with epoxy. These are subsequently referred to as MKI board one and two. The first assembled board ran into an issue where some epoxy covered some of the wire-bonding pads, preventing chip two from being connected. For this reason this board was not considered for installation in the PS. Later, a third board was assembled by the CERN electronics assembly workshop and bonding lab, with N-on-P

assemblies attached with Staystik. This board is referred to as the MKII board.

The reason for the difference in adhesive is that at first the epoxy was considered a better choice for vacuum, but it was letter proven wrong by testing the Staystik. In both cases the bare copper wires used to connect to the flange sub-d26 feedthrough were soldered by the CERN workshop after assembly of all other components. The boards were cleaned (where possible), visually inspected for defects and stored in a hermetic plastic box.

4.2.2 Flexible printed cables

The production of the flexible printed cables was first given to QPI BV (now renamed Fineline QPI BV) [91] a PCB producer based in the Netherlands. However, the production was not successful and so a second attempt was made the CERN electronics workshop, which ultimately proved successful.

The LCP was sourced from Panasonic in the form of copper clad laminates [92]. This new material integrated seamlessly in the standard flexible PCB process.

The lack of a solder-mask made the assembly of the sud-D78 notoriously difficult. The small gaps between solder-pads were prone to solder bridges and the thin LCP was easy to melt with the soldering equipment. The process ended up being entirely manual. Nonetheless the production was fairly successful and only a couple of board were discarded after visual inspection.

4.3 Detector testing

Once assembled, the chip boards and flexible cables were subjected to a series of tests to determine whether or not they were working properly and could be installed in the instrument. These tests were incremental and comprised basic electrical tests, vacuum acceptance testing, testing of the cooling system and HPDs sensor testing. Finally the detection of low energy particles was verified with a weak Fe55 radioactive source.

Due to the various delays these test were performed in the days preceding the final assembly and installation of the instrument.

4.3.1 Electrical tests

Due to the facts that the Timepix3 wire-bonds are exposed, that the boards do not have solder-mask and that the feature size on the boards is relatively small, electrical failure related to light mechanical damages can occur. It is therefore crucial to ensure that the chips are properly connected and that no short circuits are present. In order to verify this, the following test procedure is employed.

The chip board was installed in a partially assembled PS-BGI. In function of when the test was performed, final assembly or first test, the semi-rigid Kapton cables or the LCP cables were used to connect to the flange. The chip board was powered by a bench power supply. The analog and digital voltage were set to 1.55 V to account for the voltage drop in the cables. The readout system was connected to the flange and controlled by a laptop. The cooling system was inactive, the detector was cooled by passive air cooling.

At first, the chips were powered-on one by one and their power consumption was monitored. If no anomaly was detected, the readout system was connected and the test was repeated. The readout system was used to verify that the Timepix3 could receive commands and that the SLVS readout links were all sending data properly.

This test showed that none of the assembled board were defect-free. Both MKI boards have connection problem with chip three, while the MKII board has a small connection problem with a non-critical signal. This prevented the Timepix3 chip from being properly tested and calibrated, but it could still be used. Despite this, the MKI board two and the MKII board were cleared for installation as there was no time to prepare replacements.

4.3.2 Vacuum acceptance testing

In order for the detector to be installed in the PS it needs to pass a vacuum acceptance test. This test assess the total degassing of the components and the composition of the gas released. These two aspects are important as they affect the lifetime of the beam circulating in the machine. The tested parts are placed in a test chamber where the background gas pressure and gas composition have already been measured. The degassing is estimated from the chamber pressure and the effective pumping speed, while the gas composition is measured using a Residual Gas Analysis (RGA) device.

The degassing limit for the PS-BGI is set to $5 \times 10^{-6}\,\mathrm{mbar\,l\,s^{-1}}$. The criterion for the gas composition is that all gas species with mass between 18 and 44 u shall have individual concentration a hundred time lower than that of water (18 u) and that gas species between

Table 4.1: Measured vacuum degassing from the chip boards and flexible cable after 24h pump-down.

	MKI board 1	MKI board 2	MKII board	LCP flexible cable
Vacuum Degassing [mbar l s^{-1}] (After 24h pump-down)	3.5×10^{-6}	1.8×10^{-6}	3.4×10^{-7}	2.2×10^{-6}

44 and 100 u shall have concentration 1000 times lower than that of water.

All assembled chip boards and one flexible cable were tested individually. The results for the degassing rate is presented in table 4.1. The details of the testing procedure and RGA scans are available in these CERN EDMS documents [93, 94]. All tested parts have successfully passed. Nonetheless one can observe that the two detector assembled with epoxy have a degassing significantly higher than that of the one assembled with Staystik.

4.3.3 Cooling system testing

The aim of this test is to ensure that the cooling system is effectively cooling the detector in vacuum. This test was performed on chip boards that were assembled on the real PS-BGI during the assembly of the instrument. For this reason, only the MKI board two and the MKII board were tested. The test is setup as follows.

A partially assembled PS-BGI with the detector, flexible cables and cooling stack is inserted in the instrument vacuum chamber. The water cooling circuit is connected to a portable lab chiller. The electrical tests presented earlier is repeated to ensure proper connections before the vacuum chamber is sealed. The detector is turned on and the chips temperature is monitored using the TPX3 internal temperature sensor and the readout system. The chiller is turned-on with 15 °C water to avoid condensation. The detector is powered-on and the chamber is pump-down to a pressure close to 1×10^{-5} mbar. At this pressure the contribution from convective air cooling is negligible. The water temperature is then finally lowered to 5 °C.

To mitigate the risk of damaging the detector, in the event of a malfunction of the cooling system, the heat load is limited to two Timepix3 at the start. This results in a heat load of ≈3 W. In these conditions both chip boards displayed a similar steady state temperature of ≈50 °C. The two remaining Timepix3 are then powered-on, bringing the heat load to ≈6 W. With this load the MKII board reaches a steady state temperature of ≈85 °C, while the MKI board reaches ≈90 °C.

These results showed that the cooling system is effectively cooling the detector. the difference between the two board temperature can be explained by the fact that the gold foil used in the cooling stack is manually applied and that the pressure on the fastener can vary.

The steady state temperature each detector reached is in the upper limit of what is considered safe. Moreover, during data acquisition the heat load of the Timepix3 can rise to 4 W, which could drive the detector temperature above ≈100 °C. For this reason, methods to mitigate the detector heating are put in place. These are presented in chapter 5.

4.3.4 Detector bias current

In order to verify that the bias voltage is properly connected to the sensors, it is scanned from 0 V to 35 V for the P-on-N sensors and from 0 V to −35 V for the N-on-P sensors. The current drawn by the sensors is monitored and a characteristic I-V curve is produced. Since all sensors are inter-connected this has to be done for the four sensors in parallel. The measurement is performed using a voltage source measure unit. The boards are placed in the vented PS-BGI vacuum chamber to prevent ambient light from biasing the measurements. Figure 4.7 presents the I-V curve measured for the two tested boards.

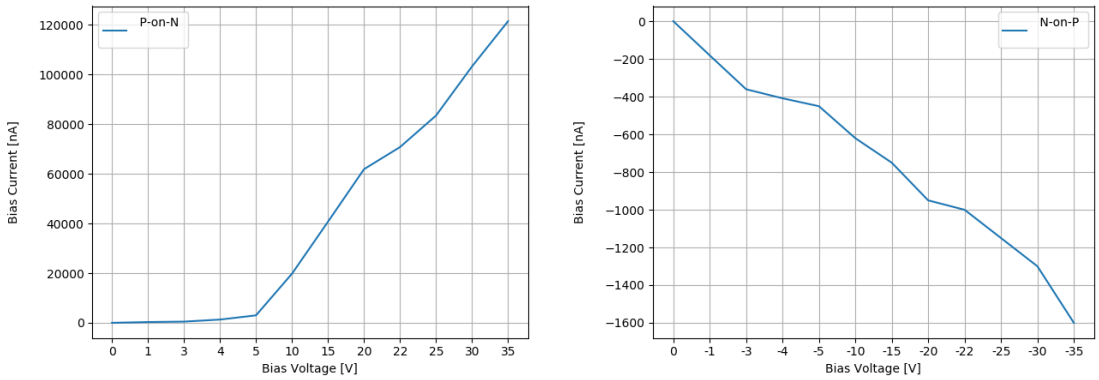

Figure 4.7: Left: I-V curve for the MKI board with P-on-N sensors. Right: I-V curve for the MKII board with N-on-P sensors.

From measurements done on other assemblies in our possession, mounted on standard chip boards from Medipix, a sharp rise and a plateau of the current at ≈900 nA was expected [95]. This is however not the case, both boards display a resistive response with voltage. Moreover, the current seen for the P-on-N sensors is too high to originate

from healthy sensors. The current from the N-on-P sensors, although a little high, is still conceivable.

The measurement was repeated several times while also verifying the measurement setup against a standard Medipix Timepix3 chip board. No anomaly was found and the measurement had to be accepted as is.

Due to the limited time available before the installation of these board in the PS, the source of this problem could not be fully investigated. A later review of the images made during the visual inspection of the MKI board revealed that some of the epoxy glue used to secure the Timepix3 was sucked in between two of the chips to the point where it was in contact with a sensor. This might explain the source of the resistive leakage current observed. No obvious causes for this behaviour was found for the N-on-P sensors. Moreover, no effect on the chips performance or behaviour were observed with either of the sensor types.

4.3.5 Low energy particle detection

The detection of low energy particles is a test aiming at verifying that the assemblies were not damaged during the assembly of the detector and that they had the capacity to detect the BGI ionisation electrons.

A Fe55 source was loaned from CERN Radio-Protection (RP) group. Fe55 is selected for its emission of Auger electrons and photons with an energy close to 5.5 keV. Since the source is not vacuum compatible, this test is done in atmospheric conditions. The electrons have therefore little chance to reach the detector and most probably only the photons are detected.

The detector is powered, the sensors are biased with 30 V (or −30 V) and the readout system is connected. The Timepix3 chips are left in their base configuration and the threshold is raised to a point where no noise is visible. The source is placed a couple of millimetres above one of the hybrid pixel detector The shutter is then opened, if nothing is detected, the threshold is lowered until the particles from the source are detected. An example of the recorded data is presented in figure 4.8.

All chips easily detected the particles from the source, except chip three from the MKI board. No inhomogeneity in the detection was observed. Despite the malfunction of chip three from the MKI board, this test confirmed that the detectors were working as intended.

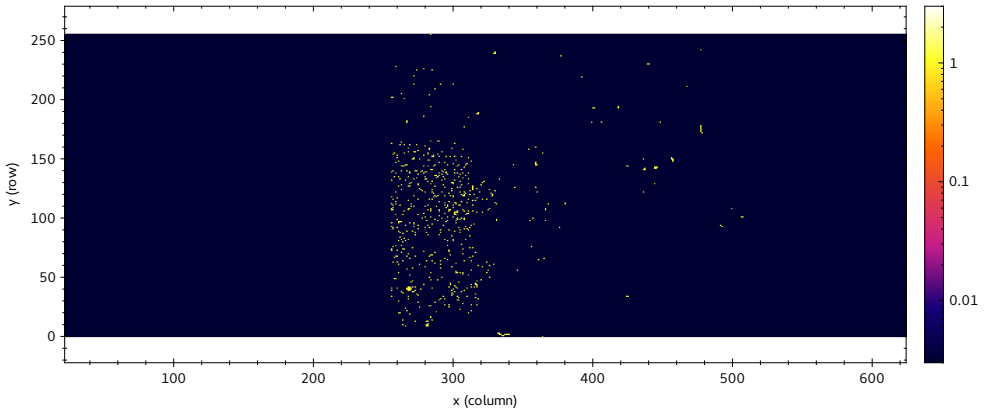

Figure 4.8: Integrated counts of the particle detected by chip one of the MKII board when exposed to the Fe55 source. Image taken from the live view of the Panda readout software.

4.4 Summary

The design production and testing of the PS-BGI detector was presented. Two chip carrier boards were successfully tested and approved for installation in the instrument: One board with P-on-N assemblies where chip three is non functional; and one board with N-on-P assemblies were all chips where functional. The flexible cable design was implicitly tested. All components where approved for use the PS primary vacuum by the CERN vacuum group.

Chapter 5

Assembly, installation and commissioning

With a now functioning detector, the instrument was fully assembled and installed in the PS. These two steps are presented in Section 5.1 and 5.2 respectively. Following its installation, the detector was prepared for data acquisition. This procedure is detailed in Section 5.3. Once prepared, the PS-BGI first measurements were used to quantify the background present at the instrument location. The detection of ionisation-electrons from the beam quickly followed. These first measurements are presented in Section 5.4.

At this point, it is useful to clarify the chronology of installed instruments. Two complete instruments were assembled and installed in the PS. The first was installed and operated during the 2017 run. A significant number of issues plagued this instrument. Its detector had the P-on-N chip carrier on which chip three was faulty and there were problems with the sensors bias, which did not follow the expected I-V curve behaviour of a semiconductor. The readout system was still in its infancy, and the data post-processing presented in Chapter 6 was nonexistent. Moreover, the high voltage circuit did not allow to reach the nominal $-20\,\mathrm{kV}$ and would often discharge without warnings. These issues significantly reduced the potential of this instrument. For this reason, it was primarily used as test-bed to learn how to operate the instrument, and to debug the readout system.

This first instrument was then removed and replaced by the second one in 2018. This second instrument had the N-on-P chip carrier where all chips were functional. Its bias voltage had no issue, the readout system was improved, and its high voltage could operate at the nominal value. The rest of this document only relates to the second instrument installed in 2018.

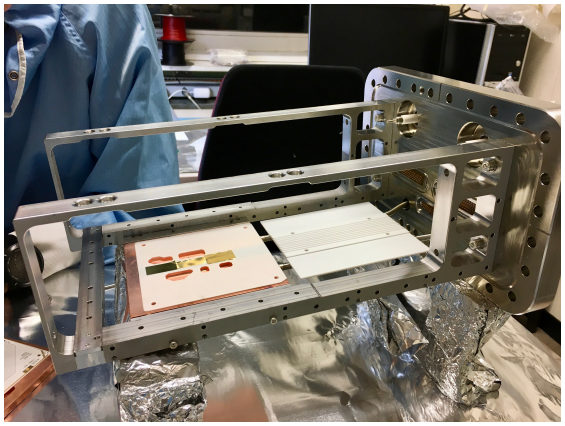

(a) Assembly of the cooling stack.

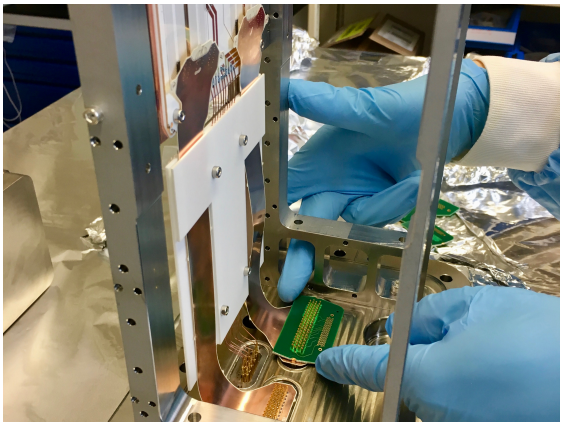

(b) Installation of the LCP flexible cables onto the flange.

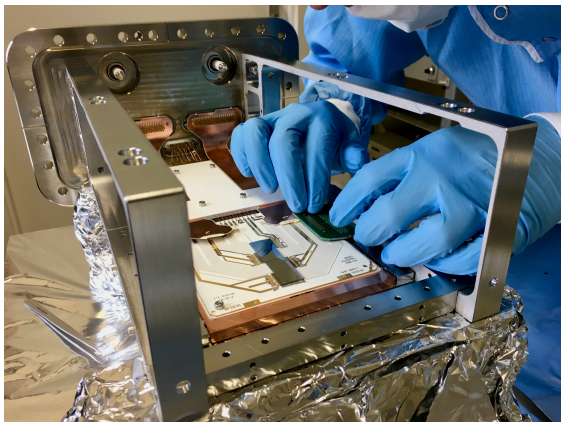

(c) Mating the flexible cables with the chip carrier.

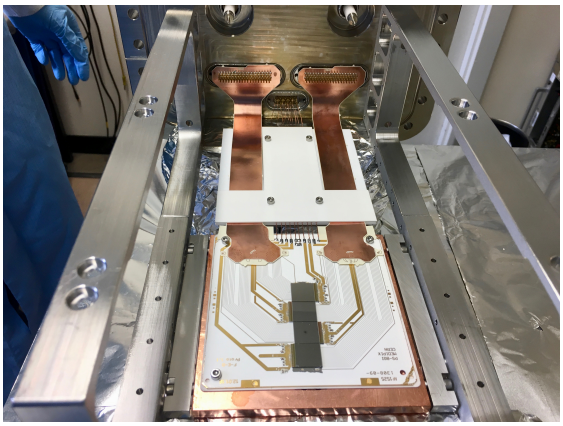

(d) Completed detector sub-assembly.

Figure 5.1: Putting together the detector sub-assembly.

5.1 Instrument assembly

The instrument was assembled in the PS-BGI lab. To ensure proper vacuum standards, all parts were cleaned and individually packaged by CERN cleaning services. The tools used for the assembly were also cleaned, and a clean workbench was prepared. Figure 5.1 presents the assembly of the detector sub-assembly. The instrument was constructed on the flange by following these steps:

1. The support arms were fastened to the flange, and the cold head was attached to them.

2. The ceramic wire guide for the chip carrier power-lines were attached to the cooling pipes.

3. The cooling stack was assembled and the chip carrier was fastened to the cold head.
4. The power lines of the chip carrier were installed in the ceramic guide and then mated to the sub-d26 feedthrough.
5. The flexible cables were put in place.
6. The detector was tested to ensure that everything was connected properly (e.g. Electrical continuity, correct communication with the read-out system and sensor bias I-V curve).
7. The Faraday cage side walls and top cover were attached to the support arms.
8. The steel honeycomb was attached to the anode.
9. The anode was fastened to the support arms.
10. The cathode was installed on the support arms, a thin copper wire links it to the high voltage feedthrough.

Figure 5.2 shows the completed instrument before it was sent to the vacuum group for vacuum outgassing test. The instrument passed the test with a total vacuum outgassing of $8.3 \times 10^{-7}\,\mathrm{mbar\,l\,s^{-1}}$, which is below the limit of $1.5 \times 10^{-6}\,\mathrm{mbar\,l\,s^{-1}}$ set for the PS-BGI. The test report is available here [96]. After the vacuum acceptance test, the instrument underwent high voltage conditioning to allow it to hold the nominal $-20\,\mathrm{kV}$ on the cathode. The procedure consists of slowly raising the voltage until signs of discharge(s) are detected

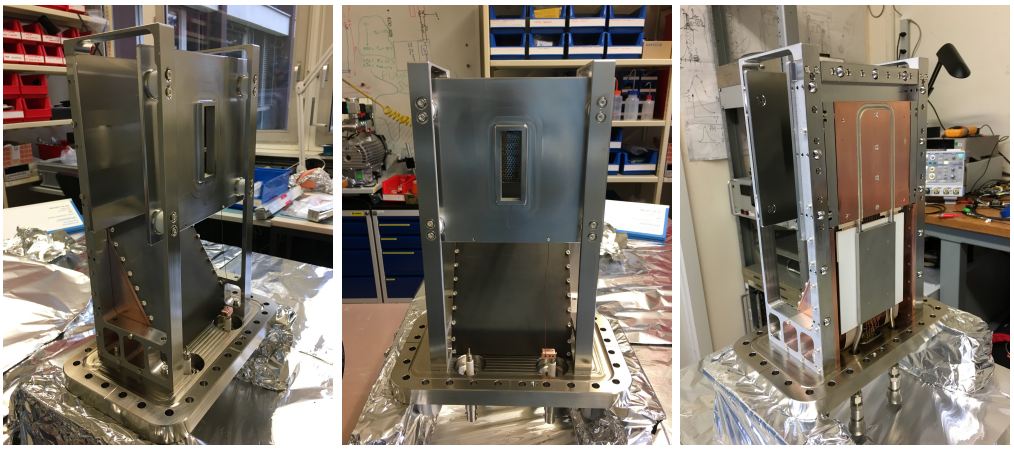

(a) Side view. (b) Front view. (c) Back view.

Figure 5.2: Fully assembled PS-BGI instrument. The top cover of the faraday cage is carbon coated.

(e.g. current spikes from the power supply). The voltage is then held at this level until the discharge activity dies. This process was repeated until the operational voltage was reached. This high voltage conditioning procedure is described in [97]. The instrument was then stored waiting for its installation in the PS.

5.2 Installation in the CERN PS

Once assembled the instrument was installed in PS straight section 82. The installation required to break the vacuum in the sector. This is only possible during the winter shutdown of the accelerator complex or during a 36 hours technical stop of the PS which occurs two or three times a year. Before the installation, several copper cables and optical fibres were laid between the counting room rack and the instrument location. A dedicated 6 °C water line was installed for the detector cooling. The installation is presented in Figure 5.3.

The vacuum chamber was installed on the support table, requiring a first vacuum intervention. Later, the instrument was brought to the PS and installed in the vacuum chamber. The vacuum was reestablished, and the instrument was leak checked by the CERN vacuum group. The magnet was tested and installed independently of the rest of the instrument by the CERN magnet group. Finally, the front-end and back-end electronics were put in place, and the instrument was tested to ensure that the installation was successful (e.g. communication with the readout system, detection of background particles).

5.3 Instrument preparation for data acquisition

The instrument is prepared for operation by equalising the Timepix3 and masking the noisy pixels. Additional operations such as the time-walk correction and energy calibration were not implemented due to limitations in the readout system capabilities.

5.3.1 Equalisation

The Timepix3 pixels are given a user-defined threshold. This threshold is referred to as the global threshold. Due to the nature of the fabrication process used to make the Timepix3 (CMOS), each pixel is unique. This causes the value of the global threshold seen by each pixel to deviate slightly from the value set by the user. The threshold seen by the pixel

(a) The PS-BGI open vacuum chamber with the magnet surrounding it

(b) Installing the instrument in the vacuum chamber.

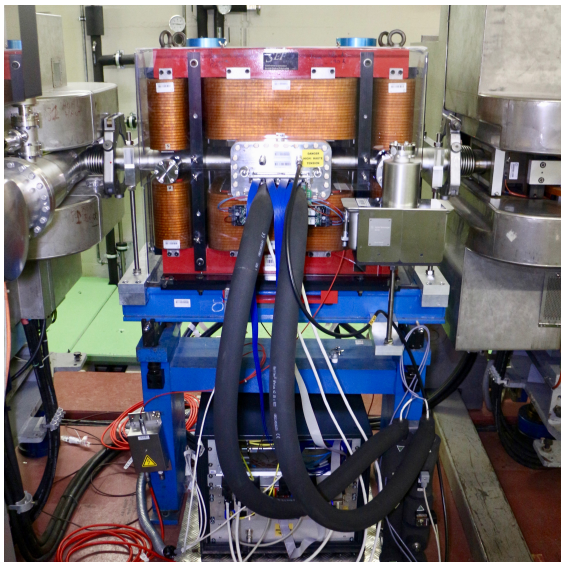

(c) Completed installation of the instrument.

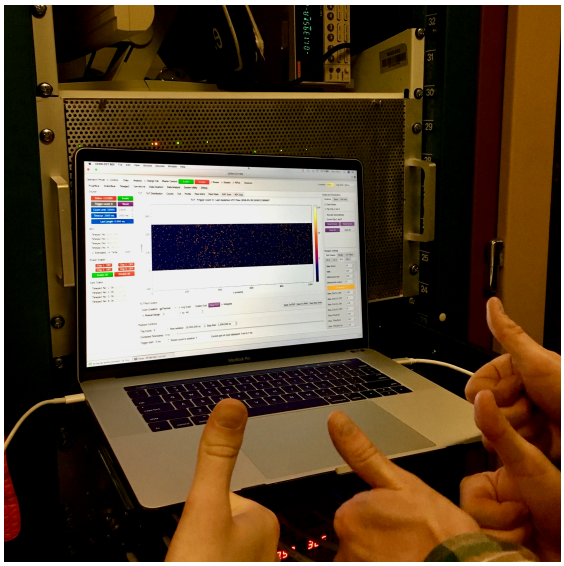

(d) A first test of the detector recording background radiation.

Figure 5.3: Installation of the instrument in the PS.

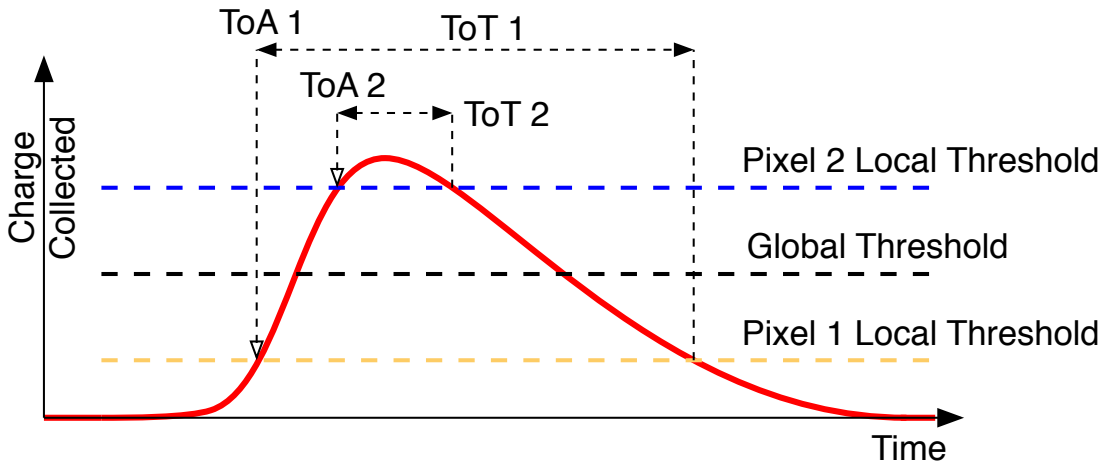

Figure 5.4: TOA and TOT response to a common input for different pixels.

is referred to as the local threshold. An example is shown in Figure 5.4. Pixel two has a higher local threshold than pixel one, leading to the two pixels measuring different values of TOT and TOA for a common input. This threshold dispersion leads to a spread in the TOT and TOA measurements, which is problematic when performing measurements with the PS-BGI. The TOA spread causes a degradation of the instrument time resolution, while the TOT spread causes pixels with a low local threshold to become noisy when Timepix3 is operated close to the noise floor (more on noisy pixels in section 5.3.2). This effect subsequently lower the ionisation-electron detection efficiency as the global threshold has to be raised. In the context of the PS-BGI, this second aspect is the most important one since noisy pixels caused issues during operation (see Section 5.5).

The noise floor is the limit below which pixels are triggered by the electronics noise in the Timepix3 and sensor rather than by ionising radiation. It is assumed uniform across the chip and is mostly affected by the chip temperature.

In order to limit the pixel threshold dispersion, a procedure called *equalisation* is performed. The Timepix3 features the possibility to locally adjust the threshold in the pixels using a four bits internal Digital to Analog Converter (DAC). This DAC converts a four bit digital value (from 0 to 16 in decimal base) into a voltage which is then added to the global threshold to create the pixel local threshold. The equalisation procedures is based on the measurement of the threshold dispersion and its minimisation via the optimisation of the pixel local threshold for each pixel. The method presented here is adapted from [98].

5.3.1.1 Threshold dispersion measurement

The threshold dispersion is measured by performing threshold scans. The global threshold is scanned across a reference signal while the occupancy for each pixel is recorded. The reference signal is either a user defined test-pulse injected in each pixel or the noise floor. In our case the readout system does not allow the use of external test-pulses, the noise floor is therefore preferred. The occupancy is defined as the percentage of time a pixel is triggered relative to the shutter length. In practice the Timepix3 is operated in event counter + integrated TOT mode with a frame-based readout. The occupancy Occ_{pixel} is then calculated with

$$Occ_{pixel} = \frac{iToT_{pixel}}{T_{shutter}}, \tag{5.1}$$

where $iToT$ is the total time that the pixel spent above the threshold and $T_{shutter}$ is the shutter length.

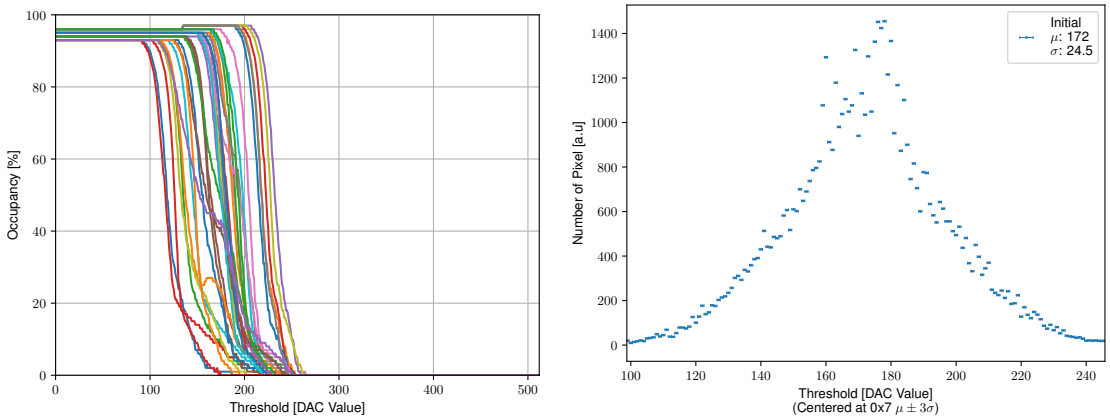

(a) Threshold scans for 30 random pixels. (b) Threshold distribution histogram.

Figure 5.5: An S-curve example and the threshold distribution for a non-equalised Timepix3 chip.

The threshold scan results in a so-called *S-curve* unique to each pixel. The pixel threshold is defined as the threshold from which the occupancy crosses the 50 % mark. The standard deviation of the pixel-threshold distribution is the measure of the threshold dispersion. It is used as a figure of merit for the following pixel local threshold optimisation. An example is given in Figure 5.5. The S-curves for 30 randomly selected pixels in a Timepix3 are visible, as well as the histogram of the threshold distribution from the complete matrix.

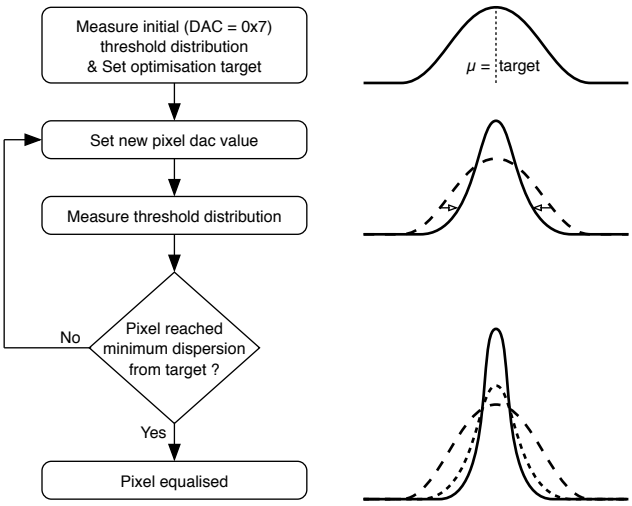

Figure 5.6: Simplified flow-chart of the optimisation procedure. Individual pixel DAC values are changed iteratively to reduce the spread in the pixel local thresholds.

5.3.1.2 Pixel local threshold optimisation

The pixel local threshold optimisation tries to minimise the threshold dispersion by tuning the local threshold of each pixel. The complete process is presented in Figure 5.6.

All pixels are set to the same central DAC value of 7 out of 16 and the initial threshold distribution is measured (see example in Figure 5.5). The mean of this distribution is used as the target for the local threshold optimisation. The optimisation process is then started. For each pixel, if its local threshold is above the target, it is lowered by one DAC value. While if it is below the target it is increased by one. The threshold dispersion is then re-measured and the optimisation step is repeated.

Since there are only 16 DAC values and the pixels start at position 7, the maximum number of optimisation steps is limited to eight. A pixel is considered equalised when the local threshold yielding the smallest deviation from the target is found. The result of the equalisation is the final DAC value for each pixel. Figure 5.7 shows a comparison between the initial threshold distribution and the one obtained after equalisation. The standard deviation of the distribution for each optimisation step is also presented. In this example the threshold dispersion is reduced by a factor five.

In addition, the mean of the final threshold distribution can be used as a measure of the noise floor position in units of the global threshold. This is used to decide the minimum safe threshold at which to set the chip.

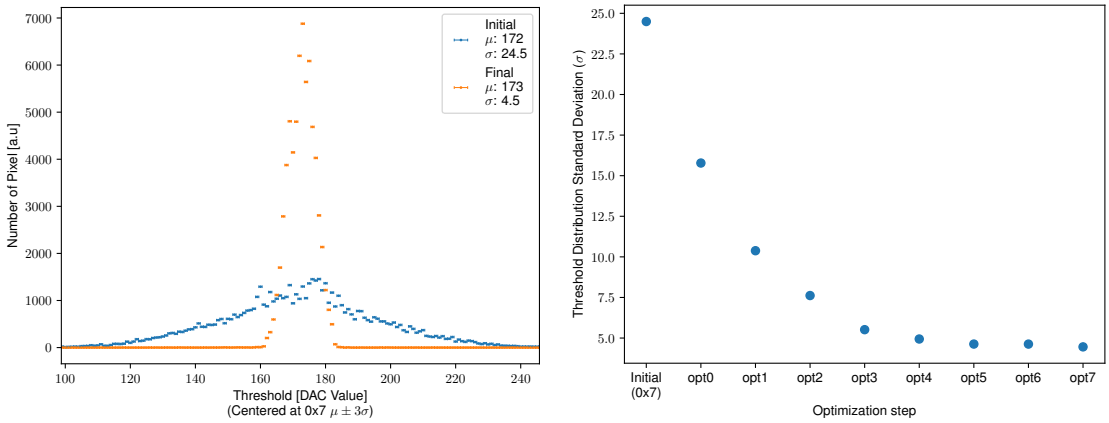

(a) Threshold distribution histogram of the initial and final equalisation step.

(b) Standard deviation of the threshold distribution for each optimisation step.

Figure 5.7: The threshold distribution before and after equalisation. The spread is reduced by a factor five.

5.3.2 Noisy pixel masking

Noisy pixels are pixels which are triggered by processes other than ionising radiation. They are sorted into two categories; transient and continuous. Transient noisy pixels are pixels that become noisy when their local threshold gets too close to the noise floor. In my own experience, the number of transient noisy pixels ranges from less than 10 in a well equalised Timepix3 to more than 200 in a non equalised one. Continuous noisy pixels are malfunctioning pixels, these are few (<10) in a Timepix3 that passed the production quality control. Either way, noisy pixels are problematic for the following reasons:

- Events from noisy pixels contribute to the noise on the profile measurement.
- Noisy pixels generate a large amount of events, which can quickly saturate the readout system.
- Noisy pixels can trigger *power glitches* (see Section 5.5).

In order to mitigate these adverse effects, the Timepix3 features the possibility to deactivate individual pixels on demand. Noisy pixels are identified with the following method. No beam is present in the PS and the cathode high voltage is off. This reduces the amount of unwanted background signal. The chip is then set for operation at the required threshold, and the shutter is opened for an arbitrary period of time. The data recorded during this test is then used to generate a distribution of the pixels triggering-frequency. An example of a typical distribution is presented in Figure 5.8.

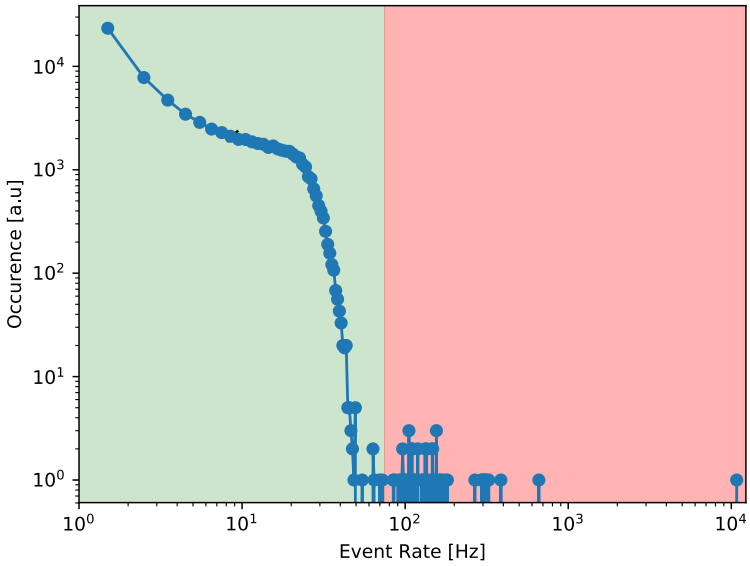

Figure 5.8: Distribution of the triggering frequency of pixels in the PS-BGI detector. The green area represents the values below the limit, while the red area represents the noisy pixels.

In this distribution, noisy pixels appear as outliers with a high frequency, while valid pixels constitute the bulk with a low frequency. The limit between valid and noisy pixels is calculated with

$$Limit = \mu_{dist} + N\sigma_{dist} \tag{5.2}$$

where μ is the mean of the triggering-frequency distribution, σ is the distribution standard deviation and N is a user defined factor. This method works based on the fact that typically a large majority of pixels are valid. The distribution mean is therefore a good indicator of the location of the bulk of the valid pixels.

Ideally, the distribution is measured in an environment with little to no background signal. In these particular conditions, the limit could be set to the minimum frequency of one count per unit time; leading to the conclusion that any pixel that triggered during the test is noisy. This is however not possible as the Timepix3 is sensitive to cosmic muons and radiation from activated materials inside the beam pipe. This causes the triggering frequency distribution to look like Figure 5.8, where the non-noisy pixel triggering rate is in the order of few tens of Hertz. The limit between noisy and non-noisy pixel had therefore to be chosen based on the test condition to achieve the best compromise between finding noisy pixels and not removing valid ones.

Pixel masking is done at two occasions, during the setup of the Timepix3 and in post-processing. The former is used to prevent already existing noisy pixels from affecting the data acquisition, while the latter removes events from pixels which became noisy during the acquisition (see chapter 6).

5.4 First measurements

Shortly after the installation, the first measurements with the instrument were performed. The objectives were to quantify the background signal, determine if the PS-BGI would work in the PS environment and if the instrument would detect the ionisation electrons created by the beam.

5.4.1 Background measurements

The background was measured with the following conditions:

- Without the beam and without high voltage on the cathode
- Without the beam and with high voltage on the cathode
- With the beam and without high voltage on the cathode

The measurements without the beam intended to measure the background signal from the activated materials surrounding the detector and the potential effect of the cathode high voltage on it. The measurements with the beam are intended to measure both the background from activated materials and beam loss. The beam used for the measurement is a standard LHC25 beam. In both cases, the instrument magnetic field was not present. Figure 5.9 presents a count image of the background signal measured without the beam for an integration time of two seconds. A count-image is an image where the colour scale represents the number of events recorded by each pixel. The image is presented as if the four Timepix3 comprising the detector were a single large detection area. Chip one spans the columns [0, 255], chip two spans [256, 511], chip three spans [512, 767], and chip four spans [768, 1023]. This representation gives a view of the spatial distribution of the events on the detector surface.

The images show a wide diversity of curly tracks, small clusters and single events. Curly tracks and single events are most likely created by electrons, while clusters may originate from highly ionising particles. The event spread is homogeneous across the

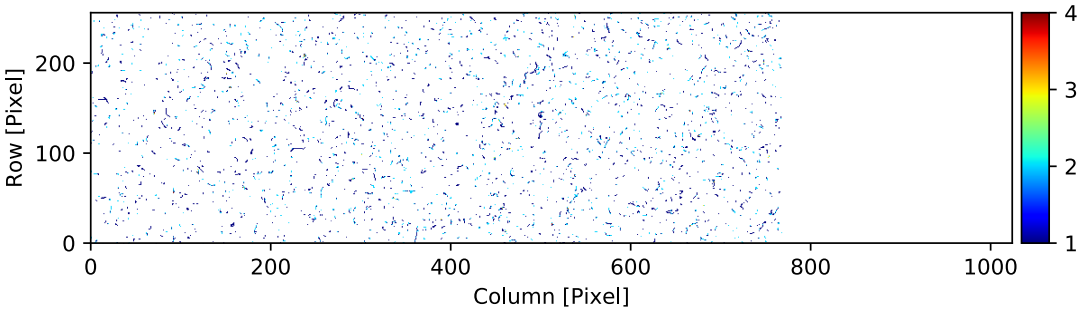

(a) Without high voltage

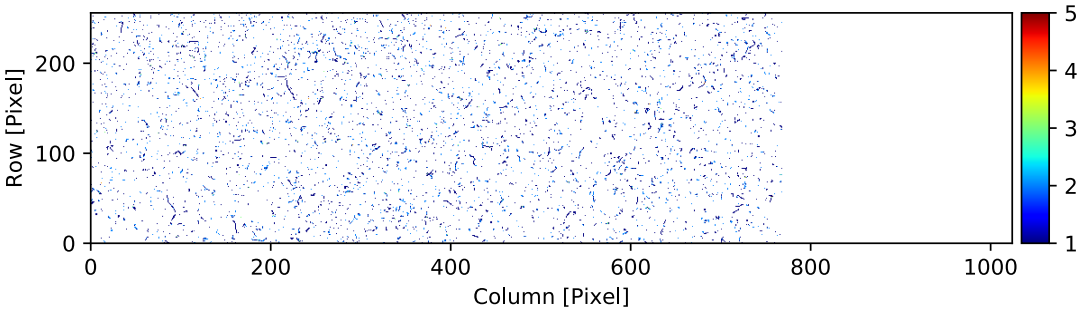

(b) With high voltage (−20 kV)

Figure 5.9: Count-images of the background without the PS beam. These were obtained with an integration time of two seconds. The last quarter of the image is blank because chip four was not working during this acquisition.

detection surface. Both cases, with and without the high voltage, are visually similar. Their event rate of ≈ 5 kHz is negligible in comparison with the ≈ 60 MHz signal expected from the PS beam. For the case with high voltage, the event rate ($\approx$ 1.5 kHz/TPX3) is slightly higher than without it ($\approx$ 1.2 kHz/TPX3). The increased rate with high voltage is explained by the deflection of charged particles toward the detector by the electric field; which would otherwise miss the detector or not have enough energy to create an event.

In the presence of the PS beam, the background becomes more interesting. Depending on the beam characteristics and the operation performed on it, beam loss may be rare or in such number that the detector is completely saturated. Examples of beam loss at different times during a single PS cycle are presented in Figure 5.10.

The characteristic *tracks* made by the beam loss (protons) in the sensor are clearly visible, as well as curly tracks, heavy tracks and small clusters, which are are typically caused by electrons, heavy ions and alpha particle respectively [99, 100]. These are presented in Figure 5.11.

Besides their shape, the most noticeable difference with the case with no beam is the event rate. The event rate can fluctuate between a few kHz per chip to a few MHz per chip, making it potentially comparable to the expected beam signal. In hindsight, beam losses are relatively rare with the LHC type beams. They mostly occur during the beam injection and manipulations, which only account for a fraction of the cycle time.

The time over threshold distributions for the three measured cases are presented in Figure 5.12. This type of distribution is presenting the relative energy deposition of the events for a given data-set. The distributions are normalised to their area in order to be compared. All distributions are qualitatively similar to a landau distribution for Minimum Ionising Particles (MIP) [101]. The three distributions have their main peak at ≈ 25 TOT, except for the case with high voltage, which has a secondary peak at a lower TOT. This secondary peak — when combined with the higher event rate — reveals an effect of the instrument high voltage on the signal measured by the detector. One possibility to explain this peak, is the fact that light particles from the background are deflected toward the detector by the instrument electric field.

The background signal presented in this section is considered noise in the profile measurement and must, therefore, be mitigated. The methods applied to reduce its impact on the measurement are presented in Chapter 6.

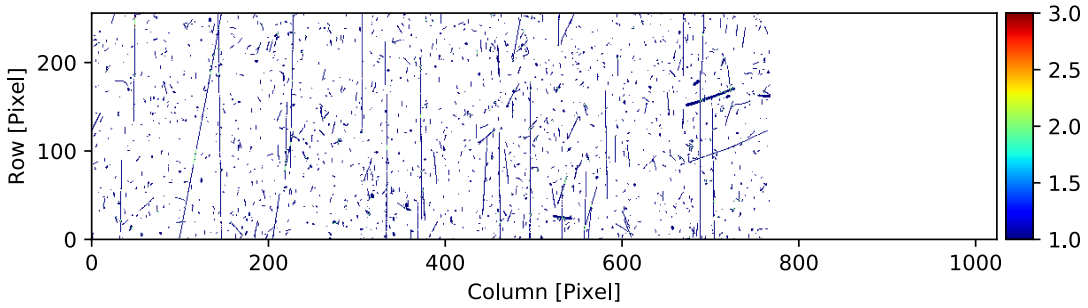

(a) Medium intensity beam loss during the beam acceleration.

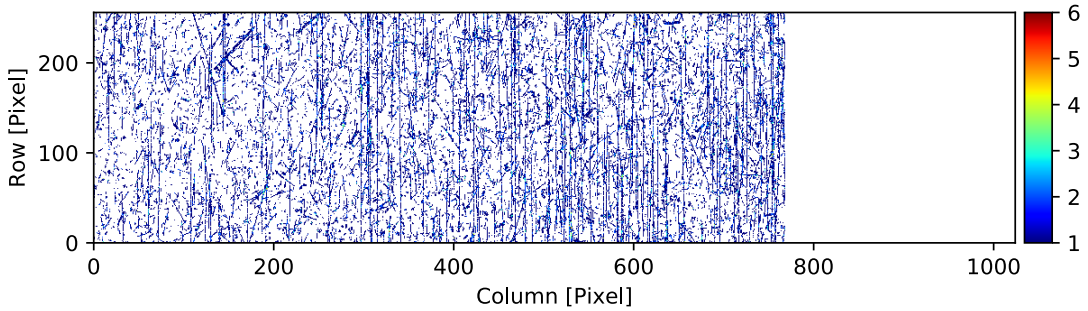

(b) High intensity beam loss at the beam injection.

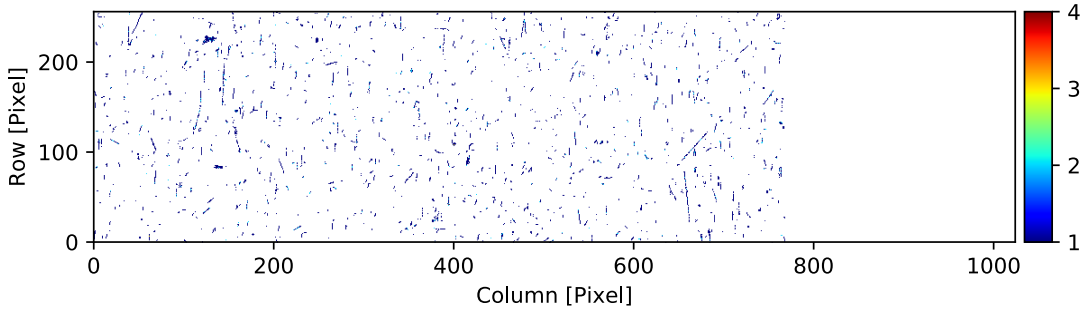

(c) Low intensity beam loss moments before the beam extraction.

Figure 5.10: Count images for different intensity of beam loss for a 1 ms integration time with a nominal LHC beam. The beam loss intensity depends of the type of beam circulating in the PS and the operation performed on the beam (e.g. injection, bunch splitting, transition crossing etc...).

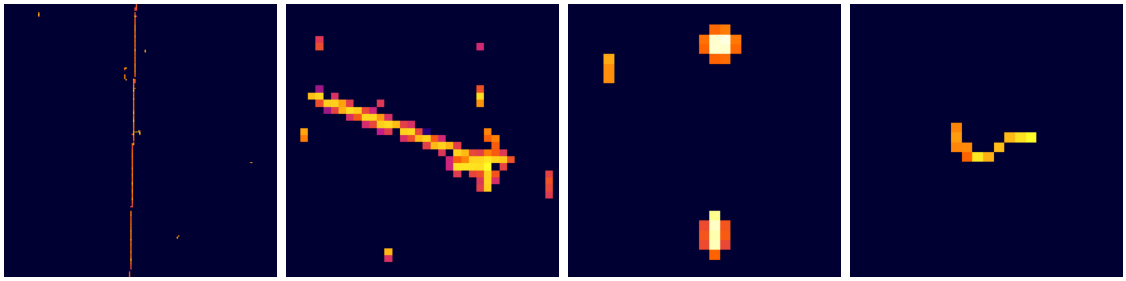

(a) Beam loss track. (b) Heavy track. (c) Small clusters. (d) Curly track.

Figure 5.11: Example of different types of background signal detected by the Timepix3. These are image captures from the readout system software.

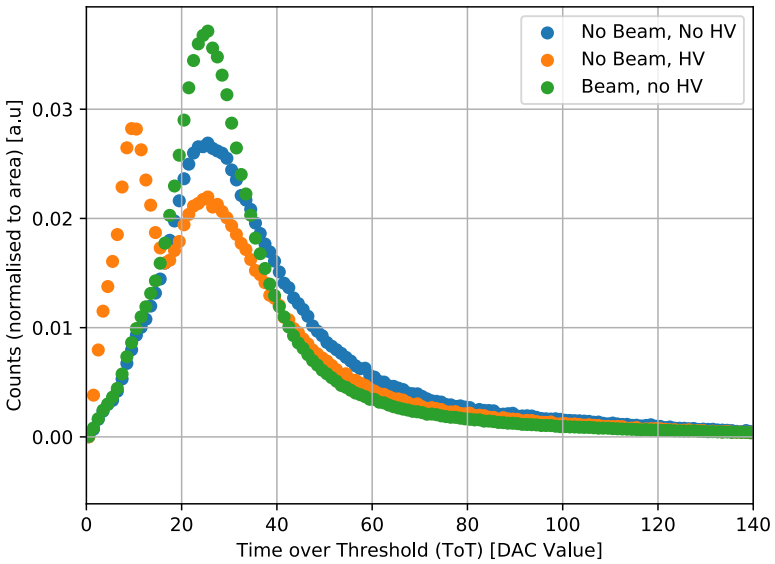

Figure 5.12: Distribution of the time over threshold for the background measurements. The abscissa is limited to 140 (out of 1023) for better visibility.

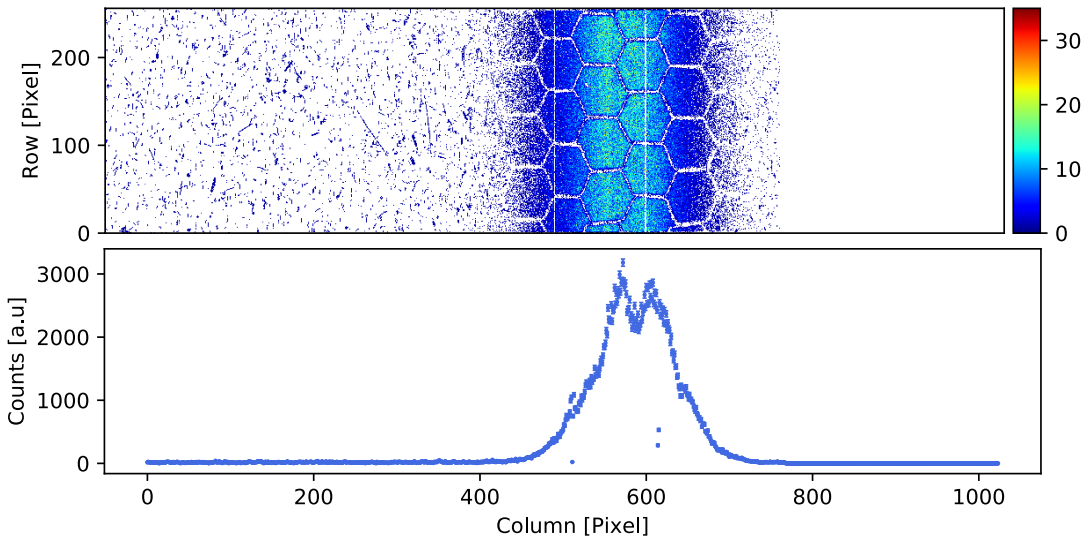

Figure 5.13: Count-image and count-histogram of the beam for a LHC type beam with a 100 ms integration time.

5.4.2 Detection of ionisation electrons

The detection of ionisation-electrons was tested a few days after the background measurements. The instrument was set to its nominal working point with the cathode voltage at −20 kV and the magnetic field at 0.2 T. The beam targeted by the measurement was a standard LHC25 cycle. This was considered an optimal candidate due to the small expected beam size, high intensity and low beam loss. The count-image and count-histogram for several time intervals of a single cycle are shown in Figure 5.13. A count-histogram is the sum of counts per columns. It gives the event distribution along the transverse beam dimension and is the base for the profile measurement with the instrument.

The image and histogram reveal a large number of events clustered within the distinct shape of the beam. These are not visible in the absence of the high voltage. The sharp shadow caused by the steel honeycomb is also visible. These are evidence that the particles creating the events seen in the cluster are negatively charged and originate from the beam or a process related to it. Moreover, to leave such a sharp shadow, the events must be directed at the detector with a relatively straight trajectory, and they do not have the energy required to go through the honeycomb walls.

In Figure 5.14, the time over threshold distribution for the data presented in Figure 5.13 is compared to the distribution of the unnormalised background signal from Figure 5.12. Similarly to what is observed with the background, the distribution shows a large

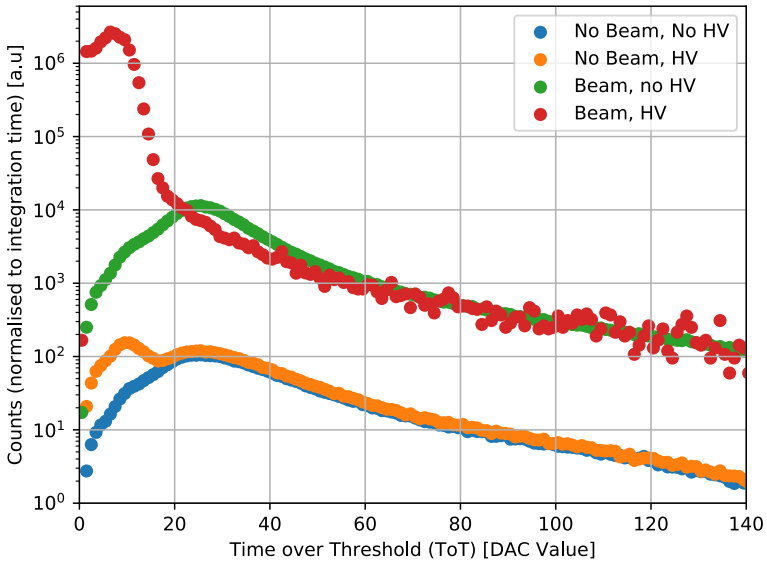

Figure 5.14: Distribution of the time over threshold for the beam and background measurements. The abscissa is limited to 140 (out of 1023) for better visibility.

excess of events with a low TOT when the instrument high voltage is turned-on compared to when it is turned off. This excess is qualitatively consistent with the signal of 10 keV electrons, which is lower than the expected energy deposition of Minimum Ionising Particles (MIP) in silicon (26 keV). The difference when the beam is introduced is the much more significant event rate observed with the beam than without it. This is to be expected from the ionisation-electrons generated by the beam in the instrument.

This evidence is sufficient to conclude that the PS-BGI is detecting the beam ionisation electrons. This was a significant milestone in the PS-BGI project as it validated that the detector was able to detect the ionisation electron signal and to operate in the PS environment. These results were presented in [102].

5.5 Detector limitations and difficulties of operation

During the weeks/months following the instrument installation, many of its limitations were discovered. This instrument is considered a prototype. It is, therefore, normal to identify its limitations in order to correct for them in the future.

5.5.1 Temperature limitations

The current implementation of the cooling system is insufficient to maintain a stable detector temperature during data acquisition. This implies that the detector can only sustain data acquisition for a few seconds per PS super-cycle (≈30 s), preventing the continuous monitoring of the beam profile.

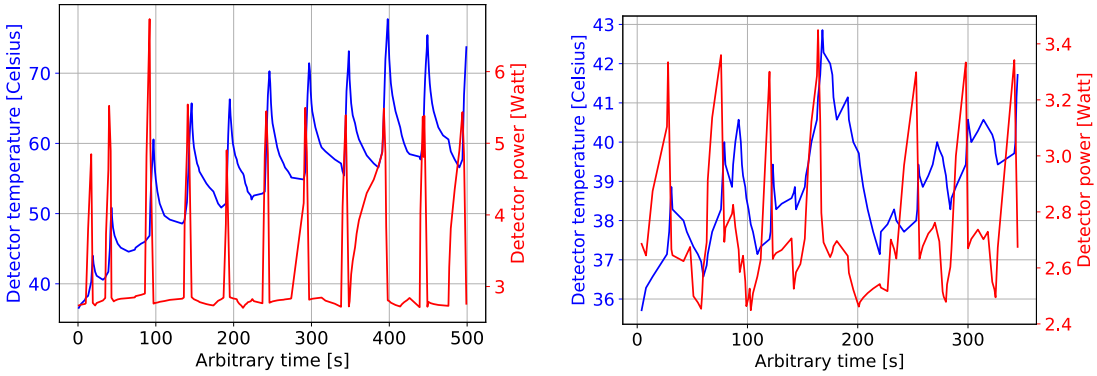

(a) Standard power mode.

(b) Low-power mode.

Figure 5.15: Detector power and temperature during data acquisition in standard and low-power mode.

In order to mitigate this problem, the Timepix3 are set in a particular low-power mode. In this state, the detector requires much less power (≈1.1 W/chip) when acquiring data than with its standard settings (≈2 W/chip). The improvement given by the low-power mode is visible in Figure 5.15, where the detector temperature and power are presented during data-acquisition for both power modes.

Each spike in the detector power corresponds to one data-acquisition per PS super-cycle. In the standard power mode, the temperature rises with each acquisition from 35 °C to 58 °C. The amplitude of the temperature variations caused by an acquisition are up to 20 °C. In the low-power mode, the temperature slowly rise from 36 °C to 42 °C due to the continuous series of data-acquisition. The temperature spikes caused by data-acquisitions are only in the order of a few degrees.

The workaround offered by the low-power mode only extends the time the detector can acquire data and does not solve the problem. Moreover, the low-power mode comes at the cost of increasing the TOA jitter and reducing the Timepix3 detection efficiency. This situation will be addressed in a future update of the instrument cooling system.

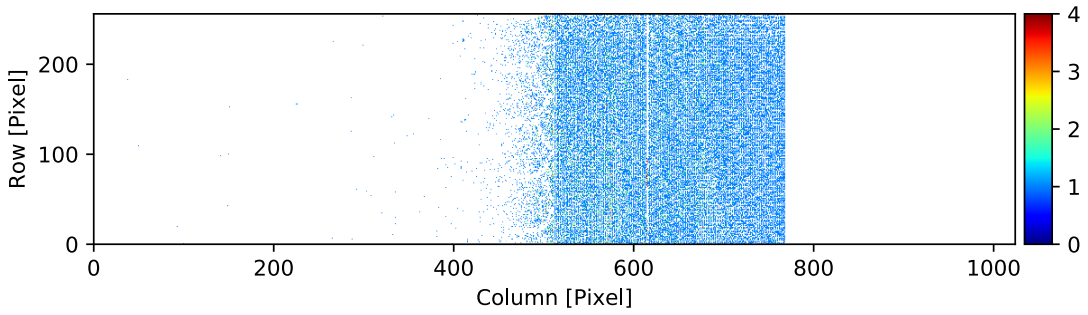

Figure 5.16: Count-image of a power glitch on chip three during data acquisition of a LHC type beam.

5.5.2 Chip four failure

Shortly after the installation of the PS-BGI, the control of chip four was lost. One or several important control signals appeared to be disconnected, causing the chip not to follow the commands of the readout system. No attempt to remotely recover control of chip four worked (e.g. manually toggling control signals, power cycling). Since at the time of writing, the detector is still installed in the PS, no conclusion on the reason for its failure is available. For this reason, most of the data presented in this thesis is lacking chip four. It is however important to notice that the beam is usually not over chip four, thus this failure is only a limited problem.

5.5.3 Power glitch

Power glitches are instances where almost the totality of the Timepix3 is triggered at the same time for no apparent reason. These can last for a few milliseconds and can even affect other chips on the detector. Figure 5.16 presents an example where the edge of the beam is visible in chip two, but chip three is entirely saturated.

Power glitches are problematic since they render useless a significant fraction of the detection area; and the large number of events generated may lead to a readout saturation. These cannot be prevented and happen with no warning. The only mitigation available is to truncate the section of the data-set where the glitch happened.

Our best hypothesis for the cause of the power glitches is a sudden drop in the chips supply voltages caused by a high current spike. Such spike may be caused by the sudden power demand of the pixel matrix. If it is confirmed, the solution to this problem will most likely be an upgrade of the power distribution scheme of the detector.

5.5.4 Beam loss effects

In addition to the noise caused on the profile measurement, certain lossy beams may also force a Timepix3 to reset or enter a state requiring a reset. The only way to recover from it is to power cycle the detector and to perform a complete reconfiguration of the chip.

This effect is problematic when the beam causing the problem is cycling with the PS supercycle, resetting the PS-BGI every ≈30 s; effectively rendering the PS-BGI inoperable. This problem has only been observed during *machine development* time, where new beams or equipment are tested, and not during the normal operation of the PS.

There is no clear explanation for this issue. One possibility is that the Timepix3 reset is caused by a single event upset or that the ceramic capacitors on the chip carrier are affected by the beam loss.

The only mitigation envisaged so far is to fully automatise the set-up procedure of the detector, allowing it to recover in a few seconds rather than a few minutes. This issue will be investigated further at the restart of the PS in 2020.

5.6 Summary

This chapter presents the assembly and installation of the PS-BGI in the PS. The methods for the Timepix3 equalisation and noisy pixel removal are introduced. The equalisation allows to get a more stable detector; while improving the measurement quality.

The background seen at the instrument location is evaluated. Most of it comes in the form of beam loss of various intensity. The signal induced by this background is potentially comparable to the ionisation-electron signal; which could affect the quality of the instrument profile measurements. Removal of the background is addressed in the next chapter. The instrument is able to detect ionisation-electron signal and measure a beam profile. However, several issues render the utilisation of the instrument difficult, which will be addressed in the next version of the instrument design.

Chapter 6

Analysis of the detector data

The goal of the PS-BGI is to measure the width of the LHC-type beams. This information is carried to the instrument by ionisation-electrons generated by the beam rest-gas interaction. However, the data measured by the instrument is a blend of the ionisation-electrons and the beam loss background. Only the signal from the ionisation-electron is useful to measure the beam width, the background contribution is therefore removed in post-processing. The instrument records data in the form of an unsorted list of Timepix3 events. We refer to this list of events as a *data-set*. A data-set which has not gone through any post-processing steps is a *raw data-set*. An overview of the complete data post-processing is given in Section 6.1. The method to remove the background is detailed in Sections 6.2 and 6.3. The method to extract the beam width from the background-free data-set is presented in Section 6.4.

6.1 Post processing overview

During a typical data acquisition, the instrument records events — regardless of their origin — for the totality of the PS cycle or part of it. The resulting raw data-set is then stored in the back-end computer, to await offline processing. The data processing is split into three steps: cleaning, filtering and profile reconstruction. Figure 6.1 summarises the data processing.

The cleaning step aims at removing events which do not originate from ionisation radiation and to re-order the data-set in time. The filtering step removes events which do not originate from the beam ionisation-electrons. This is done by two independent filters, the cluster filter and time over threshold filter. The profile reconstruction uses the now

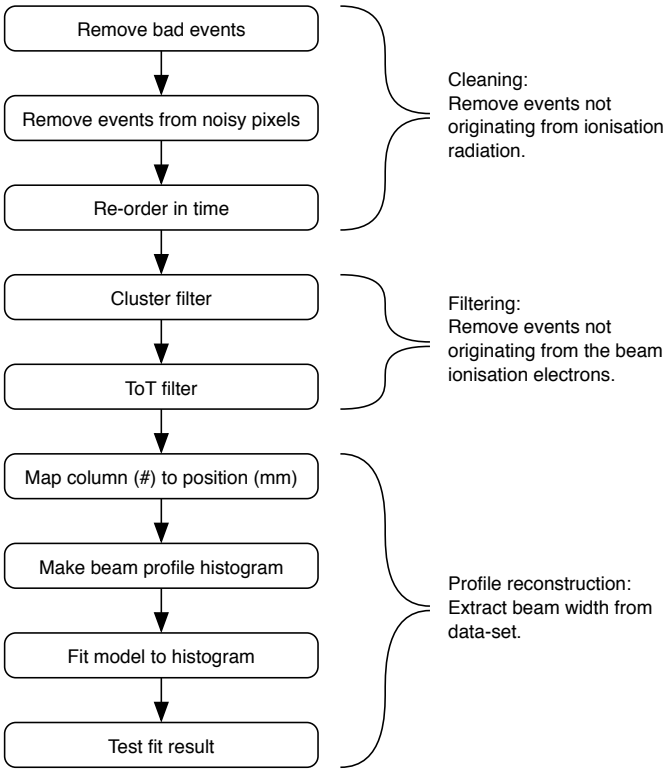

Figure 6.1: Flow-chart of the data processing for the PS-BGI.

background-free data-set to create a count-histogram. This histogram is the ionisation-electron distribution measured by the instrument. A model accounting for the detector imperfections is then fitted to this histogram. The fit result is tested with a Chi-squared test. If the model passes the test, its parameter corresponding to the beam width is taken as the measurement result.

6.2 Data cleaning

Raw data-set recorded during an acquisition might include the following:

- duplicated-events,
- events with physically impossible values,
- events from noisy pixels.

Duplicated-events and events with physically impossible value originate from errors in the readout system that have yet to be corrected. Noisy pixels are masked prior to an acquisition but the large temperature swing sustained by the detector during operation

causes the noise floor to rise. This leads some valid pixels to become noisy during the operation and thus generate events.

These are events which do not originate from ionising radiation. They are therefore systematically removed from any data-set. Simple comparisons and testing spot the duplicated-events and events with impossible values (e.g. if the row is superior to 256, the event is rejected). While the method presented in Chapter 5 tags and removes events with noisy pixels.

The readout system does not guaranty the temporal ordering of the events However, the cluster filter — presented below — relies on a data-set ordered in time. The events are therefore sorted incrementally, based on their time-stamp. The algorithm Quick-sort [103] performs this sorting step. At this point, the data-set is considered clean. Further filtering steps, detailed in the next sections, are then used to select the ionisation-electron signal and from the various backgrounds.

6.3 Data filtering

The data filtering aims to remove the background events from the data-set. Two complementary methods are used for this purpose; the cluster filter and the time over threshold filter.

6.3.1 Cluster filter

The cluster filter is the combination of a clustering algorithm and a filter which removes clusters outside a certain size-range from the data-set. In the context of the PS-BGI, we define a cluster as a group of events originating from the same incident particle. The cluster size is the number of events comprising it; clustering is the action of identifying these groups of events.

Chapter 5 introduces, the background signal from the beam and activated materials. One can easily see that it is composed of straight tracks, curly tracks, blobs, and so on; while the ionisation-electrons appear to generate mostly single events. The role of the cluster filter is thus to tag and remove the background signal associated with this type of large clusters.

The current state of the art method to perform clustering on pixel detector data is to use deep learning [104]. Deep learning is a method where an artificial neural network

is trained to recognise specific patterns in the input data. A trained neural network is, in principle, able to split clusters and their individual constituents (e.g. two tracks crossing, a track and incident delta-ray). The main difficulty in implementing such method is to provide the training data-set. This data-set has to contain examples of inputs and their expected outputs; while being large enough to train the artificial neural network properly.

Training data-sets are typically obtained from a complete simulation of the instrument or from a science crowd-sourcing campaign. The former is feasible using a combination of simulation tools such as Geant4 [105], IPMSIM and AllPix Squared [106]. While the later would require to already dispose of a substantial data-set from the PS-BGI and to be able to reach a large number of people.

On the other hand, a traditional clustering algorithm such as the one presented below can provide a crude clustering (e.g. find cluster, shape and size, no identification of the individual constituents) for virtually no setup cost. As said above, the cluster filtering is based on the cluster size only and does not require an understanding on the type of particle involved in creating the clusters. For this reason there is no advantage in using the deep-learning approach for the PS-BGI data clustering. The traditional approach is therefore preferred.

6.3.1.1 Clustering algorithm

Since there is no openly available clustering algorithm for Timepix3 data-sets, a custom clustering algorithm was designed for the PS-BGI. This algorithm takes advantage of both the spatial and temporal information available in the Timepix3 data. Figure 6.2 presents a simplified flow-chart of the algorithm.

At its core, the algorithm looks at each event in the data-set. If the current event is not already attributed to a cluster, it starts a recursive cluster search. The recursive search defines the current event as a reference, and a new cluster is created with it. It then searches for events which are close in space and time to this reference. These are added to the current cluster. Each of the events newly added to the cluster is then used as the reference and the search is repeated. This process continues until no new event satisfies the space and time criteria. The clustering is complete once all events have been attributed to a cluster. In this context, single events are attributed to a cluster of size one.

The use of space and time criteria to identify clusters is motivated from the fact that

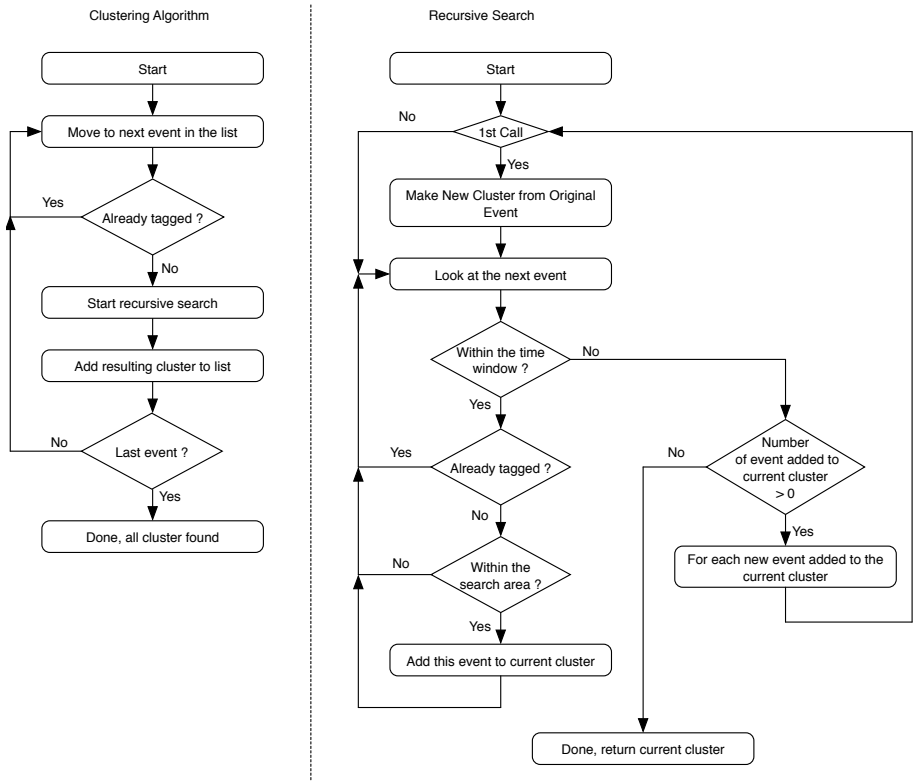

Figure 6.2: Flow-chart of the clustering algorithm and recursive search.

the path and energy deposition of an incident particle in a silicon sensor are continuous. Thus, events originating from the same incident particle should be neighbouring each-others. For this reason, the default space criterion is set to a radius of one pixel around the reference pixel. Moreover, with respect to the Timepix3 time reference (360 MHz), the duration of the energy deposition of an incident particle appears instantaneous. The time of arrival of events originating from the same incident particle should, therefore, be close to each-other. The default time criterion is set to 15 ns after the reference pixel. This value accounts for the drift time of the charge in the sensor (<10 ns), and the various delays in the Timepix3 (e.g. time-walk, fast oscillator start-up time). These values were fine-tuned — after trials and errors — to provide the best clustering result with most data-sets. In some cases increasing the space criterion and reducing the time criterion may improve the clustering result significantly.

Due to the absence of another algorithm to test the result of the clustering algorithm, small data-sets — <1000 events — were manually clustered in order to provide a comparison. The clustering algorithm was found to find all clusters, aside from extreme cases (e.g. very large beam loss, cluster happening exactly at the same time...).

6.3.1.2 Cluster filter

The cluster filter removes all clusters outside a user-defined range. By default, the filter is set to keep only clusters with a size inferior or equal to two. This default range is attributed to the ionisation-electron signal. It was determined empirically by comparing the count-images, histograms and TOT distributions obtained with different filtering ranges.

We showed in Chapter 5 that the presence or absence of events from the ionisation electrons is visible in the count images, histogram and TOT distribution. Therefore by examining these for different cluster size ranges, we can find at which cluster size ionisation electrons stop being present.

We demonstrate this by using a measurement taken with a BCMS beam. The original data-set is given to the cluster filter with the instruction to keep only clusters of size one, one to two and one to three. The clusters above these ranges are also conserved and correspond to the clusters of sizes two to infinity, three to infinity and four to infinity respectively.

The results are visible in Figures 6.3 and 6.4. Figure 6.3 presents the count-images for the original data-set, for the clusters of size one to two and for the clusters of size three to infinity. The count-image for the original data-set shows a mix between the beam ionisation-electron and the background. The count-image for the clusters of size one to two shows mostly the ionisation-electrons; while the count-image for the cluster of size three to infinity shows mostly the background. Only this case is presented as there is little visible difference with the other filtering ranges.

To better compare the different filtering ranges, Figure 6.4 shows the count histograms and time over threshold distributions for all ranges. The count histograms for the cluster size one, one to two and one to three clearly show the beam profile. There is a small amplitude difference between the histograms for the cluster of size one and one to two. This difference is also visible in the histograms for the clusters of sizes two to infinity and three to infinity.

The time over threshold distributions present the same result. The peak associated with the ionisation-electron signal is visible up to clusters of size two. Above this limit, the time over threshold distribution is qualitatively similar to the the distribution for the background.

These results indicate that most of the ionisation-electrons are single events (clusters of size one). Nonetheless, some are counted as clusters of size two. This might indicate

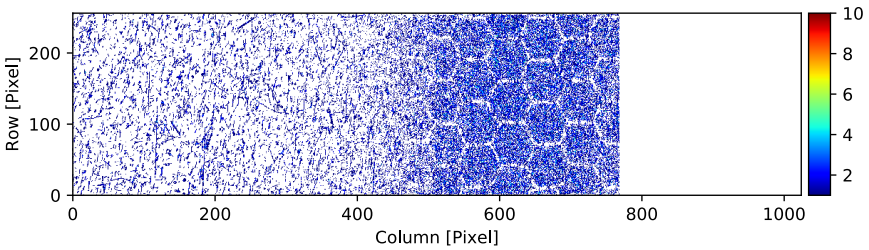

(a) Original data-set.

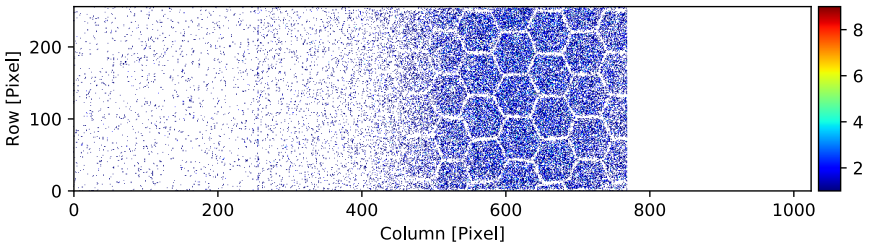

(b) Clusters of size zero to two.

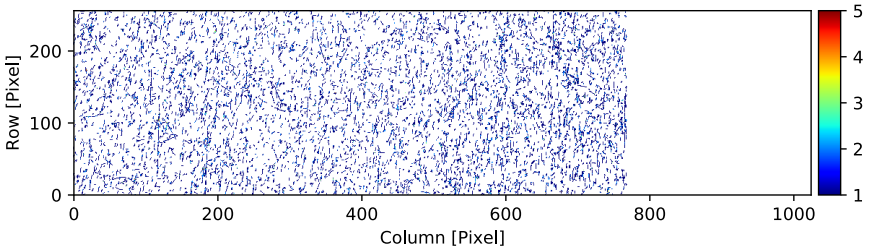

(c) Clusters of size three to infinity.

Figure 6.3: Count images for different cases of cluster filtering. The original data-set is a BCMS beam with 10 ms integration window.

that a small fraction of the ionisation-electrons are incorrectly counted as clusters of size two or that they have enough energy to trigger two pixels at once.

The former case is possible since two particles triggering two neighbouring pixels within the same TOA clock cycle would be indistinguishable from a cluster of size two. However, this scenario is unlikely due to the low production rate of ionisation-electron predicted in Chapter 2 and measured in Chapter 7.

The later case is more likely when comparing the charge an ionisation-electron deposits in the sensor to the charge required to trigger a single pixel. The Timepix3 can have a threshold as low as 500 e^-, while a 10 keV ionisation-electron produces more than 2500 electron-hole pairs in the sensor.

6.3.2 Time over threshold filtering

The cluster filter removes clusters too large to be associated with the ionisation-electrons. However, small clusters with a large time over threshold — which are incompatible with the ionisation-electron signal — are not filtered by this method. This issue is resolved by filtering the data-set given by the cluster filter based on the TOT of each event.

The ionisation-electron signal is associated with a low-TOT peak in the time over threshold distribution. The filtering-range is therefore adjusted to keep this peak while rejecting everything else. The exact limit between what is considered ionisation-electrons and background is adjusted based on the Timepix3 settings during the data acquisition. During data acquisition, the detector temperature may vary by more than 40 °C (see Chapter 5). This affects the Timepix3 noise floor and by extension, the emergence of new noisy pixels. As a consequence, the chips thresholds are constantly adjusted during operation. This has an impact on the TOT measured by the Timepix3 and therefore affects the location of the ionisation-electron peak in the TOT distribution. Depending on the conditions the cutoff limit is manually set between 15 and 30 [DAC value].

Figure 6.5 presents the result of the time over threshold filter on the data filtered by the cluster filter presented in Section 6.3.1. The TOT filter is applied with a cutoff value of 15. The effect of the filter is a visible decrease of the number of events across the surface of the detector, with little change to the beam profile shape or amplitude. The count histogram of the filtered-out data is homogeneous across the columns indicating that little to no ionisation-electrons events were removed.

This example shows that to remove the most background, both the cluster and TOT

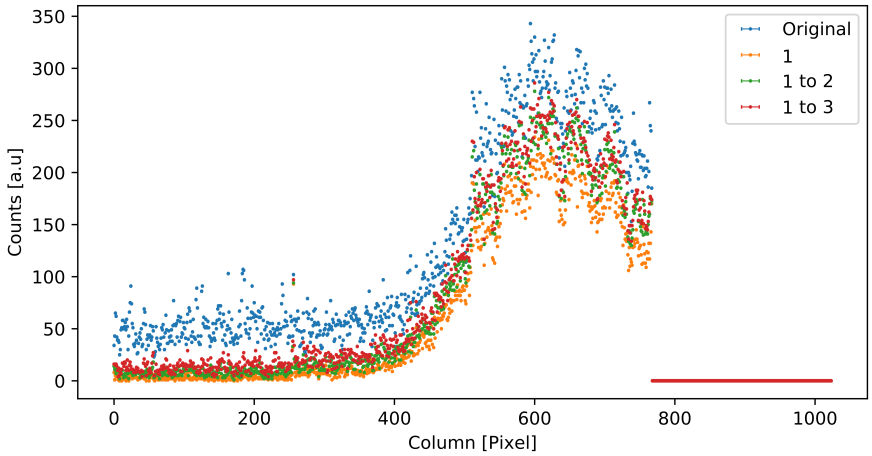

(a) Count histogram from the data kept by the cluster filter.

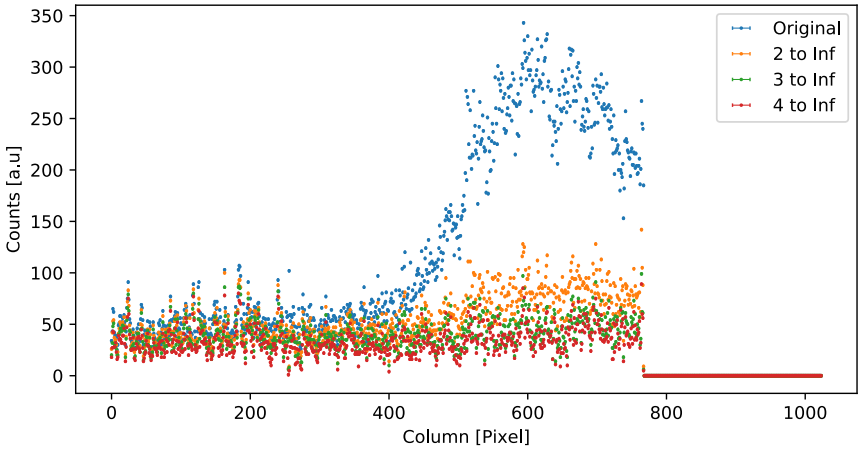

(b) Count histogram from the data rejected by the cluster filter

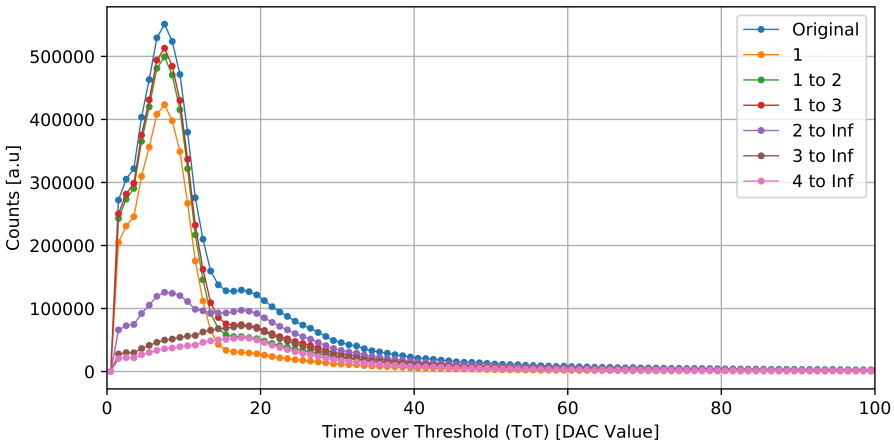

(c) Time over threshold for all cases of cluster filtering.

Figure 6.4: Count histograms and time over threshold distribution for different ranges of cluster filtering. The vertical error-bars are not displayed for clarity.

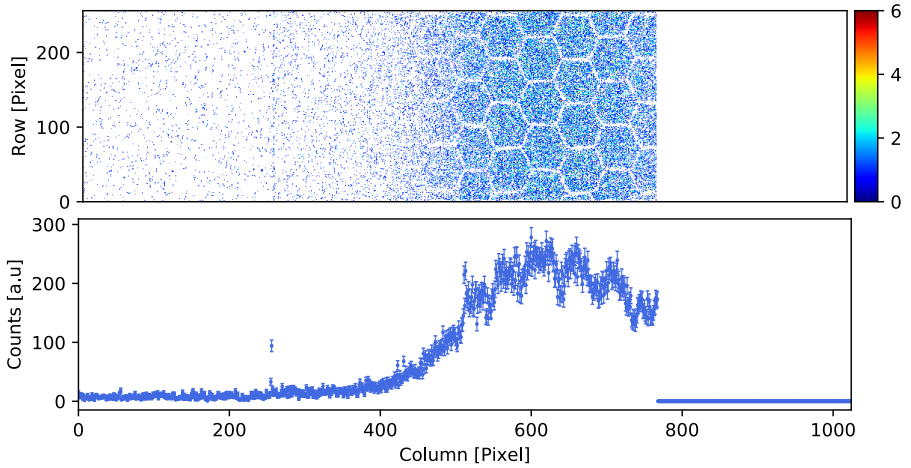

(a) Cluster filter only.

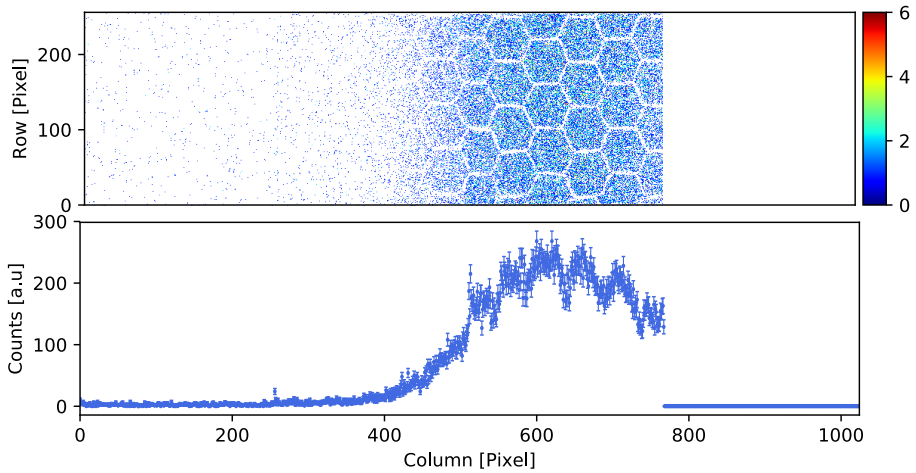

(b) Cluster filter followed by time over threshold filter.

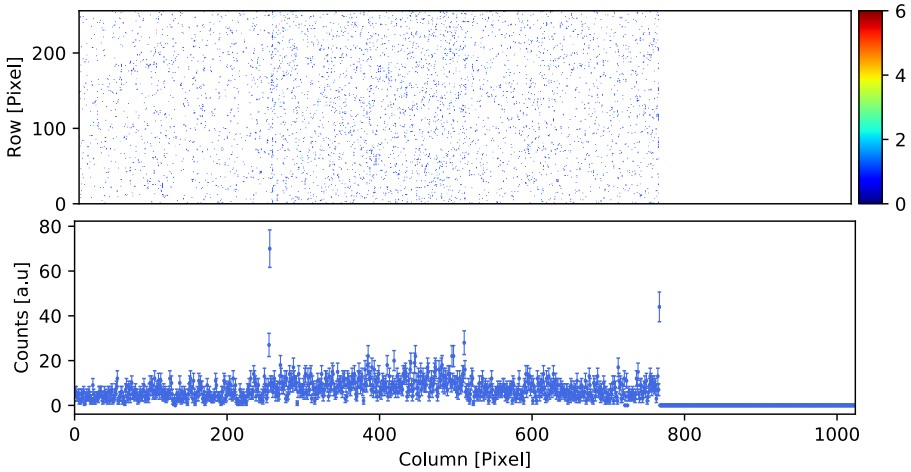

(c) Data removed by the TOT filter.

Figure 6.5: Count images and corresponding histograms for the result of the cluster filter, cluster filter and TOT filter. Noisy pixels at the edge of chip1/2 is causing the abnormally high bin in the histograms at column 255.

filters should be applied.

6.4 Profile reconstruction and beam size measurement

The profile reconstruction takes a filtered data-set and makes a count-histogram with it. This histogram is the transverse ionisation-electron distribution measured by the detector. During the transport of the ionisation electrons to the pixel detector, some of the electrons are stopped by the Faraday cage honeycomb. The amount of blocking is not same for each pixel detector column, implying that the distribution measured by the instrument is no longer the beam one. We refer to this effect as honeycomb masking. This issue is overcome by fitting the measured distribution to a model that takes into account the effect of the honeycomb masking.

To ensure that the model is a correct representation of the measured electron distribution, the result of the fit is tested with a Chi-squared goodness-of-fit test. If the result of the test is satisfactory, we consider the fitted model trustworthy, and the model parameter corresponding to the beam width is used as the instrument result. Additionally, the relative beam position is also used as it is included in the model.

6.4.1 Accounting for the chip position

Up until now we presented the count-histogram and count-images as if the four Timepix3 were a single large detection area. However, in reality there is a small gap and rotation between each of the chips, which can been seen in Figure 6.6.

To account for this, a new global Cartesian coordinate system is defined. The abscissa X and ordinate Z of this coordinate system are horizontally transverse to the beam trajectory and parallel to the beam trajectory respectively. The origin of the system is set to the bottom left corner of chip one and extends to the furthermost pixel of chip four. The position of each hybrid pixel detector is measured relative to chip one, using a microscope. Figure 6.6 gives the result of the measurement for the N-on-P chip carrier. This measurement allows us to know the gaps, rotation and misalignment between the chips and to know the position of each pixel in the global coordinate system.

An example of this position calibration is visible in Figure 6.7, where two histograms are presented with and without the position calibration. The gaps between chip one, two and three are visible in the second histogram.

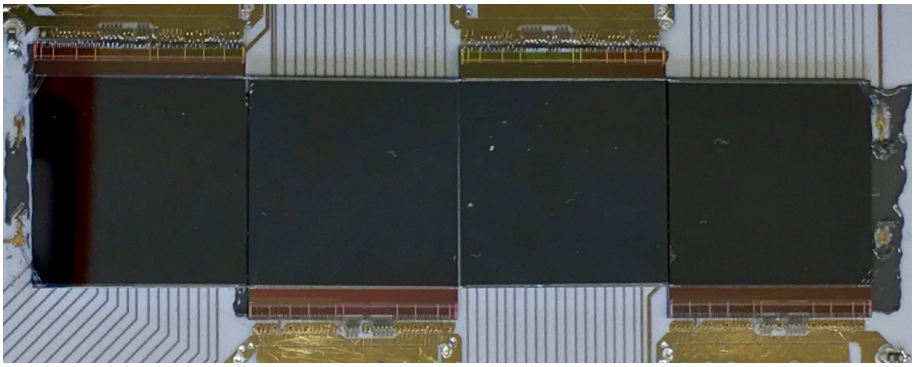

(a) Close view of the N-on-P chip carrier.

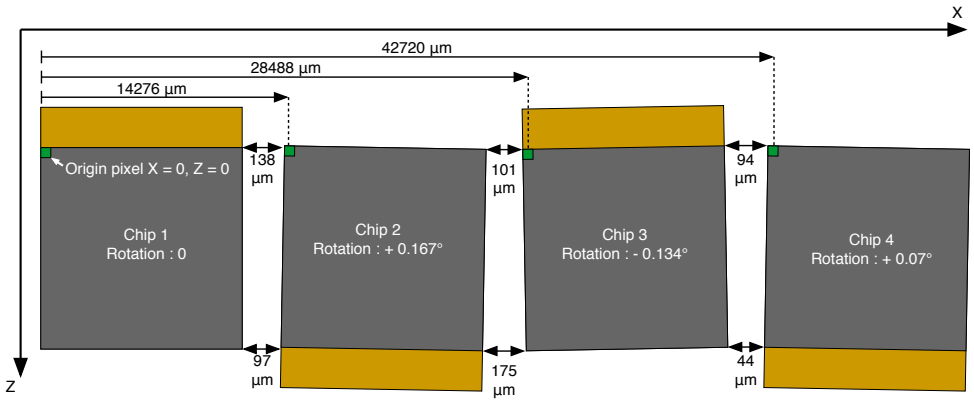

(b) Schematic representation of the chip placement.

Figure 6.6: Picture and schematic representation of the chip placement. The gap between the chip is clearly visible in Figure (a). The rotation and gaps represented in Figure (b) are not to scale.

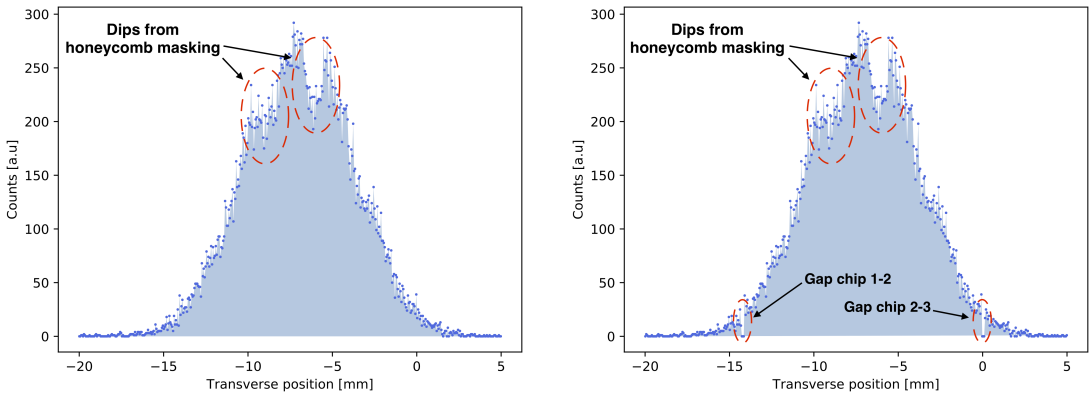

(a) Without position calibration.

(b) With position calibration.

Figure 6.7: Histograms created from the same data-set with and without the position calibration. The histograms area is coloured to highlight the gaps between chip one & two and two & three.

6.4.2 Accounting for the honeycomb

The effect of the honeycomb on the original ionisation-electron distribution is to block inhomogeneously some electrons in their transport to the detector. In turn, the detector does not measure the beam ionisation-electron distribution but a modified version of it. This effect is visible in the form of dips in any of the histograms presented thus far, such as in Figure 6.7.

6.4.2.1 The fit model

To account for the honeycomb masking, we decided to model the distribution measured by the instrument as a function representing the beam distribution multiplied by a transmission function. We make the assumption that the beam distribution follows a Gaussian function $g(x)$ such as

$$g(x) = ae^{-\frac{(x-\mu)^2}{2\sigma^2}}, \tag{6.1}$$

where x is the beam transverse dimension, a the profile amplitude, μ mean beam position, and σ the beam width. It is useful to note that homogeneously masking the distribution would only result in a change to a. The distribution measured by the instrument f_{psbgi} is therefore

$$f_{psbgi}(x) = g(x) \times t(x) \tag{6.2}$$

where $t(x)$ is the transmission function, returning a transmission efficiency from zero to one. For convenience we also include in the transmission function: the gaps between the pixel detector; missing chip and the noisy pixels masked in the Timepix3. These are represented with a transmission of zero.

6.4.2.2 Finding the transmission function

The transmission function $t(x)$ is derived from the integral of the honeycomb masking $m(x, z)$ along the beam direction z with

$$t(x) = 1 - \frac{\int_l^u m(x, z) \cdot dz}{u - l}, \tag{6.3}$$

where l is the lower edge of the detector and u is the upper edge of the detector. $m(x, z)$ is a function returning a value between zero and one, which represents the degree of masking for a given position in the XZ plane. A value of one corresponds to a complete masking

(no ionisation electron can be detected at this location).

The first attempt at estimating the honeycomb masking was made by using a perfect geometrical representation of the honeycomb. This method ultimately failed because this geometrical did not represent the irregularity and imperfections of the real honeycomb. Since, at this point, the instrument was already installed in the PS, the honeycomb mask - m(x,z) - is measured in-situ.

The measurement starts by making a count-image from a large data-set. In order to have substantial coverage of the detection area and to have sufficient statistics to reveal the masked area, this large data-set is the combination of multiple data-sets. The left half of chip one and the totality of chip four are not considered for the measurement. The former is explained by the fact that the beam is never present in this area of the detector, while the later is explained by the fact that chip four stopped working during commissioning and few data were ever recorded with it.

The count image obtained by this method is shown in Figure 6.8 (a). The honeycomb masking is visible in the count image as the zone where little to no counts were measured. Since the computer does not see this pattern as easily as we (humans) do, a specific method to determine which pixels are masked by the honeycomb was devised.

For each column in the image, the distribution of the counts along the rows is examined. Due to the shape of the honeycomb and to the fact that the beam moves along the columns, each pixel within a column is expected to measure a similar number of counts, except for those pixels masked by the honeycomb. An example is shown in Figure 6.8 (b), where the counts in column number 470 are presented as a function of the row number.

To determine which pixel is masked in each column, a threshold based on a fraction of the count-distribution mean is used. Pixels where the number of counts is below the threshold are considered masked. The distribution of the counts for column 470 is shown in Figure 6.8 (c), where the mean is presented as a black dashed line and the threshold is presented as a orange dashed line. These same mean and threshold are also presented in Figure 6.8 (b). One can see that most pixels have measured between 30 to 70 counts with a mean at 45, while the rest is below 30 counts. In this example, the threshold is set to 30 percent of the mean or 13 counts and 19 pixels are below the threshold.

The process is repeated for each column and the result is a map of the honeycomb masking $m(x, z)$ presented in Figure 6.8 (d). This map is binary, a one represents a masked

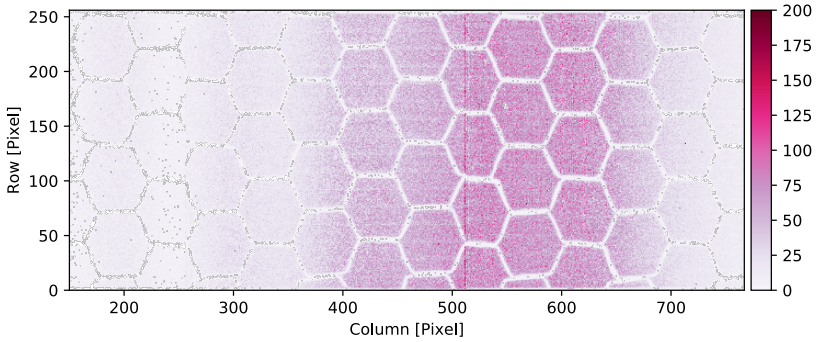

(a) Count image for the combined data-sets.

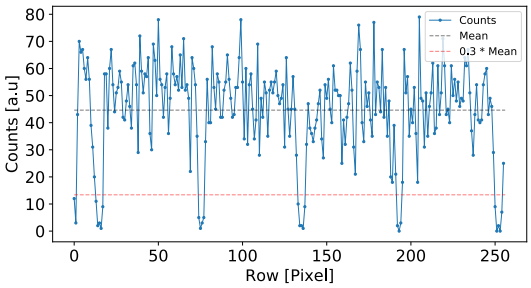

(b) Counts for the column 470.

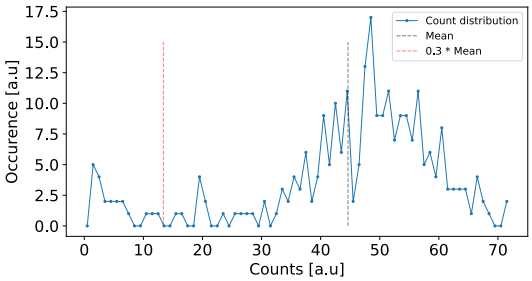

(c) Count distribution for the column 470.

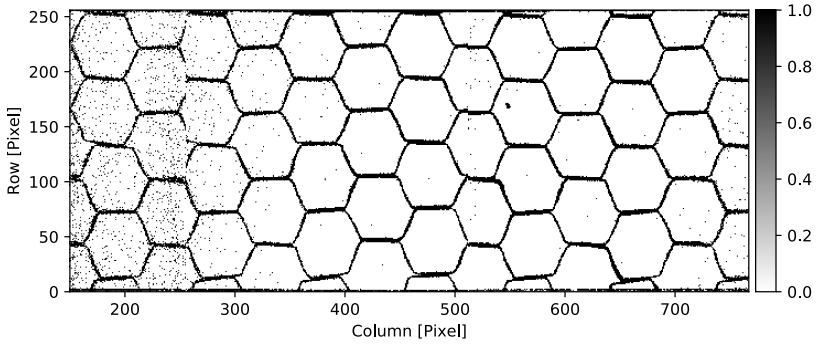

(d) Map of the masked pixels. Black pixels are masked.

Figure 6.8: The honeycomb masking is estimated from a long exposure to the beam. Pixels with a count much lower than that of the mean of the column are counted masked.

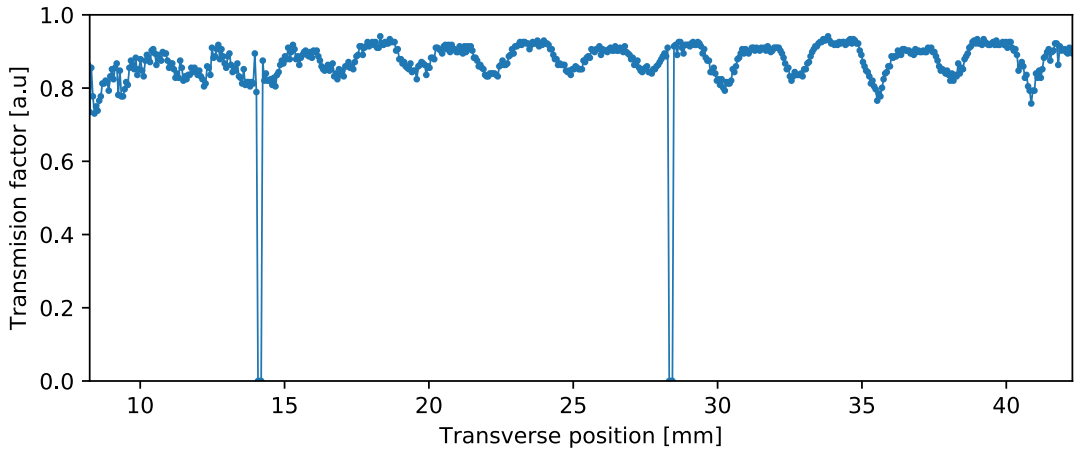

Figure 6.9: Transmission ratio as a function of the transverse position. The values where the transmission ratio is null are the gaps in between the Timepix3 chips. The transmission ratio for the positions above chip number four (>42 mm) is not shown since this chip was malfunctioning.

pixel, while a zero represent a non masked one.

The transmission for each column is then found by using Equation 6.3, which corresponds to take the ratio of non-masked pixel divided by the total number of pixels in each column. At this point, the correction accounting for the chip position presented in Section 6.4.1 is added, changing the X axis of the transmission from pixel to millimetre.The resulting transmission function is presented in Figure 6.9.

The transmission function fluctuates between 0.78 and 0.9, with an average of 0.87. The flat regions correspond to the area of the detector where the honeycomb faces are perpendicular to the beam trajectory; while the v-shaped dips correspond to the honeycomb faces oriented more parallel to the beam trajectory. The gaps between the chips are represented by the dips with a transmission of zero.

6.4.3 Fitting and goodness of fit test

The function f_{psbgi} is fitted to the calibrated count-histogram using the *curve_fit* function from the *SciPy* Python library [107]. This function uses the non-linear least square minimisation method. The maximum value, mean and standard deviation of the count-histogram are given as initial values for the α, μ and σ parameters respectively. The transmission function $t(x)$ is kept constant.

To verify the goodness of the fit, the Pearson's Chi-squared test is applied [108]. It

tests that an observation (e.g. the count-histogram) is consistent with a model (e.g. the fit of f_{psbgi}). For the test to be valid, the minimum number of counts per bin has to be greater than four [109]. The test is conducted with the following steps:

1. Calculate the Chi-squared statistic value.
2. Define the Number of Degree of Freedom (NDF).
3. Select a significance level α for the result of the test.
4. Get the p value corresponding to the test statistic result and the NDF.
5. Compare the p value with the confidence level, if p $>\alpha$ the test passes.

The Chi-squared test statistic is calculated using

$$\chi^2 = \sum_{i=1}^{n} \frac{(O_i - E_i)^2}{E_i}, \tag{6.4}$$

where O_i is the value of bin i of the count-histogram and E_i the expected value from the fitted model. A perfect fit would have a χ^2 of one. The expected values are calculated with

$$E_i = N \cdot (CDF_{psbgi}(i_u) - CDF_{psbgi}(i_l)) \tag{6.5}$$

with N the total number of counts in the histogram, CDF_{psbgi} the cumulative distribution function of f_{psbgi}, i_u the upper edge of bin i and i_l the lower edge of bin i. The Number of Degree of Freedom (NDF) is calculated by subtracting the number of non-null bins in the count-histogram by the number of fit variables plus one (3 + 1).

The significance level α is the limit from which we say that there is a significant deviation between our model and the data. If $p > \alpha$ we conclude that our model is consistent with the data. For all fit presented in this document α is set to 0.05 (95%). The p value is obtained from the chi-squared survival function SF_{χ^2} with

$$p = SF_{\chi^2}(\chi^2, NDF), \tag{6.6}$$

where χ^2 is the result of the test statistic of Equation 6.4.

6.4.4 Profile reconstruction result

Figure 6.10 presents the result of the profile reconstruction. The data-set from a BCMS beam at extraction is cleaned, filtered and integrated to form a count-histogram for a 5 ms period. The parameters for the model, f_{psbgi}, which best describe the count-histogram are then found by non-linear least squares minimisation. For comparison, the same count-histogram is fitted to a Gaussian function. The histogram parameters, fit and Chi-square results are given in the text-box in the top left corner of each plot. P0 correspond to a of $g(x)$, P1 corresponds to μ of $g(x)$, and P2 corresponds of σ of $g(x)$. All values are in millimetres.

In both plots the $g(x)$ function is referred to as the beam profile. Visually the fit of f_{psbgi} is following the electron distribution better than the simple Gaussian function. Moreover, it passes the test with a p value of 0.09 (9 %); while the simple Gaussian function fails (p <1 %).

6.5 Summary

In this chapter we present the method used to remove all non ionisation-electron events from raw data-sets. This method is based on a succession of filters, which remove events with characteristics that do not match those of the ionisation-electrons.

We further introduced the method used to extract the beam width from a filtered data-set. Due to imperfections in the detector assembly and the presence of the faraday cage honeycomb, the ionisation-electron distribution measured is not the original one. The original beam profile distribution is reconstructed using a model that accounts for the effects of the honeycomb and the physical gaps between the chips. The beam width is then determined by a fit of this model to the data.

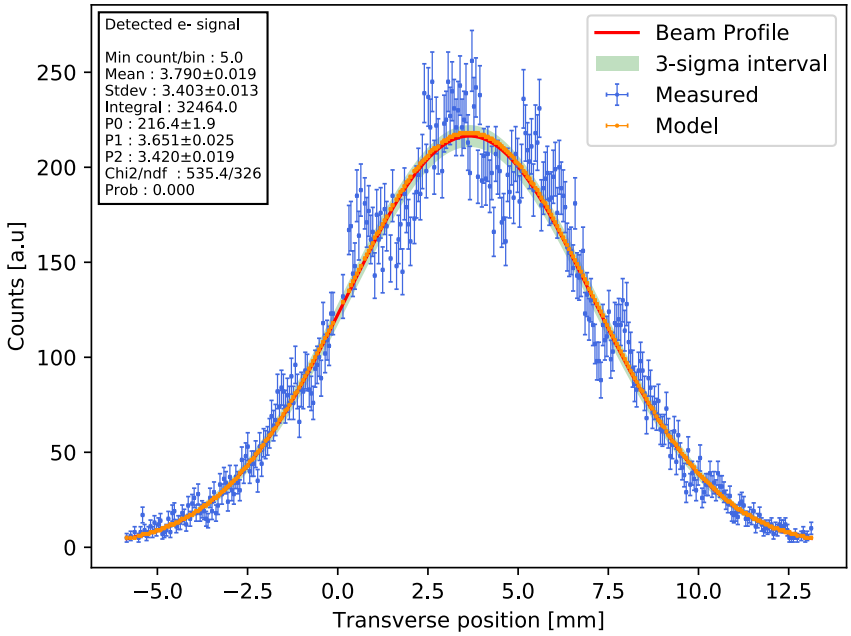

(a) Fit of $g(x)$.

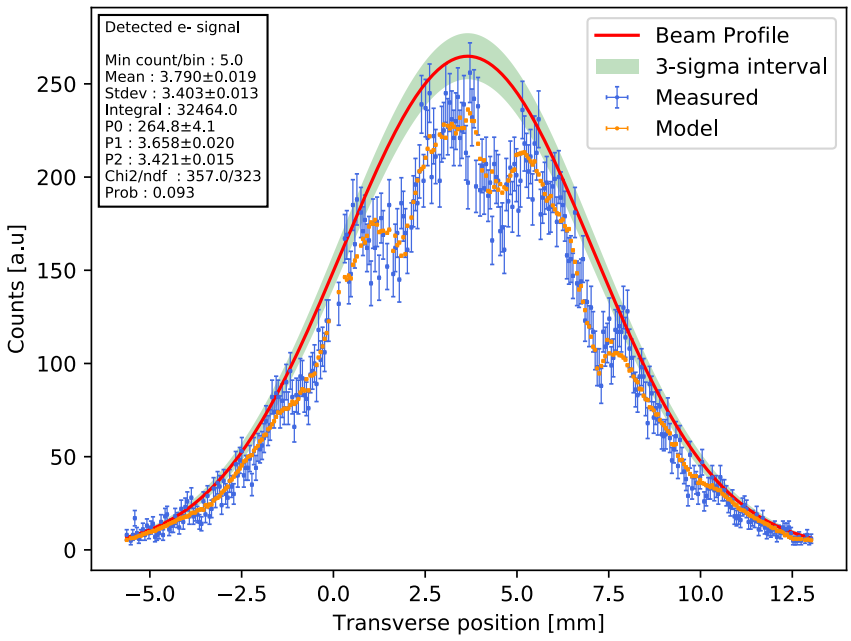

(b) Fit of f_{psbgi}.

Figure 6.10: Count-histogram (blue), expected values (orange), and the reconstructed beam profile $g(x)$ (red) with a three sigma interval (green). The expected value vertical error-bars are not displayed for clarity reasons.

Chapter 7

Beam profile measurements and instrument performance

This chapter demonstrates the novel capabilities of the PS-BGI by presenting the first time-resolved measurements of the transverse profile of the LHC-types beam in the PS. Section 7.1 introduces examples of single profile measurements, time-resolved measurements and the first estimate of the instrument precision. Section 7.2 explores the impact of the PS-BGI parameters such as the cathode high-voltage, the Timepix3 sensor bias-voltage and magnetic field strength on the measured event-rate and profile measurement. These are contrasted with the simulation presented in Chapter 2. The time-resolution of the detector is demonstrated in Section 7.1.3, hinting at possible performance improvements. Finally, Section 7.4 presents the results of a comparison between the PS-BGI and two other instruments installed in the PS, the Beam Position Monitor (BPM) [110] and the Wire-Scanner (WS).

7.1 Beam profile measurements

In order to test the PS-BGI, the LHC-type beams — BCMS and nominal LHC — were measured during the second run of the LHC. Examples of single profile measurements and time-resolved measurement are presented below. The instrument precision is then evaluated.

Table 7.1: Expected and measured beam size for the Nominal LHC and BCMS beam at flat-bottom and flat-top. The expected values are taken from table 2.1.

	Nominal LHC		BCMS	
	flat-bottom	flat-top	flat-bottom	flat-top
Expected	3.7 mm	1.14 mm	2.69 mm	0.81 mm
Measured	5.63 ± 0.07 mm	1.17 ± 0.01 mm	3.44 ± 0.04 mm	0.90 ± 0.01 mm

7.1.1 Single profile measurements

Figures 7.1 and 7.2 present single profiles measured from BCMS and LHC beams. Both the profiles at flat-bottom and flat-top are shown. These were acquired from the same cycle, with an integration window of 1 ms. The measured profile is presented in blue in the main plot, the model from the fit is presented in orange and the reconstructed beam profile in red. An error interval (3σ) for the reconstructed beam profile is shown in green. The standardised difference of the residuals is shown in a secondary plot.

These measurements demonstrate the capacity of the PS-BGI to measure both LHC-type beams at injection and extraction. The measured beam width at flat-bottom and flat-top for the nominal LHC and BCMS beams are presented in Table 7.1. For both beam types, the values measured at extraction are consistent with the values predicted in Chapter 2. However, the values measured at injection are larger than predicted by 52 % and 28 % for the nominal LHC and BCMS respectively. This has been observed on all LHC-type beam measured by the instrument.

There is no obvious reason for this discrepancy, the instrument was working as intended and the beam effects were all suppressed by the presence of the magnetic field. The values used in Chapter 2 were all taken from the latest beam and PS lattice documentation. Nonetheless, it should be noted that measuring the beam size at flat-bottom has been more difficult than anticipated due to the large beam loss produced by the injection and the fact that the beam is not perfectly stable in this part of the cycle.

7.1.2 Time-resolved profile measurements

Time-resolved profile measurements are the reason the PS-BGI was created. These are made by continuously recording the ionisation-electron signal from the beam. The beam profile is then reconstructed from the events contained in a time integration window. This window is usually 1 ms wide but this value can be increased or decreased based on the event rate and beam stability. The window is moved in steps smaller or equal to its size.

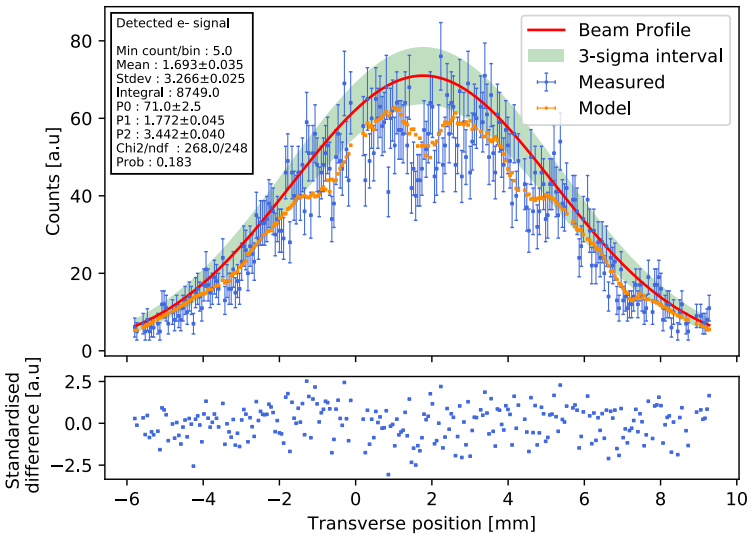

(a) Flat bottom.

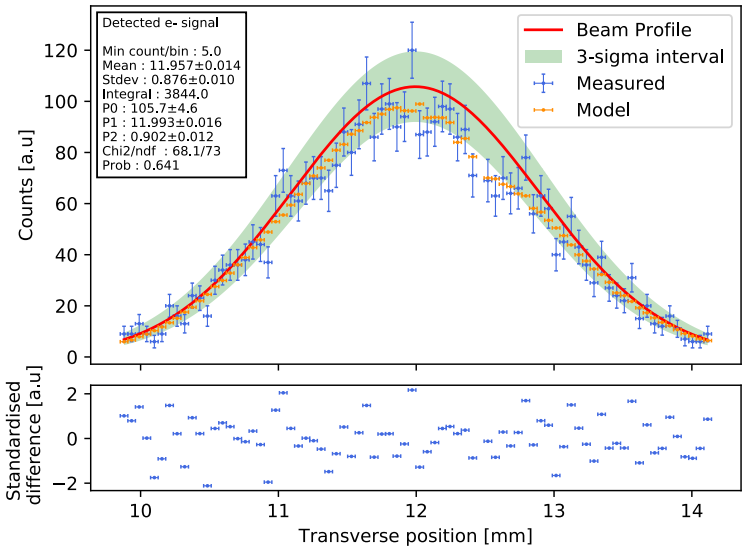

(b) Flat top.

Figure 7.1: Single profiles for the flat bottom and flat top of the BCMS beam. The vertical error bars for the model (orange) are not shown for clarity. The injection and extraction profile have separate x-axis.

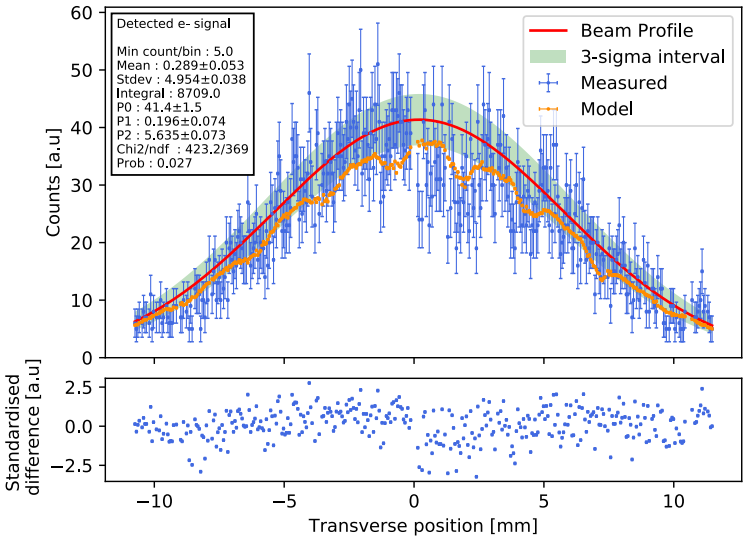

(a) Flat bottom.

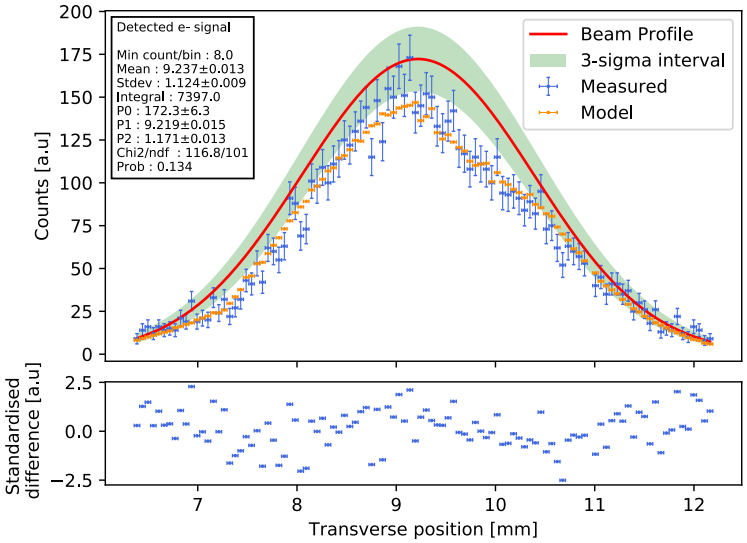

(b) Flat top.

Figure 7.2: Single profiles for the flat bottom and flat top of the nominal LHC beam. The vertical error bars for the model (orange) are not shown for clarity. The injection and extraction profile have separate x-axis.

The beam width and position obtained by this process are then plotted against time.

Figure 7.3 presents time resolved profile measurements for the BCMS and nominal-LHC beams. Both plots were produced with a 1 ms integration window and step size, which corresponds to a sampling frequency of 1 kHz. The figure background-colour represents the result of the profile reconstruction based on the Chi-squared test. A green background implies that the reconstructed profile passed the test, while a white background means that it did not pass the test. In this case, the mean and standard deviation of the ionisation-electron distribution are used in place of μ and σ from the reconstructed profile. This is valid for any other time-resolved profile measurements presented in this thesis.

The time-resolved measurement of the BCMS beam shows that the beam position and width are not static, and are for the most part decoupled. For the first half of the cycle, the beam is large and its width undergoes numerous fluctuations. These are explained by the many RF manipulations — such as the bunch merging and splitting — done to the beam during flat bottom (170 ms to 800 ms). Moreover, the transition is the cause for the blowup observed at 750 ms. During the second half of the cycle, the beam size contracts to reach a minimum before extraction. The contraction corresponds to the adiabatic damping caused by the acceleration of the beam.

Most of the profile reconstructions in the first half of the cycle, as well as in between 1250 ms and 1420 ms, do not pass the Chi squared test. Possible reasons for the former are discussed later in this section. The later is explained by the fact that the beam is largely above chip four (1350 ms to 1380 ms). Chip four does not function and only a small part of the profile tail is recorded by chip three. As a reminder, the space between chip two and three is at 0 mm and chip three extends to 14 mm.

The profile reconstruction is more consistent with the fit model in the second half of the cycle. One can observe that the beam size from the reconstruction is consistently larger than the standard deviation. This is expected since the reconstruction method assumes a significant fraction of the ionisation-electrons are stopped by the steel honeycomb during the transport to the detector.

The LHC beam shows a similar behaviour to the BCMS beam.The profile reconstruction is largely consistent with the fit model on the second half of the cycle; while it remains partly inconsistent with the model in the first half. Nonetheless, all features observed in the BCMS and nominal LHC measurements are consistent with the expected beam dynamics. These time-resolved measurement demonstrate the ability of the instrument to

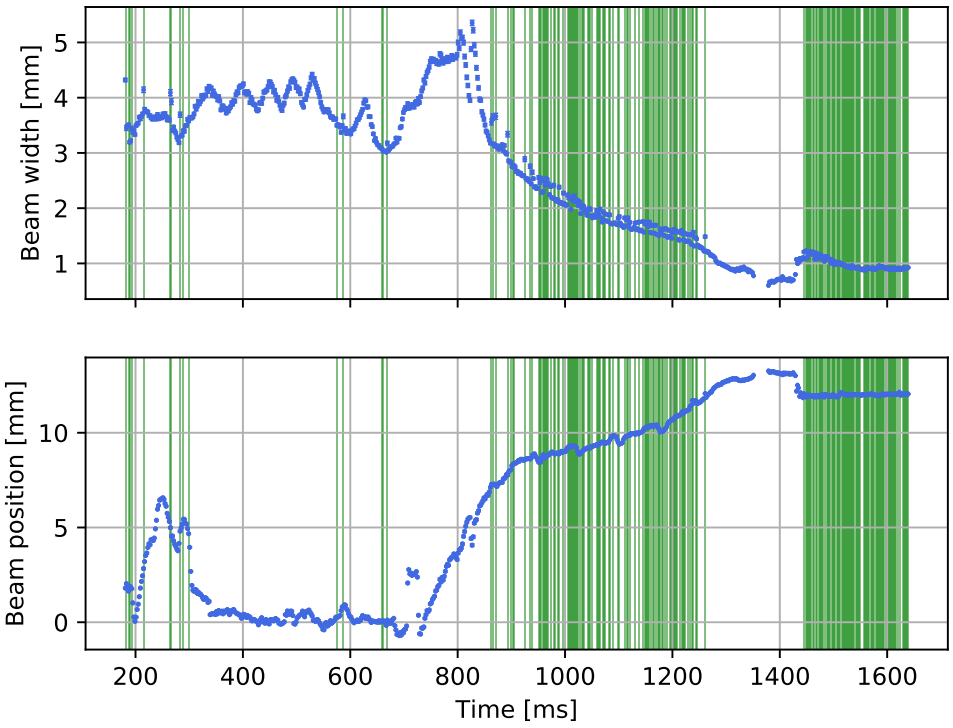

(a) BCMS beam.

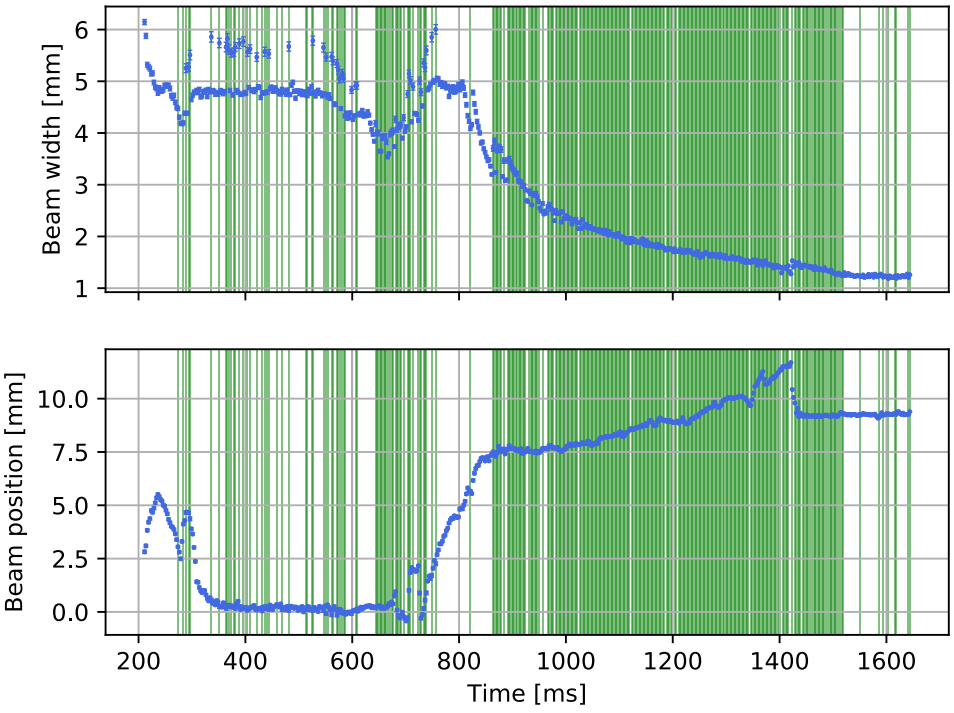

(b) Nominal LHC beam.

Figure 7.3: Time-resolved beam width and position measurements for the BCMS and nominal LHC beams.

measure the beam profile at the required rate of 1 kHz.

The fact that the reconstructed profiles do not appear to pass the Chi squared test when the beam is at flat-bottom can be explained by one of the following reasons:

- The Gaussian model used for the profile reconstruction assumes a non-realistic shape.
- The integration window is not adapted.

7.1.2.1 The beam is non-Gaussian

I have two reasons for implying that the model could be wrong. The first is that the instrument is in its infancy and there is probably unknown sources of systematic error(s). The second is that there are growing internal discussions regarding the fact that the LHC beams might not be Gaussian, or at least during parts of the cycle.

The model used for the profile reconstruction is based on the assumptions that the beam is Gaussian and that all sources of systematic error are accounted for. If one or both of these assumption are wrong, the profile reconstruction will fail.

7.1.2.2 The integration window is not adapted

The integration windows used to make the time-resolved profile measurements is static throughout the cycle. It is manually adjusted to trade-off the time-resolution of the measurement with the ionisation-electron event rate. However, this implies that in some cases the beam —width or position— is changing faster than the integration window. As a consequence, the data-set acquired in the window is the integral of several ionisation-electrons distribution, each with a different beam position or width. It is analogous to taking a picture of a moving object with a too long exposure time.

7.1.3 Instrument precision estimation

The instrument precision was estimated by performing multiple measurements of a beam with a constant width. For this purpose, the PS-BGI measured a particular BCMS beam prepared for a study with the wire-scanner. This beam was injected and no manipulations were performed on it. This allows to assume that the beam width was relatively constant; although a small jitter can not be ruled out due to the beam dynamics. Such jitter also meant that the precision estimate would include both the instrument precision and the

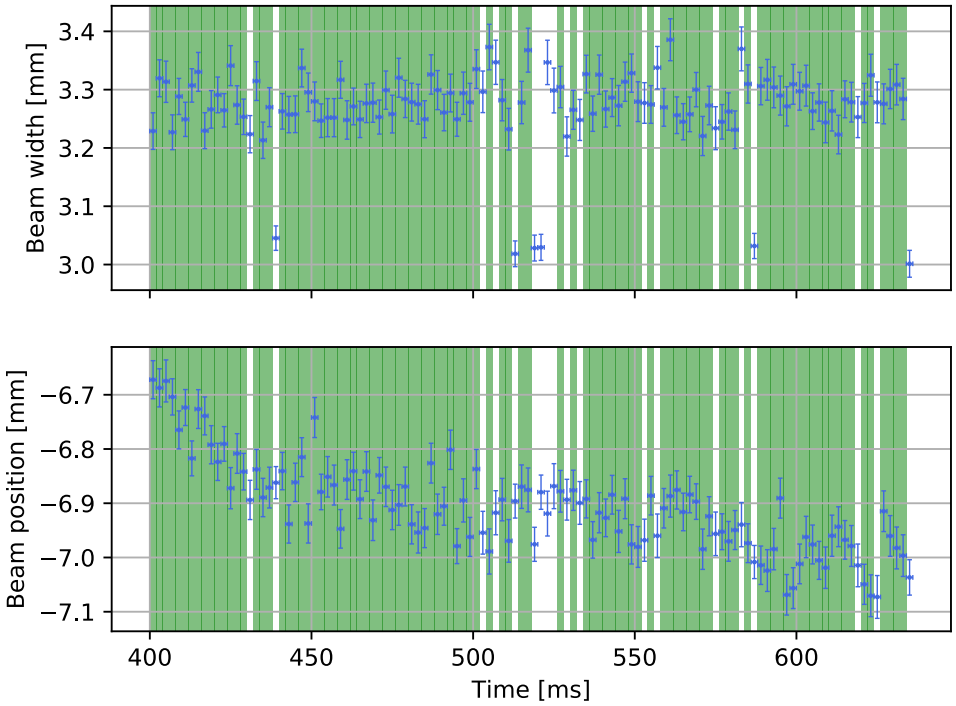

Figure 7.4: Example of a time-resolved beam width and position measurement of one of the cycle used for the precision estimation.

beam width jitter. The estimate presented below is therefore an upper bound for the instrument precision.

The most stable part of the cycle was selected and more than 100 cycles of this beam were recorded. Each cycle yielded 118 profiles with an integration window of 2 ms. As an example, a time-resolved measurement of one cycle is presented in Figure 7.4. One can see that the beam position is drifting by ≈300 µm but the width is relatively constant at ≈3.3 mm.

Due to cycle to cycle variation in the beam width and position, each cycle was treated independently. The precision for each cycle is taken as the standard deviation of the distribution of the beam widths measured for the cycle. Only measurements where the profile reconstruction was successful were used. The average of the precision for all cycles was then used as the final value for the instrument precision.

The measurement resulted in an estimated precision of 49 ± 5 µm or 1.5 ± 0.1 % relative to the mean beam width. The error used here is the standard error. This precision estimate is within the requirements presented in Chapter 2 (2.5 %).

7.2 Effect of the instrument parameters on the measured event-rate and profile measurement

Even if during operation the instrument is operated at its nominal settings, it is necessary to understand the dependencies of the instrument parameters on its performance. For this reason, the effects of the cathode high-voltage, Timepix3 sensor bias-voltage, and the magnetic field strength on the measured event-rate, beam width and position were studied.

The event-rate is directly tied to the resolution of the time-resolved profile measurement. It is therefore crucial to understand how the instrument parameters might affect it. Moreover, the effects on the beam width and position could also be used later to test the Virtual-IPM simulation tool. Unfortunately, due to the low event-rate measured below the nominal values for the scan of the cathode and sensor bias voltages, viably measuring the beam width and position for these cases was impossible. For this reason only the scan of the magnetic field strength presents a measurement of the beam width and position.

The instrument parameters were individually scanned across their full dynamic range, and for each position of the scan 100 ms of the flat top of a BCMS cycle were recorded. To limit biases, all scans were performed on the same day with the same beam and same Timepix3 settings. Each data-set is filtered and the assumption that it contains only ionisation-electron events is made. In order to be comparable, the event-rate is normalised. It is calculated from the total number of event in the data-set divided by the average pressure (mbar), beam intensity (protons), and number of beam revolutions. Moreover the event-rates were calculated from data-sets that showed no signs of readout saturation, which could affect the measurement. For each position in the scans several cycles were recorded. The values displayed in the figures below are the mean from the event-rate several cycles, and the error-bar is the standard error.

7.2.1 Scanning the electric field

The electric field was scanned from 0 kV to −20 kV, while the sensor bias-voltage and magnetic field strength were set to −35 V and 0.2 T respectively. The result of this scan for the event rate is presented in figure 7.5.

One can see that the event rate is almost negligible from 0 kV to −11 kV. It then sharply increase to reach, $0.004\,\mathrm{evnt\,rev^{-1}\,mbar^{-1}\,p^{-1}}$ at −20 kV. The low event-rate at low voltage is explained by three factors. First the minimum energy detectable by

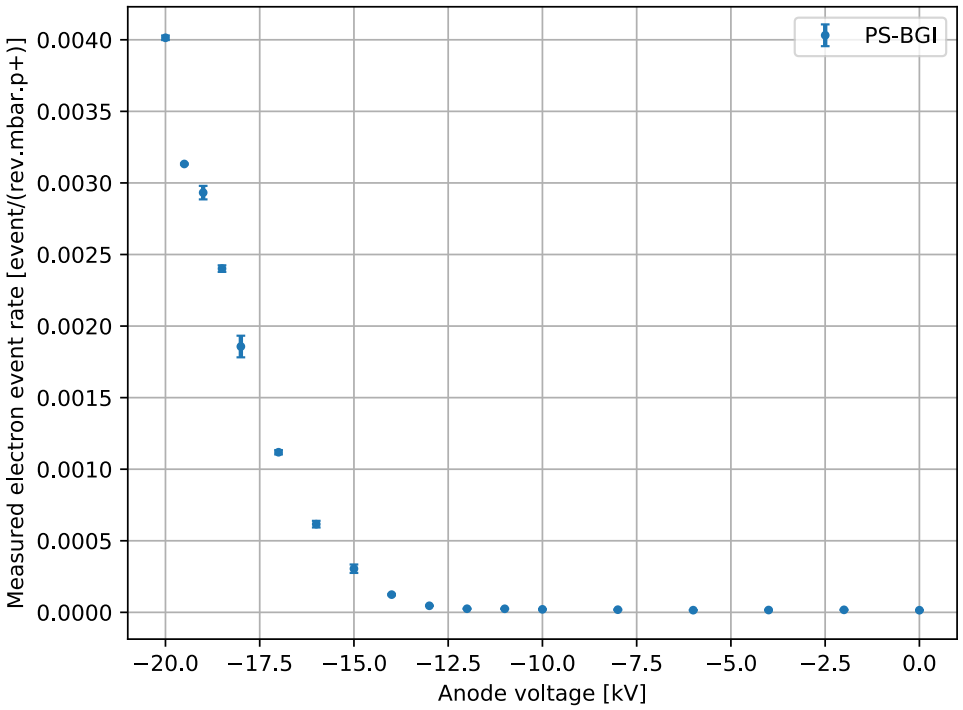

Figure 7.5: Normalised ionisation-electrons event-rate as a function of the cathode high-voltage (Blue).

a Timepix3 is $\approx 2\,\text{keV}$, which corresponds to a cathode voltage of $-4\,\text{kV}$. Second, the Timepix3 thresholds are not set to their absolute minimum, increasing further the aforementioned limit. Third, the thin N+ layer on top of the sensor reduces the charge collection efficiency of the sensor and thus increases the energy required to detect ionising particles.

The large increase seen from $-13\,\text{kV}$ onward is expected as the ionisation-electrons penetration-depth and electron/hole pairs creation increases with the ionisation-electron kinetic energy. However, I also expected the event rate to saturate past a certain point as all ionisation-electrons would have been detected. As one can see, there is no sign of saturation. Moreover, it is interesting to note that the value of the measured event rate at $-20\,\text{kV}$, is twice lower than the one calculated in Section 2.3.3 ($0.008\,\text{evnt}\,\text{rev}^{-1}\,\text{mbar}^{-1}\,\text{p}^{-1}$). The honeycomb masking can explain a small part of the gap in between the two numbers; with an average transmission of 0.87 % (see Chapter 6) and a measured event rate of $0.004\,\text{evnt}\,\text{rev}^{-1}\,\text{mbar}^{-1}\,\text{p}^{-1}$, one would expect the original event rate to be $0.0046\,\text{evnt}\,\text{rev}^{-1}\,\text{mbar}^{-1}\,\text{p}^{-1}$. The rest of the missing ionisation-electrons are either not detected, or are the difference between the model and reality. This suggests that there might be room for improving the event-rate by raising the cathode voltage past $-20\,\text{kV}$.

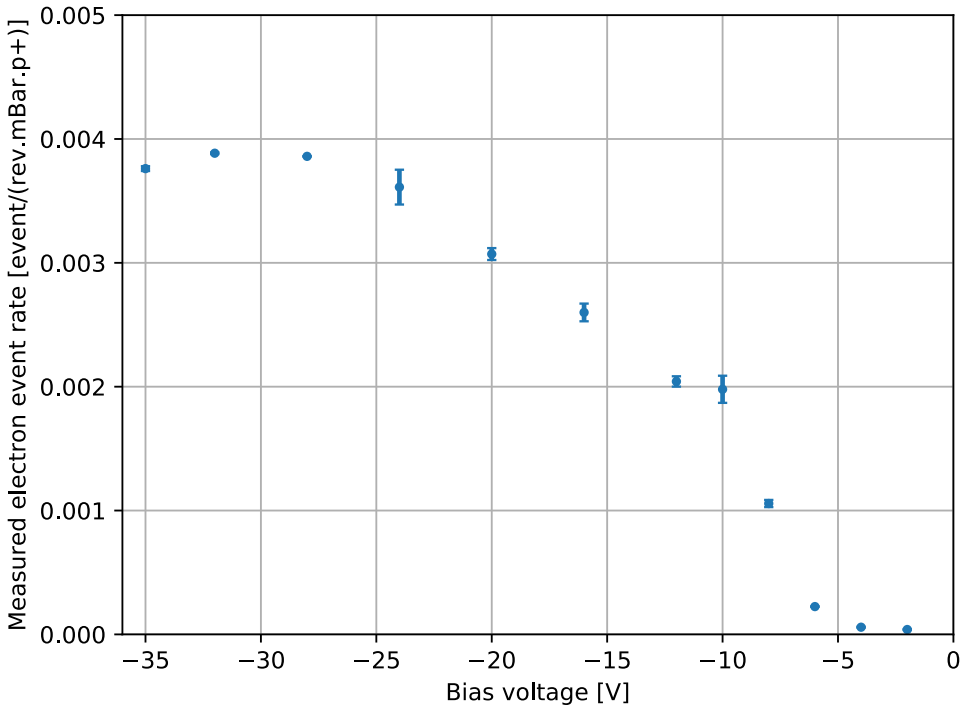

Figure 7.6: Normalised ionisation-electrons event rate as a function of the Timepix3 sensor bias-voltage.

This will be studied in further work.

7.2.2 Scanning the Timepix3 sensor bias-voltage

The Timepix3 sensor bias-voltage was scanned from 0 V to −35 V, while the cathode voltage and magnetic field strength were set to −20 kV and 0.2 T respectively. Figure 7.6 shows the measured event rate as a function of the bias voltage.

No electrons are detected below −5 V, then the event-rate slowly rose to reach a plateau past −25 V. The event-rate value on the plateau reaches a similar value found during the cathode voltage scan. The shape of the event-rate curve is expected as the bias voltage should increase the sensor depletion region — and thus the event rate — up to the point where it is fully depleted. However, one would expect a sharper rise of the event rate as the full depletion voltage for a 100 µm thick silicon sensor is closer to −10 V.

The difference may originate from the unconventional bias voltage distribution scheme used in the PS-BGI detector. Only a small part of the sensor is metallised and thus the voltage might not be well distributed across the sensor surface. A simulation of the detector sensors might answer this question. This is however, not an issue as the detector

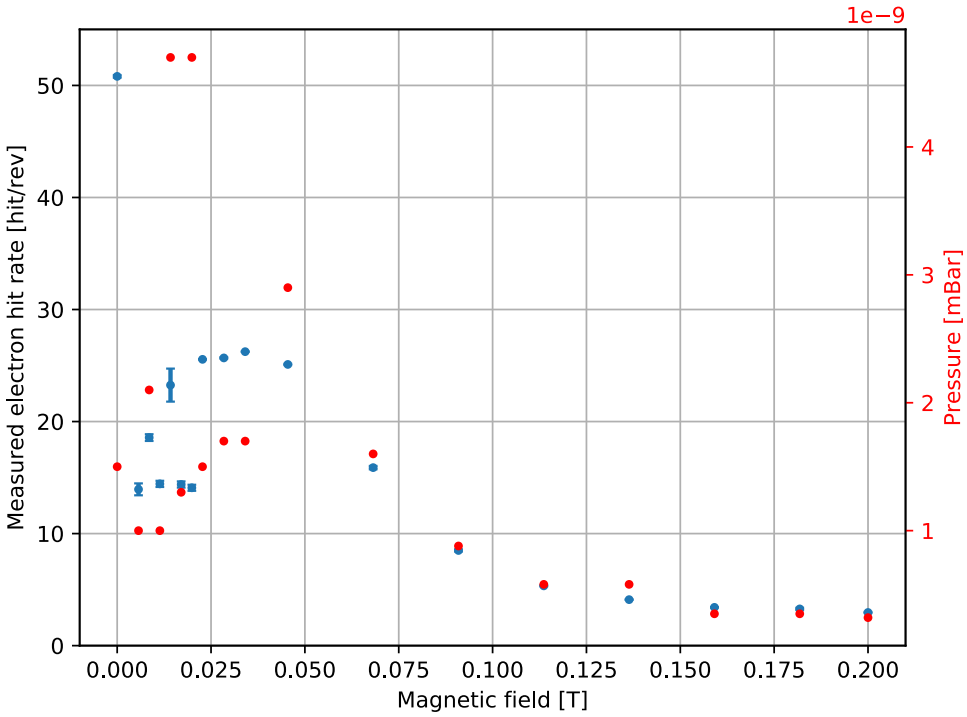

Figure 7.7: Ionisation-electrons event rate as a function of the magnetic field strength. The average pressure in the PS-BGI is given in red.

has always been operated with a sensor bias-voltage superior to −30 V.

7.2.3 Scanning the magnetic filed strength

The magnetic field strength was scanned from 0 T to 0.2 T, while the cathode voltage and Timepix3 sensor bias-voltage were set to −20 kV and −35 V respectively. Figure 7.7 presents the measured event-rate and pressure in the instrument as a function of the magnetic field strength.

From 0.2 T to 0.04 T, the event-rate and pressure increase by a factor eight and ten respectively, they then fluctuate below 0.04 T. These fluctuations are correlated with heavy distortions of the ionisation-electron distribution, causing parts of the detector to saturate. The measurement of the event-rate below 0.04 T is therefore not reliable.

As explained in Section 2.3.3, the instrument gas pressure is directly proportional to the event-rate, which explains the event-rate increase. However, the reason for the pressure increase is, at the moment, unknown.

The effects of the magnetic field strength on the beam width and position are presented in Figure 7.8. The beam width is relatively stable, with a value close to 1.75 mm,

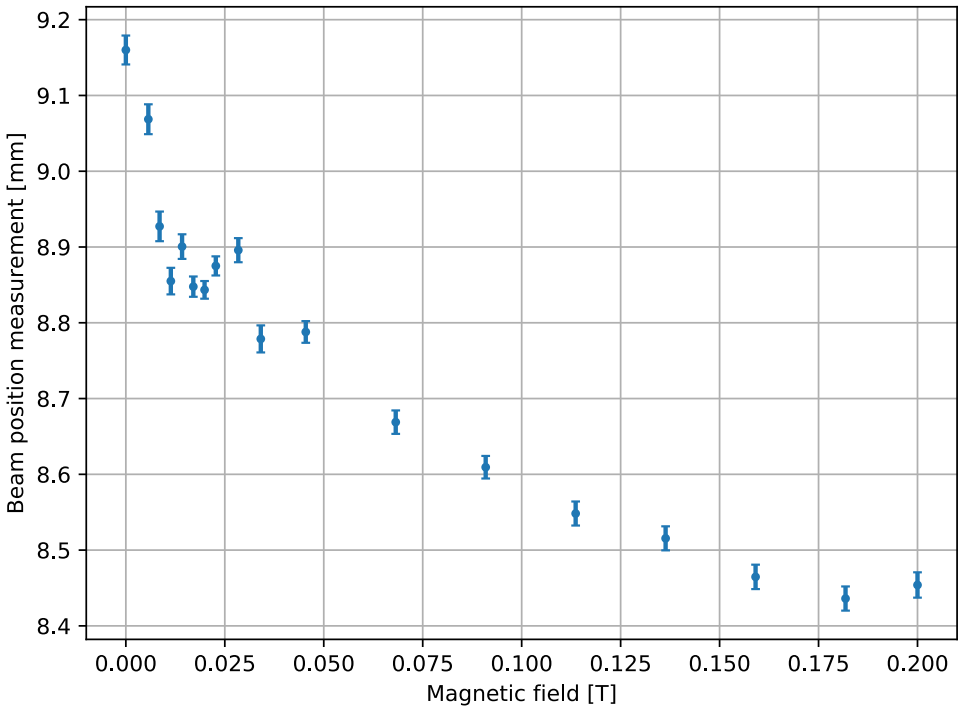

(a) Beam position.

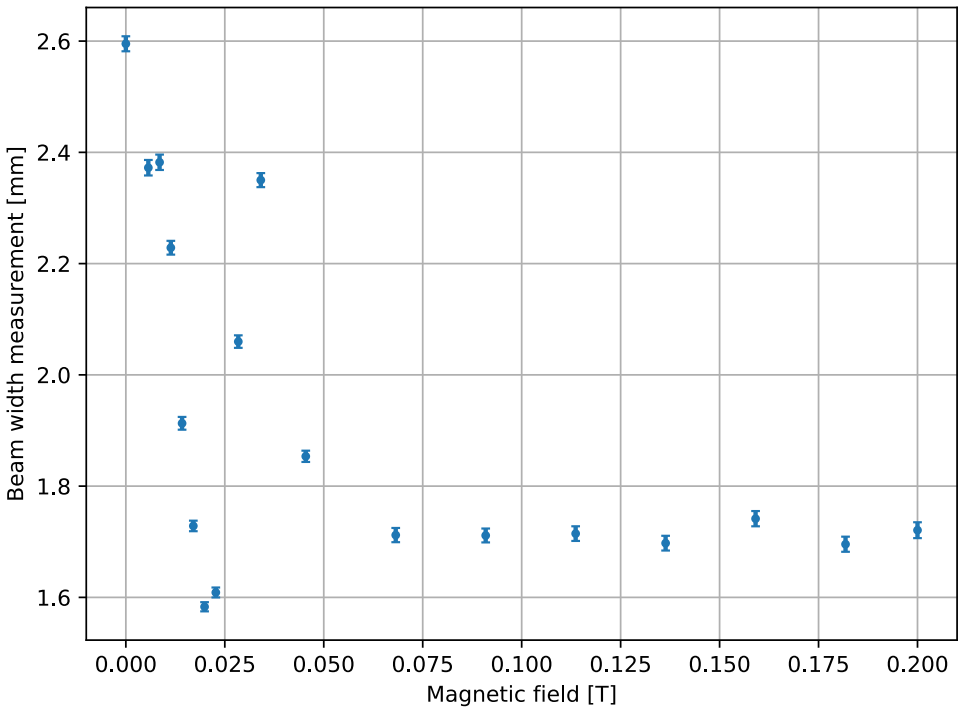

(b) Beam width.

Figure 7.8: Beam position and width as a function of the magnetic field strength. A green background indicates that the values were taken from the result of the profile reconstruction; while a white background indicates that the mean and standard deviation are used instead.

between 0.2 T to 0.07 T. The small variation observed may be caused by cycle to cycle variations. Below 0.7 T, the beam width oscillate to reach 2.6 mm (150 % of 1.75 mm). This result is agreeing with the simulation presented in Section 2.6.6, where the beam size measurement error remains below 1 % between 0.2 T to 0.11 T and then increase to 300 % when the magnetic field reaches zero. The agreement between the simulation and measurement suggests that the PS-BGI magnetic field is larger than required. This opens the possibility to lower the magnetic field to benefit from the increased event-rate at no cost on the measurement quality. As noted previously, below 0.07 T the measured ionisation-electron distribution is heavily distorted and it becomes illogical to try to reconstruct the beam profile. The value given for the beam width and position are therefore the standard deviation and mean of the ionisation-electron distribution.

The beam position is moving by $\approx 700\,\mu$m with a change in magnetic field from 0 T to 0.2 T. This displacement is comparable to the simulations presented in Section 2.6.6, where a displacement of 500 µm was found for the same magnetic field change.

7.3 Instrument time resolution

The current resolution of the time-resolved profile measurement is in the low kiloHertz range. However, the time resolution of the detector is much higher at (1.56 ns), and it is possible to distinguish events from individual beam revolution or even bunches. The potential for such measurements is demonstrated in Figure 7.9, where individual revolutions and bunches from a BCMS beam are visible. The figure shows the number of events as a function of time with a binning of 1 ns and a time window fitting three revolutions.

The injection of eight bunches, the merging of those into four larger bunches and their splitting into 12 smaller once is visible. Each bunch generates between zero and five events per revolution. The fact that the instrument can distinguish between revolution and bunches should allow shortly to measure the profile and width of individual bunches.

The ultimate goal of the PS-BGI is to measure the beam width in a turn by turn and bunch by bunch basis. From the event-rate currently measured in the instrument, such performance is unattainable without a significant change in the beam intensity, vacuum pressure, detection surface or electric field strength. The beam intensity is not a parameter that can be changed just for the PS-BGI while increasing the detection surface is impossible since it would require a complete redesign of the instrument. Moreover, this argument

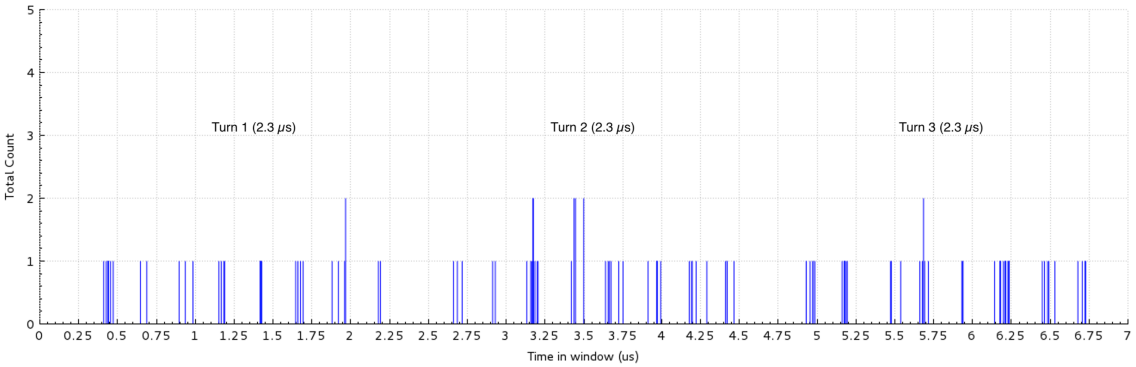

(a) Injection of eight bunches.

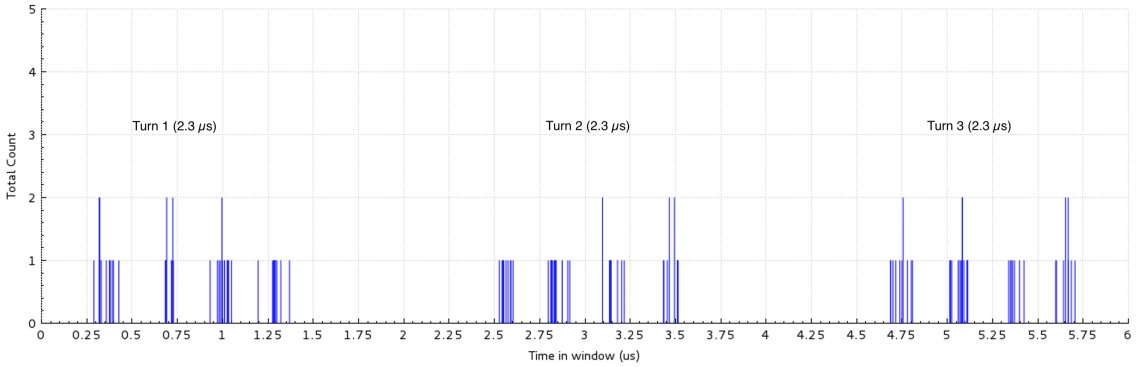

(b) Merging into four larger bunches.

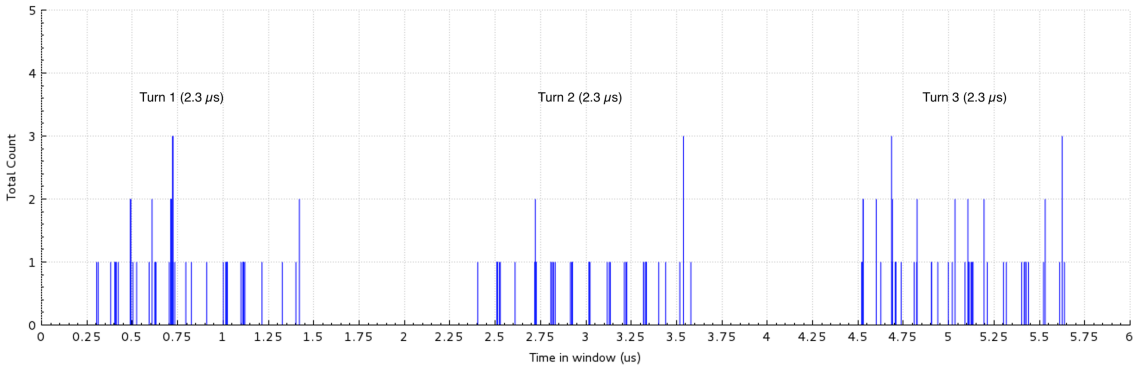

(c) Splitting of four bunches into twelve.

Figure 7.9: Number of event as a function of time for several parts of a BCMS cycle. Each have a time window encompassing three beam revolutions. The first present the beam after the injection of eight bunches from the booster. The second presents the result of the merging of the first eight bunches into four larger ones. The third presents the result of the splitting of those four bunches into twelve.

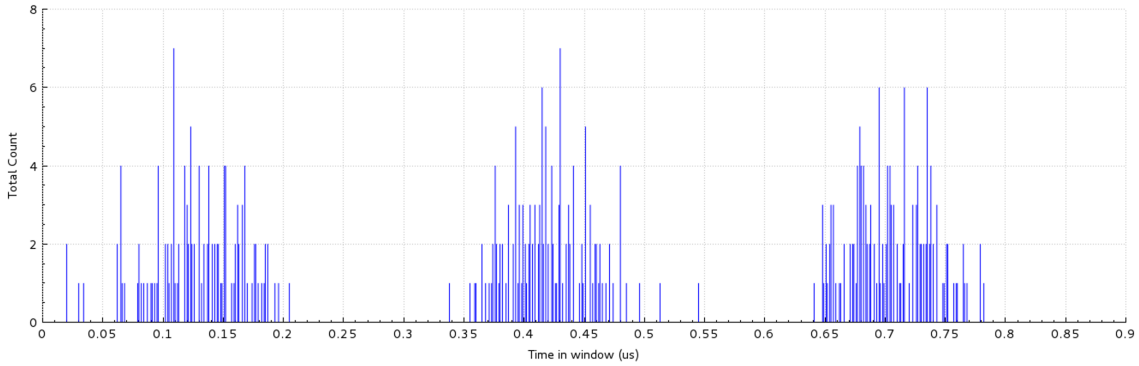

Figure 7.10: Number of events as a function of time for a BCMS beam at injection during the sublimation of a PS ion-pump. Three bunches are visible, each having more than 100 events.

also applies to increasing the electric field strength. Due to the operational requirement of the PS, the vacuum pressure cannot be raised continuously at the instrument location. It may, however, be occasionally raised for a particular study requiring a higher event-rate. In order to asses the potential improvement that such a pressure raise could offer, a few measurements were performed during the daily sublimation of the PS ion-pumps. During this procedure, the pressure increases by up to three orders of magnitude (up to 1×10^{-7} mbar) for a few seconds.

Figure 7.10 presents the events as a function of time for one of these measurement where the pressure rose from 1.5×10^{-10} mbar to 7×10^{-8} mbar. Three bunches are visible, each having more than 100 events. This represents an increase of up to 50 times from what is seen in Figure 7.9. Moreover, it is possible to obtain the bunch length from Figure 7.10. A value of $\approx 150\,\mu$m is found, which is consistent with the expected value of of 160 µm given in Chapter 2.

7.4 Comparison with the beam position monitoring system and wire-scanner

The PS-BGI was compared with the beam position monitoring system and one of the PS wire-scanner. The comparison with the BPM was made as a sanity check; while the comparison with the wire-scanner was performed to check the consistency between the PS-BGI with the wire-scanners.

The instruments simultaneously measured beams with several different widths (wire-scanner) or position (BPM). The result of these measurements is then plotted in the form

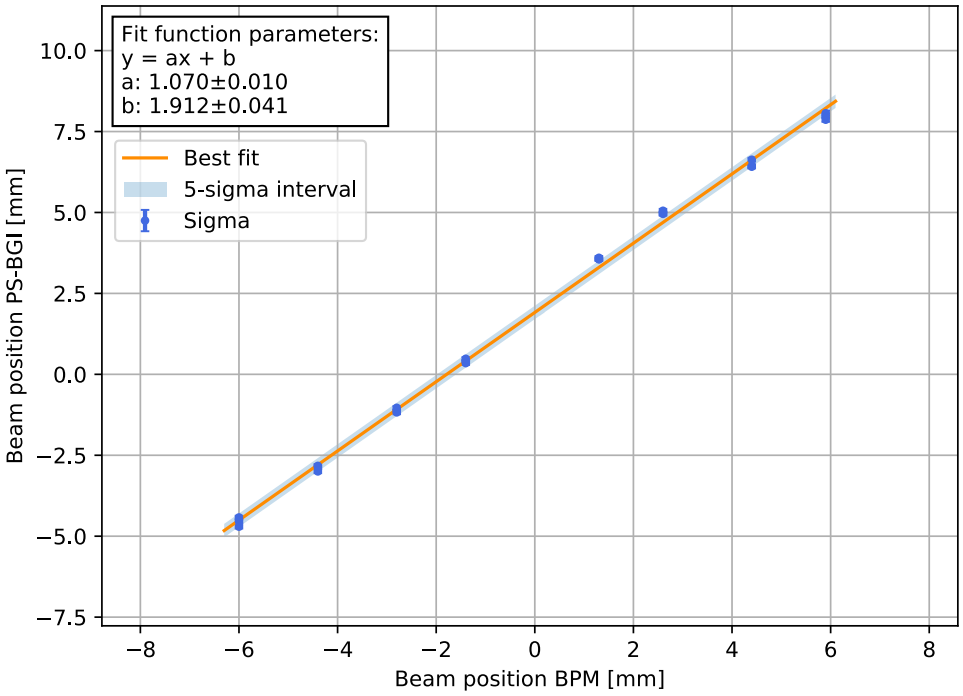

Figure 7.11: Beam position measured by the PS-BGI as a function of the BPM measurement (dark blue). A linear function is fitted to the result (orange) and its five-sigma (five time the error on the fit) interval is displayed (clear blue).

of PS-BGI measurements as a function of BPM or wire-scanner measurements. A simple linear function $f(x) = a.x + b$ is then fitted to the plot. In this context, a represents the proportionality between the two devices; while b represents a permanent offset in the measurement of the PS-BGI compared to the other instrument. A perfect agreement between two instrument should therefore results in $a = 1$ and $b = 0$.

7.4.1 Beam Position Monitor

The BPM is compared to the PS-BGI by having both instruments, simultaneously recording the position of a BCMS beam. This beam is radially displaced by steps of 1.5 mm from −6 mm to 6 mm. The result of this measurement is presented in Figure 7.11, where the relative beam position measured by the BPM is plotted against the PS-BGI measurement.

Figure 7.11 shows a reasonable agreement between the two instruments. The result of the fit of the linear function ($f(x) = a.x + b$) fitted to the result shows a proportionality $a = 1.07 \pm 0.01$ and a 1.91 mm offset. The presence of the offset is expected since the detector was never meant to be perfectly at the centre of the beam pipe; while the deviation of the proportionality from one could result from a small misalignment of the

magnet. As presented in Chapter 2, the instrument transverse electric field is not perfectly homogeneous. A misalignment of the magnet would cause the ionisation-electrons to drift more at certain location than others, affecting the proportionality.

7.4.2 Wire scanner

The PS-BGI was compared to the wire-scanner by measuring BCMS beams with different widths. The wire-scanner used for the measurements is located at PS straight section 65. For this reason the beam width obtained by the wire-scanner had to be converted to the location of the PS-BGI (SS82). We start from the expression of the beam emittance ϵ

$$\epsilon = \frac{\sigma^2 + \left(D \cdot \frac{\Delta p}{p_0}\right)^2}{\beta}, \tag{7.1}$$

where σ is the beam width, D the dispersion, β the value of the betatron function and $\Delta p/p_0$ the beam momentum spread. The emittance is assumed constant and common to both instrument during the measurement, thus

$$\epsilon_{bgi} = \epsilon_{ws}. \tag{7.2}$$

We can then substitute 7.1 in 7.2, using the values for the wire-scanner and PS-BGI, to obtain the expected beam width at the PS-BGI location σ_{bgi} from the measurement at the wire-scanner location σ_{ws}

$$\sigma_{bgi} = \sqrt{\frac{\beta_{bgi}}{\beta_{ws}} \cdot \sigma_{ws}^2 + \left(\frac{\Delta p}{p_0}\right)^2 \cdot \left(\frac{\beta_{bgi}}{\beta_{ws}} \cdot D_{ws}^2 - D_{bgi}^2\right)}. \tag{7.3}$$

Simultaneously to the PS-BGI and wire-scanner measurements, the momentum spread was measured by the PS Tomoscope [111]. The momentum spread was measured to be fluctuating around 4.7×10^{-4} eV. This value is small enough to consider the second part of 7.4 negligible, we thus obtain

$$\sigma_{bgi} = \sqrt{\frac{\beta_{bgi}}{\beta_{ws}} \cdot \sigma_{ws}^2}. \tag{7.4}$$

The value for $\beta_{ws} = 22.32\,\text{m}$ and $\beta_{bgi} = 11.72\,\text{m}$ were taken from the PS lattice simulations [112]. The PS-BGI and wire-scanner measured four different beams, each with a single bunch and intensities ranging from 50×10^{10} protons to 215×10^{10} protons. Due to the

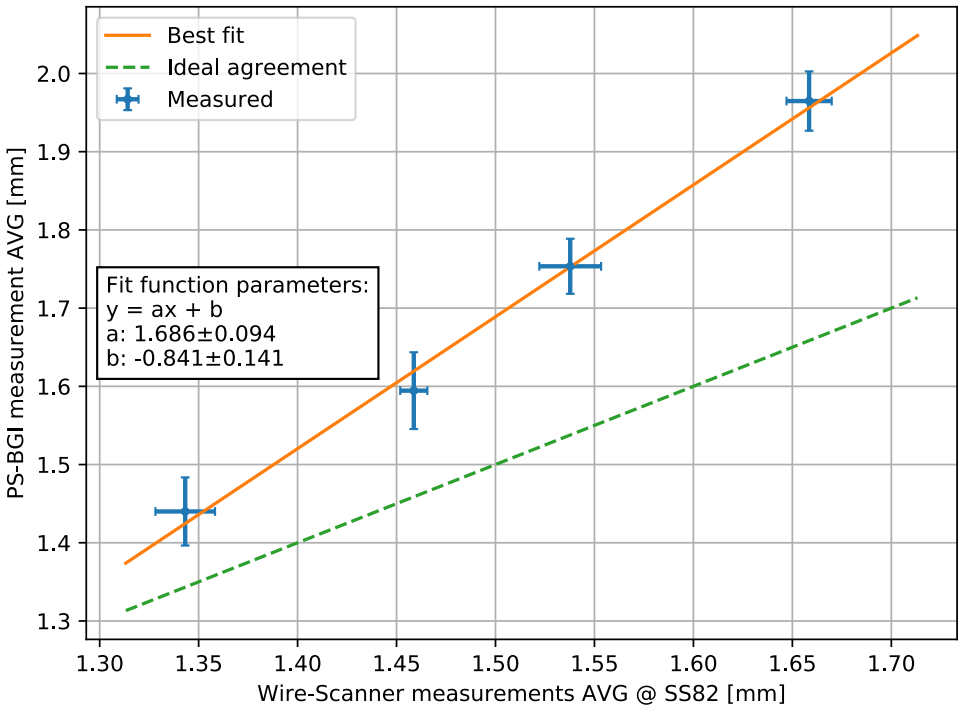

Figure 7.12: Average of the beam width measured by the PS-BGI as a function of the wire-scanner measurement (blue). A linear function is fitted to the result (orange).

way the PS Booster shapes bunches, the bunch intensity is proportional to its emittance and by extension its width. A large intensity will result in a broad beam and vice-versa. The typical measurement procedure for the wire-scanner is to measure five cycles of the same beam and take the average of the measurements as a result. In order to remain coherent with the wire-scanner, this procedure was applied to the PS-BGI. A single profile is thus measured right before the wire-scanner. This timing is used since the wire-scanner can affect the PS-BGI measurement. During a measurement, the wire-scanner interaction with the beam creates beam loss, which is detected by the PS-BGI. Although most of these beam loss can be filtered out, it is best practice to avoid beam loss in the first place. The low event-rate caused by the use of a single bunch makes the smallest viable integration window 3 ms. The error presented with the results is the standard error, which also comprises the cycle to cycle variation in the beam size and the precision of the instruments.

Figure 7.12 presents the results of the measurement. Similarly to the BPM comparison, a linear function is fitted to the results. This fit is consistent with the measurement and shows that the wire-scanner and PS-BGI have a disagreement comprised between 9 %

to 18 %. At the time of writing, there is not obvious reasons to explain this disagreement. The measurements from both instruments were verified several times as well as the beam optics used for the conversion of the wire-scanner measurement to the PS-BGI location. One can point out several shortcomings possibly leading to this result.

- The error on the beta function (β_{ws} and β_{bgi}) was not included in Figure 7.12, nonetheless, it is expected to be around 10 %.
- The Wire-Scanner is intended to provide relative beam size measurements in the PS. However, the accuracy of this instrument is difficult to establish.
- The integration window for the PS-BGI is relatively long and one cannot exclude that the beam might be moving during this period, causing the beam to appear broader than it really is.
- Only four different beam size were used for the measurement. More points would improve the measurement robustness. However, the beam width dynamic range cannot be improved as the intensities used were already at the maximum and minimum achievable.

7.5 Summary

- The PS-BGI demonstrated the ability to measure single profiles and time-resolved profiles at a rate of 1 kHz and with a precision <2 %.
- The time resolution of the detector should allow in the near future measurements of single bunch profiles as well as to accurately distinguish between beam revolutions.
- The nominal values for the cathode and sensor bias voltages provide the highest event-rate.
- A magnetic field strength of 0.2 T is more than sufficient to correct for the beam space charge by a factor of two.
- After a first comparison, the instrument is in reasonable agreement with the PS beam position monitor system but not with the wire-scanner where a disagreement of 9 % to 18 % was observed.

Chapter 8

Outlook and conclusion

8.1 Outlook

8.1.1 Instrument hardware

The instrument presented in this thesis has proven its potential as a fast continuous profile measurement device, however, the limitations presented at the end of Chapter 5 highlight the fact that it is far from from being ready for operational service. The absence of chip four severely reduces the instrument field of view, preventing it from measuring the beam size in the last part of the cycle. Moreover, the under-performing cooling system prevents the instrument from being used for extended periods of time and without constant supervision.

Fortunately, most (if not all) of the issues found with the device hardware can be addressed with a future update of the detector design. In my opinion, the new detector should be made modular, allowing each Timepix3 in the detector to be replaced individually. This would greatly increase the serviceability of the instrument, allowing to replace a single malfunctioning Timepix3 rather than having to replace the whole set.

To improve the detector cooling, the Timepix3 should be directly placed on the cooling plate or on a metal module bolted on it. This would greatly increase the thermal conduction between the chip and the cooling plate, allowing the detector to operate a more stable temperature.

Finally, the power delivery network needs to be improved, larger copper-wire sections and shorter / wider traces on the ceramic PCB would lower the voltage drop at the Timepix3. This would allow the detector to support much higher event-rate (peak current)

and possibly remove the so-called *power glitch*.

8.1.2 Going beyond the requirements

Beyond making the hardware operational, other improvements to the device are foreseen. These are not necessary to achieve the requirements stated in Chapter 2, however, they may greatly increase the device performance, in particular, the instrument measurement frequency.

- Replacing the honeycomb RF shield by a design that ensures the same ionisation-electron transmission factor across the transverse dimension would remove the need to correct for its presence and thus would greatly simplify the beam size measurement method.
- A full integration of the PS timing into the readout system would facilitate to make individual bunch transverse size measurement.
- The discarded background signal generated by the PS-BGI could be used as a fast beam loss monitor. Moreover, the clustering algorithm could be improved to identify the type of particle seen in the background.
- The instrument could be calibrated to offer beam position measurement. At the moment these are only a side product of the beam size measurement and they are therefore not regarded as viable.
- The addition of a gas injection system would allow for single-turn single-bunch beam size measurements. Such very high-speed measurements may be needed in order to study fast emittance growth in the PS.
- As suggested by Chapter 7 measurements, increasing the cathode high-voltage beyond $-20\,\mathrm{kV}$ may increase the ionisation-electron detection rate. This would increase the device measurement frequency, not unlike adding a gas injection system.

8.1.3 Going beyond the PS-BGI

The Timepix3 HPD based detector and radiation tolerant readout-system developed for the PS-BGI are not limited to the PS.

For instance, the LHC BGI's $0.2\,\mathrm{T}$ magnetic field is insufficient to compensate for the distortion induced by the beam space charge [31]. For this reason, the LHC BGIs have been

exclusively used to monitor the ion beam size. A 0.5 T magnetic field would be sufficient to measure the proton beam [113]. However, such a magnet would be too large and expensive to install with the current instrument detection system.

The small form factor of the Timepix3 HPD based detector would allow to reduce the aperture of the LHC BGIs and therefore to provide the required magnetic field with a smaller and cheaper magnet. At present, there is no instrument in use in the LHC capable of measuring the beam size during the LHC energy ramp. A Timepix3 based LHC-BGI would be a solution.

Aside from CERN, other science and medical accelerator facilities, such as KeK [114] and MedAustron [115] have expressed interest in the PS-BGI detection system. Their motivations are the absence of MCP plates, small form factor and beam size measurement frequency possible with this technology.

8.2 Conclusion

The goal of this thesis work was the development, production and commissioning of a new BGI for the CERN PS. The novelty of the PS-BGI is its detection system based on the Timepix3 HPD. This new detection system allows for faster and more reliable profile measurements, while making the device more compact compared to the previous generation of BGIs at CERN. This work was motivated by the demand for a device capable of monitoring the transverse beam size of the LHC-type beams in the PS at a rate of 1 kHz, with an accuracy ≤ 1 % and precision ≤ 2.5 %.

A detailed description of the LHC-type beams and the instrument requirement were presented. The conceptual design of the PS-BGI was given and simulations were run in order to validate it. These simulations showed that a cathode voltage of -20 kV and a magnetic field of 0.2 T were sufficient to mitigate the effects of the beam on the ionisation-electron distribution. The error on the measured beam size is therefore expected to be within the requirements, even for the HL-LHC beams.

The instrument engineering design was presented. This design departs from previous BGIs by the notable absence of side electrodes and an improved ion-trap design. The new detector, based on the Timepix3 HPD, ceramic chip carrier and flexible LCP cables was introduced, along with its radiation tolerant readout system. The main challenge of this new detector was its integration in the primary beam pipe at a pressure lower than

10^{-9} mbar and radiation dose in the region of 10 kGy per year.

The detector in vacuum electronics design was further detailed. Two versions of the detector were produced and tested, one with P-on-N silicon sensor and the other with N-on-P sensors. However, only the N-on-P variant was considered for installation. All parts of the detector were successfully tested for their compatibility with the PS vacuum.

At the start of 2018, the instrument was assembled and successfully installed at the PS straight section 82. Shortly after the installation the PS beam was introduced and the instrument measured the ionisation-electron and background signal. This confirmed that the operation of the Timepix3 HPDs in the PS beam pipe was possible. Furthermore, the detection of the ionisation-electron signal validated the Timepix3 HPD based detector concept. In order to improve the quality of the detector measurements, a method for the Timepix3 equalisation and noise removal was presented and implemented.

In order to make beam profile measurements possible it was necessary to remove the background contribution. A method based on the combination of a clustering filter and energy filter was therefore implemented. The method to extract the beam size from a the ionisation-electron distribution was further introduced. This method fits a model based on the expected beam distribution type (Gaussian) and the imperfection of the detector (steel honeycomb, gap between sensors) to the measured distribution to obtain the beam size.

The first time resolved beam size measurement of the LHC-nominal and BCMS beams was then obtained. The instrument demonstrated the ability to measure beam size and relative position for the complete PS cycle at a rate of 1 kHz. Furthermore, due to the time resolution of the detector, the ability to distinguish between individual bunches of a BCMS beam at different stages of the PS cycle was demonstrated. Measurements of the effect of the instrument magnetic field strength on the measured beam size showed a strong agreement with the early simulation. This provided an important validation of the simulation tool used to design the PS-BGI. A coasting BCMS beam was used to measure the instrument precision. A value of 1.5 % relative to the beam size, well within the required 2.5 %, was found. The PS-BGI was compared to the PS BPM system by the comparing the mean beam position to the BPM reading and to the Wire-Scanner by comparing the mean beam sizes. The instrument measurements were found consistent with the BPM but not with the wire-scanner, where an disagreement between 9 % to 18 % was observed.

In conclusion, this thesis presented the development, from concept to beam size

measurement, of a new BGI for the CERN PS. Despite the limited time frame allocated for it development, the instrument was successfully deployed in the PS and its potential as the next generation of continuous beam profile monitor at CERN was clearly demonstrated.

Bibliography

[1] T. Feder, Accelerator school travels university circuit, Physics Today 63 (2) (2010) 20.

[2] O. S. Brüning, P. Collier, P. Lebrun, S. Myers, R. Ostojic, J. Poole, P. Proudlock, LHC Design Report, CERN Yellow Reports: Monographs, CERN, Geneva, 2004.
URL http://cds.cern.ch/record/782076

[3] The ATLAS Collaboration, Observation of a new particle in the search for the standard model higgs boson with the atlas detector at the lhcarXiv:arXiv:1207.7214, doi:10.1016/j.physletb.2012.08.020.

[4] T. C. Collaboration, Observation of a new boson at a mass of 125 gev with the cms experiment at the lhcarXiv:arXiv:1207.7235, doi:10.1016/j.physletb.2012.08.021.

[5] E. Regenstreif, Le synchrotron protons du CERN, CERN, Geneva, 1958, the volume contains the reports: CERN 58-6a, CERN 59-26 and CERN 61-9.
URL https://cds.cern.ch/record/303392

[6] The 300 GeV programme, CERN, Geneva, 1972, french version available : Le programme 300 GeV.
URL https://cds.cern.ch/record/104068

[7] W. Herr, B. Muratori, Concept of luminosity.
URL http://cds.cern.ch/record/941318

[8] G. Apollinari, I. Bjar Alonso, O. Brning, M. Lamont, L. Rossi, High-Luminosity Large Hadron Collider (HL-LHC): Preliminary Design Report, CERN Yellow Re-

ports: Monographs, CERN, Geneva, 2015.
URL http://cds.cern.ch/record/2116337

[9] L. Rossi, O. Brüning, The High Luminosity Large Hadron Collider: the new machine for illuminating the mysteries of Universe, Advanced series on directions in high energy physics, World Scientific, Hackensack, NJ, 2015, will also be published as a special issue of International journal of modern physics A.
URL http://cds.cern.ch/record/1995532

[10] R. Calaga, Crab Cavities for the LHC Upgrade (2012) 10 p.
URL https://cds.cern.ch/record/1493034

[11] S. Verd-Andrs, J. Skaritka, Q. Wu, B. P. Xiao, S. Belomestnykh, I. Ben-Zv, L. Alberty, K. Artoos, R. Calaga, O. Capatina, T. Capelli, F. Carra, R. Leuxe, N. Kuder, C. Zanoni, Z. Li, A. Ratti, Design and Prototyping of HL-LHC Double Quarter Wave Crab Cavities for SPS Test (CERN-ACC-2015-0183) (2015) 3 p.
URL https://cds.cern.ch/record/2113440

[12] H. Damerau, A. Funken, R. Garoby, S. Gilardoni, B. Goddard, K. Hanke, A. Lombardi, D. Manglunki, M. Meddahi, B. Mikulec, G. Rumolo, E. Shaposhnikova, M. Vretenar, J. Coupard, LHC Injectors Upgrade, Technical Design Report, Vol. I: Protons, Tech. Rep. CERN-ACC-2014-0337 (Dec 2014).
URL http://cds.cern.ch/record/1976692

[13] L. Arnaudon, P. Baudrenghien, M. Baylac, G. Bellodi, Y. Body, J. Borburgh, P. Bourquin, J. Broere, O. Brunner, L. Bruno, C. Carli, F. Caspers, S. M. Cousineau, Y. Cuvet, C. De Almeida Martins, T. Dobers, T. Fowler, R. Garoby, F. Gerigk, B. Goddard, K. Hanke, M. Hori, M. Jones, K. Kahle, W. Kalbreier, T. Kroyer, D. Kchler, A. M. Lombardi, L. A. Lpez-Hernandez, M. Magistris, M. Martini, S. Maury, E. Page, M. Paoluzzi, M. Pasini, U. Raich, C. Rossi, J. P. Royer, E. Sargsyan, J. Serrano, R. Scrivens, M. Silari, M. Timmins, W. Venturini-Delsolaro, M. Vretenar, R. Wegner, W. Weterings, T. Zickler, Linac4 Technical Design Report, Tech. Rep. CERN-AB-2006-084. CARE-Note-2006-022-HIPPI, CERN, Geneva, revised version submitted on 2006-12-14 09:00:40 (Dec 2006).
URL http://cds.cern.ch/record/1004186

[14] G. Arduini, C. Carli, K. Hanke, S. Gilardoni, M. Ludwig, M. Martini, U. Raich, F. Roncarolo, R. Steerenberg, R. Scrivens, Measurement of the transverse beam distribution in the lhc injectors, Tech. rep., CERN (2006).
URL https://edms.cern.ch/document/772786/1

[15] J. Wenninger, Lattice measurements.
URL https://cds.cern.ch/record/1213282

[16] E. J. N. Wilson, An introduction to particle accelerators, Oxford Univ. Press, Oxford, 2001.
URL https://cds.cern.ch/record/513326

[17] S. Hancock, A simple algorithm for longitudinal phase space tomography, Tech. Rep. CERN-PS-RF-NOTE-97-06, CERN, Geneva (May 1997).
URL https://cds.cern.ch/record/1174559

[18] S. Hancock, P. Knaus, M. Lindroos, Tomographic Measurements of Longitudinal Phase Space Density; 1998 ed. (CERN-PS-98-030-RF) (1998) 4 p.
URL https://cds.cern.ch/record/363824

[19] M. Zhang, Emittance formula for slits and pepper pot measurementdoi:10.2172/395453.

[20] R. Veness, N. Chritin, B. Dehning, J. Emery, J. Herranz Alvarez, M. Koujili, S. Samuelsson, J.-L. Sirvent, Design of a high-precision fast wire scanner for the SPS at CERN, Tech. Rep. CERN-ATS-2012-283, CERN, Geneva (Oct 2012).
URL https://cds.cern.ch/record/1495080

[21] J. L. Sirvent Blasco, F. Roncarolo, B. Dehning, A. Dieguez, Beam secondary shower acquisition design for the CERN high accuracy wire scanner, presented 12 Dec 2018 (Sep 2018).
URL https://cds.cern.ch/record/2640438

[22] M. Sapinski, T. Kroyer, Operational limits of wire scanners on LHC beam (2009) 6 p.
URL https://cds.cern.ch/record/1177364

[23] B. Cheymol, Development of beam transverse profile and emittance monitors for the CERN LINAC4, Ph.D. thesis, Clermont-Ferrand U. (2011).

[24] R. Grb, J. Hoyer, The observation screen and TV installation of the external proton beam monitoring system, Tech. Rep. CERN-NPA-Int-69-17, CERN, Geneva (Sep 1969).
URL http://cds.cern.ch/record/2031275

[25] L. Wartski, S. Roland, J. Lasalle, M. Bolore, G. Filippi, Interference phenomenon in optical transition radiation and its application to particle beam diagnostics and multiplescattering measurements, Journal of Applied Physics 46 (8) (1975) 3644–3653. arXiv:https://doi.org/10.1063/1.322092, doi:10.1063/1.322092.
URL https://doi.org/10.1063/1.322092

[26] P. Karataev, S. Araki, R. Hamatsu, H. Hayano, T. Muto, G. Naumenko, A. Potylitsyn, N. Terunuma, J. Urakawa, Beam-size measurement with optical diffraction radiation at KEK accelerator test facility, Phys. Rev. Lett. 93 (2004) 244802. doi:10.1103/PhysRevLett.93.244802.

[27] A. Potylitsyn, Imaging of optical diffraction radiation in pre-wave zone and spatial resolution of non-invasive beam size diagnostics, Nuclear Instruments and Methods in Physics Research Section B: Beam Interactions with Materials and Atoms 266 (17) (2008) 3797 – 3802, radiation from Relativistic Electrons in Periodic Structures. doi:https://doi.org/10.1016/j.nimb.2008.04.020.
URL http://www.sciencedirect.com/science/article/pii/S0168583X08005855

[28] C. Fischer, J. Koopman, D. Kramer, R. Perret, M. Sillanoli, Design and Tests of a New Rest Gas Ionisation Profile Monitor Installed in the SPS as a Prototype for the LHC, AIP Conf. Proc. 732 (CERN-AB-2004-031-BDI) (2004) 133–140. 9 p.
URL https://cds.cern.ch/record/746667

[29] C. Bal, V. Prieto, R. Sautier, G. Tranquille, First Results from the LEIR Ionisation Profile Monitors (CERN-AB-2007-022) (2007) 3 p.
URL http://cds.cern.ch/record/1045238

[30] J. L. Wiza, Microchannel plate detectors, Nuclear Instruments and Methods 162 (1) (1979) 587 – 601. doi:https://doi.org/10.1016/0029-554X(79)90734-1.
URL http://www.sciencedirect.com/science/article/pii/0029554X79907341

[31] M. Sapinski, W. Andreazza, B. Dehning, A. Guerrero, M. Patecki, R. Versteegen, The first experience with LHC beam gas ionization monitor, Tech. Rep. CERN-ATS-2012-286, CERN, Geneva (Oct 2012).
URL http://cds.cern.ch/record/1495085

[32] D. K. Morris, P. Adamson, D. Capista, I. Kourbanis, T. Meyer, K. Seiya, D. Slimmer, M.-J. Yang, J. Zagel, Operational use of ionization profile monitors in the fermilab main injector (2012). arXiv:arXiv:1209.1326.

[33] K. Satou, S. Lee, T. Toyama, H. Harada, N. Hayashi, A. Ueno, Ipm systems for j-parc rcs and mr, Proceedings of HB2010.

[34] G. Kube, Review of synchrotron radiation based diagnostics for transverse profile measurements, Proceding of DIPAC 2007.
URL https://accelconf.web.cern.ch/accelconf/d07/papers/moo1a03.pdf

[35] A. Jeff, A. Boccardi, E. Bravin, A. Fisher, T. Lefevre, A. Rabiller, F. Roncarolo, C. P. Welsch, First results of the LHC longitudinal density monitor, Nucl. Instrum. Methods Phys. Res., A 659 (CERN-ATS-Note-2011-091 TECH) (2011) 549–556. 8 p.
URL https://cds.cern.ch/record/1395374

[36] G. Trad, J.-M. De Conto, F. Roncarolo, Development and Optimisation of the SPS and LHC beam diagnostics based on Synchrotron Radiation monitors, presented 22 Jan 2015 (Oct 2014).
URL https://cds.cern.ch/record/2266055

[37] R. Connolly, C. Degen, L. DeSanto, R. Michnoff, M. Minty, D. Raparia, A laser-wire beam-energy and beam-profile monitor at the bnl linac, Proceedings of 2011 Particle Accelerator Conference.

[38] T. Hofmann, F. Roncarolo, B. Schmauss, S. Gibson, G. Boorman, A. Bosco, Development of a Laser-based Emittance Monitor for Negative Hydrogen Beams. Entwicklung eines Laser-basierten Messgerts zur Ermittlung der Emittanz von Negativen Wasserstoffionenstrahlen, presented 29 Jul 2017 (May 2017).
URL https://cds.cern.ch/record/2282569

[39] T. Tsang, D. Trbojevic, S. Bellavia, R. Connolly, D. Gassner, Y. Makdisi, T. Russo, P. Thieberger, A. Zelenski, A new luminescence beam profile monitor for intense proton and heavy ion beams doi:10.2172/1061920.

[40] P. Forck, A. B. Bank, T. Giacomini, A. Peters, Profile Monitors Based on Residual Gas Interaction (CARE-CONF-05-027-HIPPI. CARE-CONF-2005-027-HIPPI).
URL https://cds.cern.ch/record/924577

[41] T. Ruf, The LHCb VELO and its use in the trigger .
URL http://cds.cern.ch/record/1745497

[42] T. Kirn, Scifi a large scintillating fibre tracker for lhcb, Nuclear Instruments and Methods in Physics Research Section A: Accelerators, Spectrometers, Detectors and Associated Equipment 845 (2017) 481 – 485, proceedings of the Vienna Conference on Instrumentation 2016. doi:https://doi.org/10.1016/j.nima.2016.06.057.
URL http://www.sciencedirect.com/science/article/pii/S016890021630599X

[43] M. Rihl, J. Marton, M. Ferro-Luzzi, Development of a non-destructive beam-profile monitor based on scintillating fibre planes and SIPMs, presented 25 Apr 2018 (Mar 2018).
URL https://cds.cern.ch/record/2318275

[44] A. Alexopoulos, C. Barchel, A. Bay, F. Blanc, E. Bravin, G. Bregliozzi, N. Chritin, B. Dehning, M. Ferro-Luzzi, S. Gian, M. Giovannozzi, O. Girard, R. Greim, G. Haefeli, P. Hopchev, R. Jacobsson, L. Jensen, O. Rhodri Jones, V. Kain, W. Karpinski, T. Kirn, A. Kuonen, R. Matev, T. Nakada, M. Rihl, V. Salustino Guimaraes, S. Schael, O. Schneider, A. Schultz von Dratzig, G. Schwering, M. Tobin, R. Veness, Q. Veyrat, S. Vlachos, M. Wlochal, B. Wiirkner, Z. Xu, First LHC transverse beam size measurements with the beam gas vertex detector, J. Phys. : Conf. Ser. 874 (CERN-ACC-2017-315. 1) (2017) 012086. 6 p.
URL https://cds.cern.ch/record/2276055

[45] P. Hopchev, V. Baglin, C. Barschel, E. Bravin, G. Bregliozzi, N. Chritin, B. Dehning, M. Ferro-Luzzi, C. Gaspar, M. Giovannozzi, E. van Herwijnen, R. Jacobsson, L. Jensen, O. Rhodri Jones, N. Jurado, V. Kain, M. Kuhn, B. Luthi, P. Magagnin, R. Matev, N. Neufeld, J. Panman, M. Rihl, V. Salustino Guimaraes, B. Salvant,

R. Veness, A. Bay, F. Blanc, S. Gian, G. Haefeli, T. Nakada, B. Rakotomiaramanana, O. Schneider, M. Tobin, Q. Veyrat, Z. Xu, R. Greim, W. Karpinski, T. Kirn, S. Schael, A. Schultz von Dratzig, G. Schwering, M. Wlochal, A Beam Gas Vertex detector for beam size measurement in the LHC (CERN-ACC-2014-0134) (2014) 5 p.
URL https://cds.cern.ch/record/1742250

[46] G. Maps, last accessed : Jan 18. [link].
URL https://goo.gl/maps/jkqUV

[47] T. Poikela, J. Plosila, T. Westerlund, M. Campbell, M. D. Gaspari, X. Llopart, V. Gromov, R. Kluit, M. van Beuzekom, F. Zappon, V. Zivkovic, C. Brezina, K. Desch, Y. Fu, A. Kruth, Timepix3: a 65k channel hybrid pixel readout chip with simultaneous ToA/ToT and sparse readout, Journal of Instrumentation 9 (05) (2014) C05013–C05013. doi:10.1088/1748-0221/9/05/c05013.
URL https://doi.org/10.1088%2F1748-0221%2F9%2F05%2Fc05013

[48] Private correspondence with the members of the Medipix3 collaboration (2017).

[49] S.Levasseur, Development and integration of a new beam gas ionization monitor for cern proton synchrotron, Master's thesis (2015).

[50] O. Keller, B. Dehning, M. Sapinski, L. Swann, Feasibility Study of a Novel, Fast Read-out System for an Ionization Profile Monitor Based on a Hybrid Pixel Detector (2015) MOPAB41. 5 p.
URL http://cds.cern.ch/record/2158996

[51] D. Vilsmeier, M. Sapinski, T. Wettig, Profile distortion by beam space-charge in Ionization Profile Monitors, presented 24 Apr 2015 (Apr 2015).
URL https://cds.cern.ch/record/2012342

[52] F. F. Rieke, W. Prepejchal, Ionization cross sections of gaseous atoms and molecules for high-energy electrons and positrons, Phys. Rev. A 6 (1972) 1507–1519. doi:10.1103/PhysRevA.6.1507.
URL https://link.aps.org/doi/10.1103/PhysRevA.6.1507

[53] A. B. Voitkiv, N. Grn, W. Scheid, Hydrogen and helium ionization by relativistic projectiles in collisions with small momentum transfer, Journal of Physics B: Atomic,

Molecular and Optical Physics 32 (15) (1999) 3923.
URL http://stacks.iop.org/0953-4075/32/i=15/a=321

[54] K. Schindl, Space charge.
URL https://cds.cern.ch/record/941316

[55] M. Bassetti, G. A. Erskine, Closed expression for the electrical field of a two-dimensional Gaussian charge, Tech. Rep. CERN-ISR-TH-80-06. ISR-TH-80-06, CERN, Geneva (1980).
URL http://cds.cern.ch/record/122227

[56] D. Vilsmeier, B. Dehning, M. Sapinski, Investigation of the Effect of Beam Space-charge on Electron Trajectories in Ionization Profile Monitors (2015) MOPAB42. 5 p.
URL https://cds.cern.ch/record/2158997

[57] M. Patecki, M. Sapinski, A. Kisiel, Analysis of LHC Beam Gas Ionization monitor data and simulation of the Electron transport in the detector, presented 18 Sep 2013 (Aug 2013).
URL https://cds.cern.ch/record/1610547

[58] M. Patecki, B. Dehning, G. Iadarola, M. Sapinski, Electron Tracking Simulations in the Presence of the Beam and External Fields (CERN-ATS-2013-050) (2013) 3 p.
URL https://cds.cern.ch/record/1566614

[59] D. Vilsmeier, M. Sapinski, R. Singh, J. W. Storey, Reconstructing space-charge distorted IPM profiles with machine learning algorithms, Journal of Physics: Conference Series 1067 (2018) 072003. doi:10.1088/1742-6596/1067/7/072003.
URL https://doi.org/10.1088%2F1742-6596%2F1067%2F7%2F072003

[60] R. Singh, M. Sapinski, D. Vilsmeier, Simulation supported profile reconstruction with machine learningdoi:10.18429/JACoW-IBIC2017-WEPCC06.
URL http://accelconf.web.cern.ch/AccelConf/ibic2017/papers/wepcc06.pdf

[61] Computer simulation technology (cst) studio, 3d electromagnetic simulation software, https://www.cst.com, accessed: 2019-02-06.

[62] K. Satou, J. W. Storey, S. Levasseur, G. Schneider, D. Bodart, M. Sapinski, A novel field cage design for the CPS IPM and systematic errors in beam size and emittance, Journal of Physics: Conference Series 1067 (2018) 072008. doi:10.1088/1742-6596/1067/7/072008.
URL https://doi.org/10.1088%2F1742-6596%2F1067%2F7%2F072008

[63] D. Vilsmeier, A modular framework for simulations of ionization profile monitors - implementation and benchmarking, please find the git repository here: https://gitlab.com/IPMsim/Virtual-IPM (September 2017).
URL https://epub.uni-regensburg.de/36198/

[64] M. Van Rooij, J. P. Bertuzzi, M. Brouet, A. Burlet, C. Burnside, R. Gavaggio, L. Petty, A. Poncet, The Vacuum Upgrade of the CERN PS and PS Booster.
URL https://cds.cern.ch/record/907557

[65] P.PACHOLEK, Thermal analyses and cooling solution design for the silicon pixel detector in ps-ipm, Project Report 1500338, CERN (march 2015).
URL https://edms5.cern.ch/document/1500338/0.1

[66] T. M. collaboration, last accessed : Fev 19. [link].
URL https://medipix.web.cern.ch/collaboration/medipix3-collaboration

[67] X. Llopart, R. Ballabriga, M. Campbell, L. Tlustos, W. Wong, Timepix, a 65k programmable pixel readout chip for arrival time, energy and/or photon counting measurements, Nuclear Instruments and Methods in Physics Research Section A: Accelerators, Spectrometers, Detectors and Associated Equipment 581 (1) (2007) 485 – 494, vCI 2007. doi:https://doi.org/10.1016/j.nima.2007.08.079.
URL http://www.sciencedirect.com/science/article/pii/S0168900207017020

[68] J. Jakubek, Precise energy calibration of pixel detector working in time-over-threshold mode, Nuclear Instruments and Methods in Physics Research 633 (2011) 262–266.

[69] The nist stoping power and range table for electrons (estar) database., last accessed : Fev 19.
URL https://physics.nist.gov/PhysRefData/Star/Text/ESTAR.html

[70] D. Pitzl, N. Cartiglia, B. Hubbard, D. Hutchinson, J. Leslie, K. O'Shaughnessy, W. Rowe, H.-W. Sadrozinski, A. Seiden, E. Spencer, H. Ziock, P. Ferguson, K. Holzscheiter, W. Sommer, Type inversion in silicon detectors, Nuclear Instruments and Methods in Physics Research Section A: Accelerators, Spectrometers, Detectors and Associated Equipment 311 (1) (1992) 98 – 104. doi:https://doi.org/10.1016/0168-9002(92)90854-W.
URL http://www.sciencedirect.com/science/article/pii/0168900292908 54W

[71] G. Casse, P. P. Allport, M. Hanlon, Improving the radiation hardness properties of silicon detectors using oxygenated n-type and p-type silicon, IEEE Transactions on Nuclear Science 47 (3) (2000) 527–532. doi:10.1109/23.856475.

[72] J. Visser, M. van Beuzekom, H. Boterenbrood, B. van der Heijden, J. Muñoz, S. Kulis, B. Munneke, F. Schreuder, SPIDR: a read-out system for medipix3 & timepix3, Journal of Instrumentation 10 (12) (2015) C12028–C12028. doi:10.1088/1748-0221/10/12/c12028.
URL https://doi.org/10.1088%2F1748-0221%2F10%2F12%2Fc12028

[73] H. Sandberg, W. Bertsche, D. Bodart, B. Dehning, S. Gibson, S. Levasseur, K. Satou, G. Schneider, J. Storey, R. Veness, First use of timepix3 hybrid pixel detectors in ultra-high vacuum for beam profile measurements, Journal of Instrumentation 14 (1). doi:10.1088/1748-0221/14/01/C01013.

[74] M. B. Marin, A. Boccardi, C. D. Godichal, J. Gonzalez, T. Lefevre, T. Levens, B. Szuk, The giga bit transceiver based expandable front-end (GEFE)—a new radiation tolerant acquisition system for beam instrumentation, Journal of Instrumentation 11 (02) (2016) C02062–C02062. doi:10.1088/1748-0221/11/02/c02062.
URL https://doi.org/10.1088%2F1748-0221%2F11%2F02%2Fc02062

[75] P. Moreira, The radiation hard gbtx link interface chip, PH-ESE Electronics Seminars (nov 2013).
URL http://indico.cern.ch/event/267408/material/slides/1.pdf

[76] The versatile link project, https://www.cst.com, accessed: 2019-02-06.

[77] Microsemi proasic3 fpga, https://www.microsemi.com/product-directory/fpgas/1690-proasic3, accessed: 2019-02-26.

[78] Arduino, https://www.arduino.cc, accessed: 2019-02-26.

[79] Xilinx virtex-7 FPGA VC707 evaluation kit, https://www.xilinx.com/products/boards-and-kits/ek-v7-vc707-g.html, accessed: 2019-02-26.

[80] C. G. Larrea, K. Harder, D. Newbold, D. Sankey, A. Rose, A. Thea, T. Williams, IPbus: a flexible ethernet-based control system for xTCA hardware, Journal of Instrumentation 10 (02) (2015) C02019–C02019. doi:10.1088/1748-0221/10/02/c02019.
URL https://doi.org/10.1088%2F1748-0221%2F10%2F02%2Fc02019

[81] The CMS experiment, https://cms.cern, accessed: 2019-02-26.

[82] Google protocol buffers, https://developers.google.com/protocol-buffers, accessed: 2019-02-26.

[83] Alpha advanced material, https://www.alphaadvancedmaterials.com/Products/Non-Conductive-Polymers/STAYSTIK-672, accessed: 2019-03-02.

[84] Epoxy technology, https://www.epotek.com/site/component/products/productdetail.html?cid=120&Itemid=, accessed: 2019-03-02.

[85] Ansys high frequency structure simulator, https://www.ansys.com/fr-fr/products/electronics/ansys-hfss, accessed: 2019-03-02.

[86] Molex slimstack connectors, https://www.molex.com/molex/products/family?key=slimstack_fine_pitch_smt_board_to_board_connectors&channel=PRODUCTS&chanName=family&pageTitle=Introduction&utm_source=ds&utm_medium=lit&utm_campaign=general&WT.mc_id=A03447, accessed: 2019-03-02.

[87] Nasa outgassing data for selecting spacecraft materials, https://outgassing.nasa.gov, accessed: 2019-03-02.

[88] Cern dcdc project, https://project-dcdc.web.cern.ch/project-dcdc/, accessed: 2019-03-02.

[89] Advacam, last accessed : Fev 19. [link].
URL http://advacam.com

[90] Hightec, http://hightec.ch/home/, accessed: 2019-03-02.

[91] Fineline qpi, http://www.qpigroup.com/en/home, accessed: 2019-03-02.

[92] Panasonic flexible circuit board materials, https://industrial.panasonic.com/ww/products/electronic-materials/circuit-board-materials/felios/felioslcp, accessed: 2019-03-02.

[93] A.MICHET, Vacuum acceptance test report: Pixel detector for the ps gas injection beam profile monitor (bgi), Project Report 1698132, CERN (march 2017).
URL https://edms5.cern.ch/document/1698132

[94] A.MICHET, Vacuum acceptance test report: Of 5 components for the ps gas injection beam profile monitor (bgi), Project report, CERN, not officialy published (march 2016).

[95] Private correspondence with Jerome Alozy (member of the Medipix3 collaboration) (2016).

[96] N.Thaus, Vacuum acceptance test report of the complete gas injection beam profile monitor $\mathrm{ps}_b giha0014(bgi-h-ps-cr000002)$, Project Report 1895201, CERN (april 2018).
URL https://edms.cern.ch/document/1895201/1

[97] D. Faircloth, Technological Aspects: High Voltage (arXiv:1404.0952) (2014) 381–419. 39 p, comments: 39 pages, contribution to the CAS-CERN Accelerator School: Ion Sources, Senec, Slovakia, 29 May - 8 June 2012, edited by R. Bailey, CERN-2013-007. doi:10.5170/CERN-2013-007.381.
URL https://cds.cern.ch/record/1693330

[98] J. Rinkel, D. Magalhes, F. Wagner, E. Frojdh, R. B. Sune, Equalization method for medipix3rx, Nuclear Instruments and Methods in Physics Research Section A: Accelerators, Spectrometers, Detectors and Associated Equipment 801 (2015) 1 – 6. doi:https://doi.org/10.1016/j.nima.2015.08.029.
URL http://www.sciencedirect.com/science/article/pii/S0168900215009638

[99] J. Bouchami, A. Gutirrez, T. Holy, A. Houdayer, J. Jakbek, C. Lebel, C. Leroy, J. Macana, J.-P. Martin, S. Pospil, S. Prak, P. Sabella, C. Teyssier, Measurement of pattern recognition efficiency of tracks generated by ionizing radiation in a

medipix2 device, Nuclear Instruments and Methods in Physics Research Section A: Accelerators, Spectrometers, Detectors and Associated Equipment 633 (2011) S187 – S189, 11th International Workshop on Radiation Imaging Detectors (IWORID). doi:https://doi.org/10.1016/j.nima.2010.06.163.
URL http://www.sciencedirect.com/science/article/pii/S0168900210013537

[100] T. Holy, E. Heijne, J. Jakubek, S. Pospisil, J. Uher, Z. Vykydal, Pattern recognition of tracks induced by individual quanta of ionizing radiation in medipix2 silicon detector, Nuclear Instruments and Methods in Physics Research Section A: Accelerators, Spectrometers, Detectors and Associated Equipment 591 (1) (2008) 287 – 290, radiation Imaging Detectors 2007. doi:https://doi.org/10.1016/j.nima.2008.03.074.
URL http://www.sciencedirect.com/science/article/pii/S0168900208004592

[101] L. Landau, On the energy loss of fast particles by ionization, J. Phys.(USSR) 8 (1944) 201–205.

[102] J. Storey, W. Bertsche, D. Bodart, B. Dehning, S. Gibson, S. Levasseur, H. Sandberg, M. Sapinski, K. Satou, G. Schneider, R. Veness, First Results From the Operation of a Rest Gas Ionisation Profile Monitor Based on a Hybrid Pixel Detector (2018) WE2AB5. 5 p.
URL https://cds.cern.ch/record/2663359

[103] C. A. R. Hoare, Algorithm 64: Quicksort, Commun. ACM 4 (7) (1961) 321–. doi:10.1145/366622.366644.
URL http://doi.acm.org/10.1145/366622.366644

[104] ATLAS collaboration, A neural network clustering algorithm for the ATLAS silicon pixel detector. A neural network clustering algorithm for the ATLAS silicon pixel detector, JINST 9 (CERN-PH-EP-2014-120. CERN-PH-EP-2014-120) (2014) P09009. 38 p, comments: 6 pages plus author list + cover pages (38 pages total), 10 figures, 0 tables, submitted to JINST, All figures including auxiliary figures are available at http://atlas.web.cern.ch/Atlas/GROUPS/PHYSICS/PAPERS/PERF-

2012-05. doi:10.1088/1748-0221/9/09/P09009.
URL https://cds.cern.ch/record/1712337

[105] S. Agostinelli, J. Allison, K. Amako, J. Apostolakis, H. Araujo, P. Arce, M. Asai, D. Axen, S. Banerjee, G. Barrand, F. Behner, L. Bellagamba, J. Boudreau, L. Broglia, A. Brunengo, H. Burkhardt, S. Chauvie, J. Chuma, R. Chytracek, G. Cooperman, G. Cosmo, P. Degtyarenko, A. Dell'Acqua, G. Depaola, D. Dietrich, R. Enami, A. Feliciello, C. Ferguson, H. Fesefeldt, G. Folger, F. Foppiano, A. Forti, S. Garelli, S. Giani, R. Giannitrapani, D. Gibin, J. G. Cadenas, I. Gonzlez, G. G. Abril, G. Greeniaus, W. Greiner, V. Grichine, A. Grossheim, S. Guatelli, P. Gumplinger, R. Hamatsu, K. Hashimoto, H. Hasui, A. Heikkinen, A. Howard, V. Ivanchenko, A. Johnson, F. Jones, J. Kallenbach, N. Kanaya, M. Kawabata, Y. Kawabata, M. Kawaguti, S. Kelner, P. Kent, A. Kimura, T. Kodama, R. Kokoulin, M. Kossov, H. Kurashige, E. Lamanna, T. Lampn, V. Lara, V. Lefebure, F. Lei, M. Liendl, W. Lockman, F. Longo, S. Magni, M. Maire, E. Medernach, K. Minamimoto, P. M. de Freitas, Y. Morita, K. Murakami, M. Nagamatu, R. Nartallo, P. Nieminen, T. Nishimura, K. Ohtsubo, M. Okamura, S. O'Neale, Y. Oohata, K. Paech, J. Perl, A. Pfeiffer, M. Pia, F. Ranjard, A. Rybin, S. Sadilov, E. D. Salvo, G. Santin, T. Sasaki, N. Savvas, Y. Sawada, S. Scherer, S. Sei, V. Sirotenko, D. Smith, N. Starkov, H. Stoecker, J. Sulkimo, M. Takahata, S. Tanaka, E. Tcherniaev, E. S. Tehrani, M. Tropeano, P. Truscott, H. Uno, L. Urban, P. Urban, M. Verderi, A. Walkden, W. Wander, H. Weber, J. Wellisch, T. Wenaus, D. Williams, D. Wright, T. Yamada, H. Yoshida, D. Zschiesche, Geant4a simulation toolkit, Nuclear Instruments and Methods in Physics Research Section A: Accelerators, Spectrometers, Detectors and Associated Equipment 506 (3) (2003) 250 – 303. doi:https://doi.org/10.1016/S0168-9002(03)01368-8.
URL http://www.sciencedirect.com/science/article/pii/S0168900203013688

[106] S. Spannagel, K. Wolters, D. Hynds, N. A. Tehrani, M. Benoit, D. Dannheim, N. Gauvin, A. Nrnberg, P. Schtze, M. Vicente, Allpix2: A modular simulation framework for silicon detectors, Nuclear Instruments and Methods in Physics Research Section A: Accelerators, Spectrometers, Detectors and Associated Equipment 901 (2018) 164 – 172. doi:https://doi.org/10.1016/j.nima.2018.06.020.

URL http://www.sciencedirect.com/science/article/pii/S0168900218307411

[107] The scipy python library, https://www.scipy.org, accessed: 2019-04-02.

[108] R. L. Plackett, Karl pearson and the chi-squared test, International Statistical Review / Revue Internationale de Statistique 51 (1) (1983) 59–72.
URL http://www.jstor.org/stable/1402731

[109] R. D'Agostino, M. A. Stephens, Goodness-of-fit techniques, Statistics, Dekker, New York, NY, 1986.
URL https://cds.cern.ch/record/1348022

[110] G. Kasprowicz, J. Belleman, U. Raich, Digital Beam Trajectory and Orbit System, for the CERN Proton Synchrotron (CERN-AB-2007-021) (2007) 3 p.
URL https://cds.cern.ch/record/1045237

[111] S. Hancock, S. R. Koscielniak, M. Lindroos, Longitudinal Phase Space Tomography with Space Charge; rev. version, Phys. Rev. Spec. Top. Accel. Beams 3 (CERN-PS-2000-068-OP. 12) (2000) 124202. 8 p. doi:10.1103/PhysRevSTAB.3.124202.
URL https://cds.cern.ch/record/468153

[112] Mad - methodical accelerator design, https://madx.web.cern.ch/madx/, accessed: 2019-04-17.

[113] D. Vilsmeier, M. Sapinski, R. Singh, Space-charge distortion of transverse profiles measured by electron-based ionization profile monitors and correction methods, Physical Review Special Topics - Accelerators and Beams 22. doi:10.1103/PhysRevAccelBeams.22.052801.

[114] KEK, High Energy Accelerator Research Organisation, last accessed : July 19. [link].
URL https://www.kek.jp/en/

[115] MedAustron, the center for ion therapy, last accessed : July 19. [link].
URL https://www.medaustron.at/